De-Multiplexed Multiwavelength Interferometry for High Precision Metrology

By

Syed Zain-Ul-Abideen Zaidi

A dissertation submitted in partial satisfaction of the

requirements for the degree of

Doctor of Philosophy

in

Engineering - Electrical Engineering and Computer Sciences

in the

Graduate Division

of the

University of California, Berkeley

Committee in charge:

Professor Constance J. Chang-Hasnain, Chair
Professor Ming-Chiang Wu
Professor Feng Wang

Fall 2019

De-Multiplexed Multiwavelength Interferometry for High Precision Metrology

Abstract

De-Multiplexed Multiwavelength Interferometry for High Precision Metrology

by

Syed Zain-Ul-Abideen Zaidi

Doctor of Philosophy in Engineering - Electrical Engineering and Computer Sciences

University of California, Berkeley

Professor Constance J. Chang-Hasnain, Chair

In the era of global warming, harnessing green energy has become a top priority for nations around the world. Solar cells have been developed for over half a century, but the dull appearances of solar cells impede their widespread adaptation in size-constrained metropolitan cities like Singapore. Current colorful solar cell technologies are extremely inefficient, and their adaptation cannot be justified. In the first part of this thesis, we propose a new way to use High Contrast Gratings to materialize colorful solar cells with a very small penalty on efficiencies. We show optimized designs for Silicon, Indium-Phosphide, and Perovskite solar cells, and verify the viability of our idea through preliminary experimental demonstrations.

In the second part of the thesis, we innovate in nanoscale metrology, a key component of nanomanufacturing. Many areas of science and technology rely on the precise determination of distance over a sufficiently long range. Advanced ranging technology has the potential to open up a wide application field including 3D sensing, robotics and inspection for automated manufacturing, where high-precision, long-range, efficiency, and noise-tolerance are key. The small wavelength of light makes it a suitable candidate for precision metrology. A single wavelength interferometer has a high accuracy, but a small range that is limited by the ambiguous interferometric fringe order. We present a new arithmetic algorithm for multiwavelength interferometry that has a theoretical maximum range of the lowest-common-multiple of the wavelengths used, the resolution of a single-wavelength interferometer, and the theoretical maximum noise tolerance of an algebraic approach. We first describe the analytical formulation, analyze the noise tolerance, and present a recursive solution to extend the range through multiple wavelengths. To justify the practicality, experimental results from a simultaneous phase shifting demultiplexed two-wavelength interferometry system, with a range-resolution ratio of > 3e5, are presented to demonstrate the reliability of our method in the absence of any error correction.

To my loving parents, Shaista and Salman.

Acknowledgements

I am so very grateful for all things that conspired to take me where I am today. Foremost, I am grateful to God for everything, and grateful for being able to be grateful. I am indebted to my loving parents for being my most important teachers, and for their prayers and unconditional support during all phases of my life. I would like to thank them for being supportive of my endeavors, even if it meant not being able to see me for extended periods of time.

I would like to thank my advisor, Professor Connie Chang-Hasnain, for allowing me to explore my curiosity, passion and interests. Her unending enthusiasm is contagious and motivated me to push through obstacles. It is through her that I have been able to connect with many renowned experts in Tucson, Singapore and China. I will continue to reflect upon her very many wise anecdotes and analogies.

My research projects would not have been possible without the help of my internal and external collaborators. I am grateful to Dr. Jonas Kapraun, an alumnus of the CCHG group, and Dr. Firdaus Bin Suhaimi, from the Nanyang Technological University, for help with Perovskite solar cell fabrication. I thank the Singapore-Berkeley Research Initiative for Sustainable Energy (SinBeRISE) program for enabling and funding the colorful solar cell project. I am truly indebted to Dr. Vala Fathipour for teaching me fiber and free-space optical setups, and for her constant companionship through the challenges of the De-multiplexed multiwavelength interferometry project. I thank Xiangli Jia for her brilliant insights, especially on analytical formulation. I will forever cherish the fond memories of working together with Vala and Xiangli. We acknowledge the tremendous help of Professor James Wyant and Michael North-Morris in mentoring our work. This work would not have been possible without the support of Tsinghua-Berkeley Shenzhen Institute (TBSI).

The tight-knit optoelectronics community is one of the reasons I attended UC Berkeley. I greatly benefited from my discussions with members of the Ming and Eli groups. In particular, I am thankful to Jodi Loo, Jean-Etienne Tremblay, Sri Krishna, Dr. Andy Michaels, Zunaid Omair, and Sean Hooten for their help, friendship and support. I am indebted to the CCHG group, and in particular Dr. Adair Gerke and Dr. Linda Li for the mentorship and help. I will forever cherish my fond memories with Xiangli Jia, Jipeng Qi, Mingyue Guan and Yipeng Ji.

Teaching EE16B has been one of my best experiences at Cal. I am very thankful for having had the chance to work with an incredibly talented teaching team. I am inspired by their kindness and genuine care about teaching and will fondly look back on the memories I formed with the staff, especially, Maggie, Karina, Titan, Ramsey, Mikaela, Jove, Justin, and Victor.

Furthermore, this could not have been possible without the love and support of my wife, Shizza Fatima. Thank you for always being there for me, and for cheering me on through the ups and downs of life. Finally, I am thankful for my son, Hassan Mujtaba, for brightening up even my darkest days.

Table of Contents

List of Figures

Chapter 1: Introduction

1.1 Utilizing and Enabling Nanotechnology

As researchers and engineers in nanotechnology, we are driven, not only by the desire to push the limits of science by utilizing the latest nanomanufacturing techniques, but also by the need to make these enabling nanomanufacturing techniques precise, reliable and fast. This dissertation offers a flavor of both classes of innovation.

We begin by tackling an often-overlooked dimension of solar cells: their dull appearance. We discuss how nanotechnology can be used to make solar cells colorful, without significantly compromising their efficiencies. But as James Wyant, former dean of the College of Optical Sciences at University of Arizona Tucson, famously reminds, we cannot manufacture something finer than our ability to measure it. We thus transition to innovate in nanoscale metrology, a key component of nanomanufacturing, and improve the range, accuracy and speed of metrology systems.

1.2 Aesthetic and Efficient Solar Cells

In the era of global warming, harnessing green energy has become a top priority for nations around the world. However, for metropolitan cities, the adaption of solar energy harvesters is impeded by the dull, and rather ugly, appearance of solar cells. This is particularly an issue for small energy and aesthetic-conscious nations like Singapore.

Current colorful solar cells are very inefficient. The most common category of colorful solar cells is Dye Synthesized Solar Cells (DSSC), pioneered by Professor Michael Grätzel at Ecole polytechnique fédérale de Lausanne (EPFL), and thus also called Grätzel cells. The cells use dyes, sensitized with mesoporous TiO2 films and Rethenium (Ru) based compounds [1], [2]. Researches have demonstrated vibrant solar cells with colors from red to green, but with efficiency around 2% [3]. The efficiencies are better for DSSC with a non-tunable particular color, such as the near 10% efficiency reported for a blue DSSC [4]. However, the best efficiency for DSSC, about 12%, are for cells constructed with black dyes [5]. Yet, this is in stark contrast to the best efficiencies obtained from single-crystalline Silicon and thin-film GaAs solar cells, with the best reported efficiencies of 26.7% [6] and 29.1% [7], respectively.

Other techniques employed to make solar cells colorful significantly deteriorate their efficiencies. Perovskite solar cells are hybrid organic-inorganic lead-based cells, and have gained popularity because of their high efficiency, low-cost and ease of manufacturability. The record efficiencies for stable Perovskite cells reach about 24.2% [8], but appear black. Doctor-blade coated Perovskite cells produce mixed mosaic-like arbitrary colors, but lose about 20% efficiency [9]. Researchers have developed Perovskite cells with tunable colors, but with efficiencies of only 12.3% [10].

Hence, there is a need for a new technique to make colorful solar cells, one that makes up for the efficiency lost because of the light reflected to make it colorful. In our work we propose to achieve this with the use of High Contrast Gratings and propose designs that are supported by Rigorous coupled-wave analysis (RCWA) and Finite-difference time-domain (FDTD) simulations. We also investigate the practicality of implementing our designs on fabricated Perovskite solar cells.

1.3 Precision Metrology

In the times of shrinking dimensions, there is a growing demand for technologies that enable the precise measurement of critical features at a fast speed. During nanomanufacturing, this is typically done with either stylus-based profilometers or scanning electron microscopes (SEM). Stylus-based profilometers are quick but invasive as they drag a sharp needle across the surface. SEM scans are non-invasive and extremely accurate but take a long while to set up.

Alternatively, the non-invasive nature and small wavelength of electromagnetic waves, at the visible and infrared (IR) spectrums, make it a promising candidate for precision metrology. Light based 3D sensing technologies can be divided into two categories: incoherent, and coherent. The most popular among the non-coherent techniques is time of flight and relies on the time it takes for a pulse of light to reflect from a target. Since the clocking speed of the system determines the smallest time that can be detected, the accuracy is in a few millimeters for systems with clocking speeds in the few GHz. Another incoherent technique, commonly used for facial detection in cell phones, uses structured light together with triangulation. A pseudo-random projected pattern is distorted by the target, and the distortions can be used to calculate depths [11]. However, since a correspondence between the distorted and original pattern has to be found, large clusters of projected dots form windows that are analyzed together, and this significantly limits the lateral resolution to a few millimeters [12], [13].

The best accuracies are obtained from coherent systems obtained through the interference of light. Swept laser source based Frequency Modulated Continuous Wave (FMCW) systems are being explored for ranging and autonomous vehicles, but the accuracy is a function of the sweep length of the laser, and due to practical limitations, does not get finer than a few micrometers [14]. The finest accuracies are obtained from a single wavelength interferometer systems, and it is the underlying technology behind the gravitational wave detection at LIGO [15]. The accuracy depends on the uncertainty in phase measurements and can be sub-nanometers. However, the practical applications of these systems are limited because of its small one-wavelength long unambiguous range. Dual-comb interferometry can offer a high precision of <10 nm at a long range but requires ultrafine stabilization through piezoelectric transducers, f -2f interferometers and temperature controllers, and is thus a very expensive solution [16], [17].

An alternative cost-effective solution for practical high-precision metrology systems is to extend the range of the highly precise single wavelength interferometer. In this part of the work, we demonstrate our cost effective and computationally inexpensive system that utilizes multiple wavelengths to achieve fine resolution and long range.

1.4 Thesis Outline

This thesis consists of two parts that can be read independently. The work on colorful and efficient solar cells is all contained in Chapter 2. We start with an overview of HCG theory in Section 2.1. These properties are then utilized to design efficient Silicon and InP solar cells in Section 2.2. For the color dimension of the solar cells, we discuss a way to simulate perceived color in Section 2.3. The framework developed in all the previous sections is then used in Section 2.4 to design efficient and colorful HCG-enabled Perovskite solar cells.

The second part of the thesis is about demultiplexed multiwavelength interferometry. We begin by laying the foundations in Chapter 3 with a thorough discussion of a single-wavelength interferometer, the building block of our system. We discuss the importance of interferometric phase, how to extract it from the interferograms, and the impact of phase-noise on it. In Chapter 4, after a brief discussion on prior work, we discuss our demultiplexed multiwavelength mathematical formulation that is noise-tolerant, precise and achieves a long range. Our formulation is validated with experimental results in Chapter 5, where we demonstrate both ranging and the 3D imaging of samples.

Chapter 2: Colorful Efficient Solar Cells

It is inherently contradictory to make solar cells both efficient and colorful at the same time and is what makes this problem interesting and challenging. Color is due to light reflected from a surface, and thus colorful solar cells have to reflect light. From the perspective of efficiency, reflected light is not absorbed, and thus leads to a lower efficiency because it does not contribute to the generation of electron-hole pairs.

We propose a solution to this dilemma through the use of High Contrast Gratings (HCGs), fabricated on the top surface of the solar cell. For this purpose, we utilize two properties of the optimized HCG designs: 1) high reflectivity of light at selected wavelengths, and 2) efficient waveguide light coupling. Fig. 2.1 shows an illustration of how colorful and efficient solar cells can be materialized with the use of HCGs. The parameters of the solar cell and the HCG are optimized such that they reflect an intended color. The efficiency lost due to reflection, is made up by enhanced coupling of light at other wavelengths into the thin film solar cell region. Furthermore, our structures are designed to facilitate color tuning across the entire visible spectrum, using variations that are achievable through lithography.

In this chapter, we first discuss some of the unique properties of HCGs that enable their use in colorful, efficient solar cells. We then validate HCG theories with Rigorous coupled-wave analysis (RCWA) and Finite-difference time-domain (FDTD) simulations, discuss optimization strategies, and show optimized designs for Silicon, Indium Phosphide (InP) and Perovskite Solar cells. Lastly, we discuss the integration of HCGs with Perovskite solar cells and show photoluminescence (PL) and I-V spectrum that support our hypothesis.

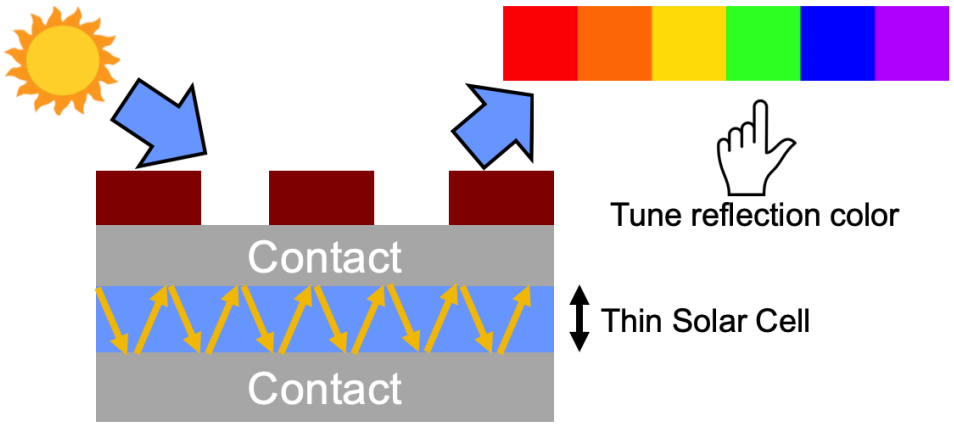

Figure 2.1 An illustration of how colorful and efficient solar cells are materialized through integration with High Contrast Gratings (HCGs). The parameters of the HCG are optimized such that they reflect a specific color, that can be tuned. Simultaneously, they also enhance the coupling of light at other wavelengths.

2.1 Unique Properties of High Contrast Gratings

High contrast gratings are a special form of periodic gratings, with a particular thickness, period and duty cycle. These gratings exhibit special properties when their refractive index is very different from their surroundings, and hence have a high contrast to their surroundings. The detailed physics behind the exotic properties have been thoroughly discussed before [18], [19], but some of the important deductions are repeated here for completion.

The interesting HCG properties can be primarily understood by studying the dominant eigenmodes in the subwavelength regime. When the grating period is much smaller than the wavelength of light, the gratings can be modelled as thin film with an effective-index, and the reflection is like that from a thin film. On the contrary, if the grating period is much larger than the wavelength, the interaction is dominated by diffraction, and gives rise to many interfering modes. The most interesting behavior, however, occurs when the period of the gratings is close to the wavelength, and the light-grating interaction is dominated by very few, usually just two, eigenmodes. The interaction between these modes can either be characterized as anti-crossing, where resonance of the modes is in-phase, or crossing, where they are out of phase. The anti-crossing interaction is also observed in other systems like photonic crystals [20] and quantum-dot cavities [21], [22], and is indicative of strong resonance of optical field in the HCG. This phenomenon has been utilized to make HCG based high-Q resonators [23] and have found applications in HCG-enabled biosensing [24].

Very high reflectivity or transmittivity can also be achieved with the HCG. This occurs in the crossing regime, when the resonance of dominant eigenmodes are out of phase and destructively interfere. High reflection occurs when the modes destructively interfere at the exiting plane, after passing through the thickness of the HCG. But modes destructively interfering at the first air/HCG interface result in high transmission. These properties have enabled the use of HCG as a high reflectivity mirror, a replacement for the bulky distributed Bragg reflector (DBR) mirrors, in Vertical Cavity Surface Emitting Lasers (VCSELs) [25]–[27]. These effects can occur at any near-period wavelength by tuning the geometric parameters of the HCG: the period, duty cycle, and thickness.

Another useful property of the HCGs is their ability to efficiently couple light into waveguides. This property is an extension of the high-Q resonance modality. Efficient coupling can occur when a thin layer, with a definitive eigen-mode, is placed within the decay length of the evanescent field of a resonant HCG. HCG parameters, for which the coupling would occur, can be found by searching for the anti-crossing between the resonant HCG eigenmodes and the vertical eigenmodes of the thin waveguide, in RCWA simulations. This principle has been used to design HCG couplers for Silicon nanophotonic waveguides, with coupling efficiencies of up to 98% [28]. We extensively use this feature of the HCG to enhance efficiencies by coupling light into thin film solar cells. In the next section, we show some examples of this coupling property, and verify them with RCWA and FDTD simulations.

2.2 High Contrast Gratings for Efficient Coupling

In this section, we explore the abilities of HCG to efficiently couple light in the context of solar cell structures. We first start with thin film Silicon solar cell structures and highlight key characteristics of the coupling mechanism. We then discuss how absorption plots are a quicker way to analyze the enhanced coupling and show how they can be combined with the solar spectrum to get the short-circuit current density. Throughout this section, we continuously countercheck our designs with both RCWA and FDTD simulations.

We first elaborate on the anti-crossing mechanism, discussed in the previous section. To do so, we use a 300 nm thick Silicon slab, and use it as a model for a thin-film Silicon solar cell. Every solar cell also needs electrical contacts, and for this model, we choose 150 nm thick Indium Cadmium Oxide (ICO). ICO's excellent electrical conductivity and optical transparency make it an excellent candidate for top-side solar cell contacts [29]. The Amorphous Silicon (A-Si) High Contrast Gratings were then designed on top of the ICO, as illustrated in Fig. 2.2. The design parameters included the thickness, duty cycle and the period of the HCGs, and were optimized for enhanced coupling using our in-house RCWA code [30]. The refractive index for ICO was fixed at 2.2, but the refractive index for Silicon and A-Si were taken from Palik [31]. All materials were fixed to be lossless by setting their imaginary refractive index to 0. Full wave FDTD simulations are very time-consuming, so we use RCWA simulations to find the best designs that support efficient coupling. The characteristic thickness-wavelength, or t_g-λ, reflection plot for an optimized set of parameters is shown in Fig. 2.3 (a). Each point of the plot represents the reflectivity of a TM-polarized plane wave incident at 0°, for a particular wavelength, and thickness of the HCG. The entire plot was calculated for an optimized grating period of 549 nm and 62.4% duty cycle.

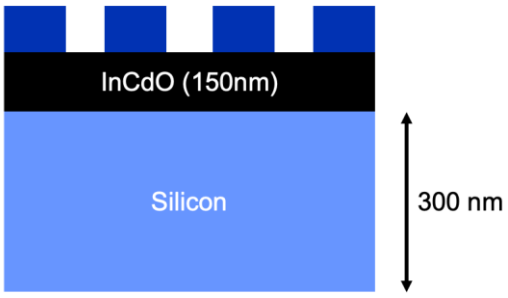

Figure 2.2: A-Si | ICO | Silicon model to study efficient coupling of light thin-film Silicon through HCGs.

These thickness-wavelength checkerboard plots offer many clues to the behavior of the system. The curved lines are due to the resonances of the dominant eigenmodes of HCG, whereas the strong vertical lines are from the eigenmodes of the thin-Silicon. The two classes of eigenmodes interact whenever they intersect, and the tell-tale signs of resonance can be identified by searching for anti-crossings. A few of such anti-crossings are circled in Fig. 2.3 (a). The plot in

Fig 2.3 (b) is a zoomed-in plot of one such anti-crossing. To verify that resonance does indeed occur at these anti-crossing points, we ran full-wave FDTD simulations for all the points circled in Fig. 2.3 (a), and the results are shown in Fig. 2.4. Each design point, with a particular thickness, period, duty cycle, and wavelength, showed a clear resonance in the silicon region, thus indicating strong coupling. We thus verified that these anti-crossings do indeed indicate strong coupling into the region of interest.

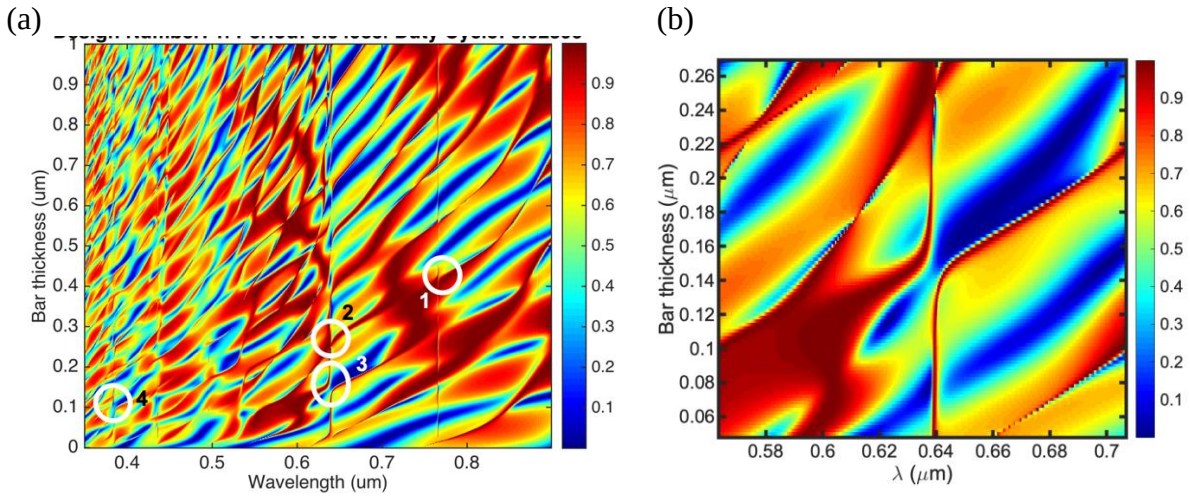

Figure 2.3: a) Thickness-wavelength reflection plot for an optimized design of the structure in the Fig. 2.2. Regions marked with a circle are where strong anti-crossing, and thus coupling occurs. b) a zoomed in plot of a clear anti-crossing region marked with the number 3 in plot (a).

Another way to analyze coupling is to directly look at the light absorption. Fundamentally, for a highly efficient solar cell, we want to maximize the absorption of light. A more direct way to analyze this is to extract absorption directly from the RCWA simulations. While the simulations only calculate the reflection and transmission, absorption for lossy materials can be estimated by subtracting the reflection and transmission by 1. To see the relation between the enhanced coupling and enhanced absorption, we run two simulations for the same structure. The first simulation calculates the reflection and assumes lossless materials by setting the imaginary refractive index, k, to 0. This allows us to see the characteristic anti-crossings. Next, after resetting the k to their original material data, we calculate the absorption plot. These two variations are plotted side-by-side in Fig. 2.5. Vertical eigenmodes of the waveguide are not visible in the Fig. 2.5 (b) because of loss in the material. However, as is evident from the plots, the anti-crossing regions in reflection plot result in higher absorption. To further validate this analysis, we calculate absorption with the more rigorous and time consuming FDTD simulations and compare them with RCWA simulations. Fig 2.6 shows that the plots obtained through RCWA and FDTD methods correlate well. They also show the impact of HCG in enhancing the absorption, especially towards the red side of the spectrum.

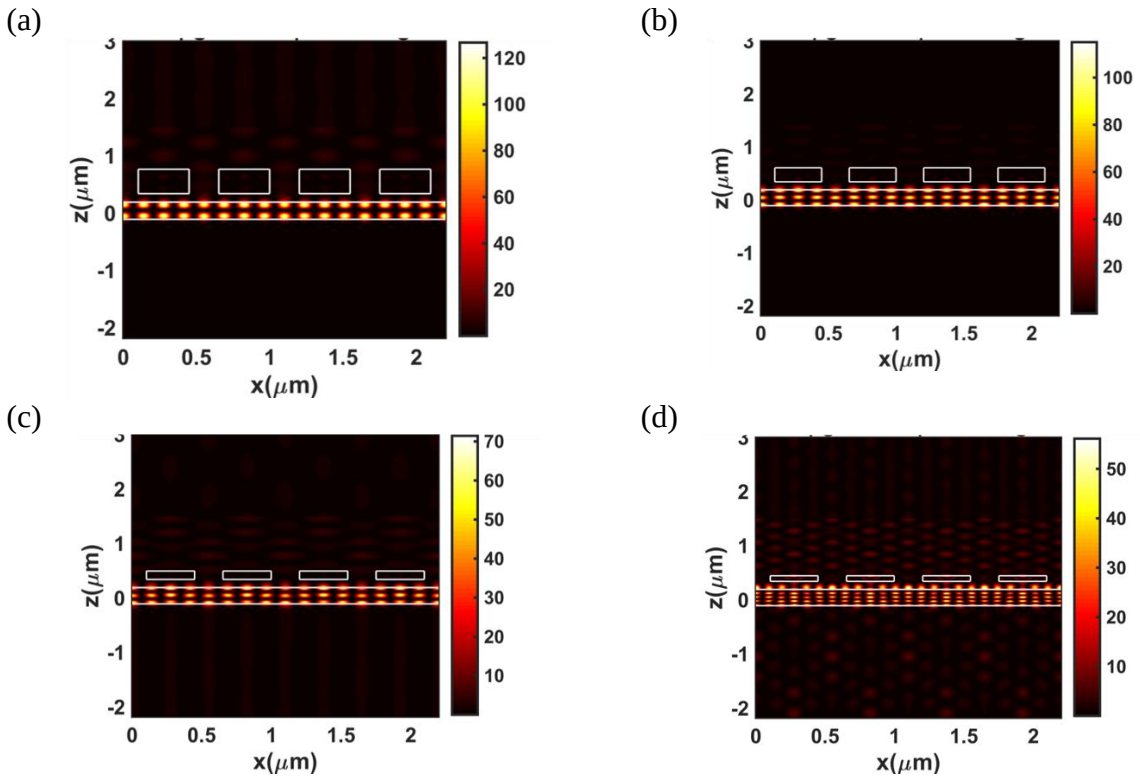

Figure 2.4: FDTD simulations showing clear resonance in the Silicon slab. These simulations were performed at regions marked in Fig. 2.3 as 1, 2, 3 and 4, respectively.

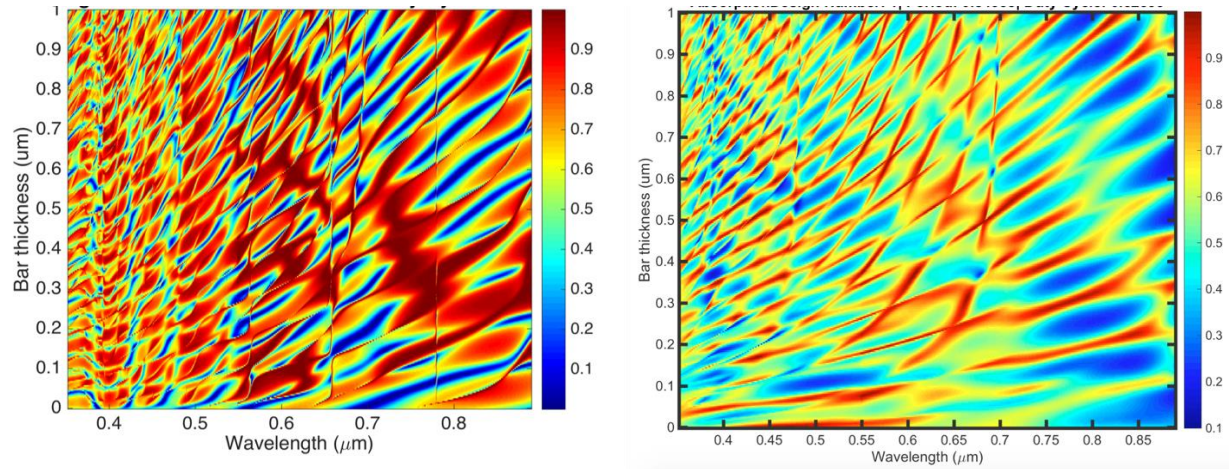

Figure 2.5: A comparison of reflection and absorption plots for the same structure. High absorption regions are strongly correlated with the anti-crossing in the reflection plot.

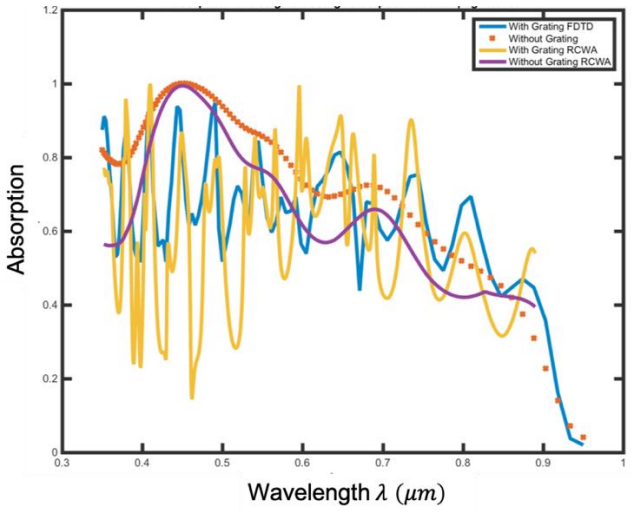

Figure 2.6: A comparison of absorptions obtained with FDTD and RCWA simulations for both with and without gratings. The RCWA simulations give a good approximation of the more time consuming FDTD simulations.

Since we are interested in energy harvested from the sun, we have to analyze the absorption of solar light. The plots in Fig. 2.6 and Fig. 2.7 (b) analyze how white light, with equal intensities across the spectrum, is absorbed by particular structures, but such plots need to be combined with the solar spectrum. The AM1.5 spectrum is an averaged solar spectrum and is the industry standard for testing and rating solar cells. The AM1.5 solar spectrum is plotted up to the band edge of Indium Phosphide (InP) in Fig. 2.7 (a), as we analyze the absorption of solar spectrum for optimized InP solar cells. In Fig. 2.7 (b), we compare the absorption of p-polarized white light by an optimized HCG | Indium Tin Oxide (ITO) | InP solar cell structure, with and without the HCGs. The optimized parameters for the structure are the following: HCG thickness = 0.1061 μm, HCG period: 0.549 μm, HCG duty cycle: 24.7%, ITO thickness: 150 nm, and InP thickness: 300 nm. The absorption of solar light can be calculated by simply evaluating the product of solar spectrum and the absorption of white light, as plotted in Fig. 2.7 (c). The short circuit current density (J_{sc}) can be calculated by integrating the absorption curve and allows us to directly quantify the impact of HCG on J_{sc}. In this particular case, the ratio of J_{sc} for the InP cell with and without the HCG is 1.127, and thus the HCGs enhance the efficiency by 12.7%.

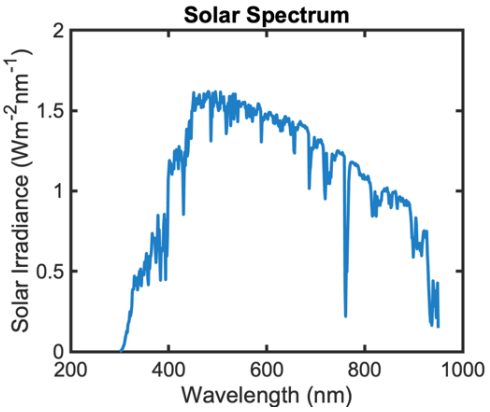

(a)

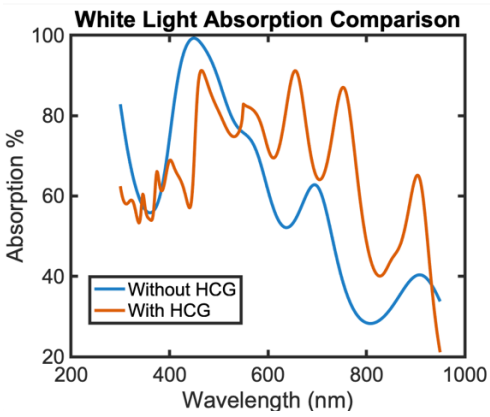

(b)

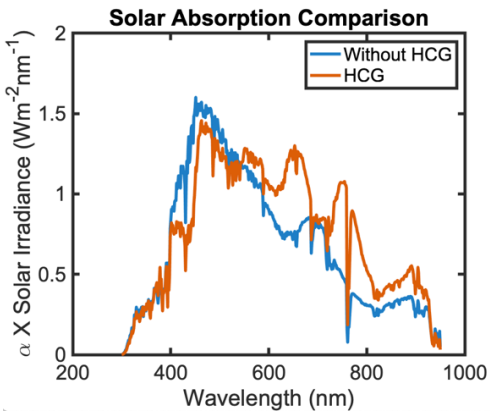

(c)

Figure 2.7: a) AM1.5: the spectrum of light from the sun. b) Absorptivity of white light by the optimized structure with and without the HCG. c) Absorptivity of the solar spectrum by the structure with and without the HCG.

2.3 Reflection Spectrum to Color

Optimizing for colors is the other important dimension of colorful and efficient solar cells. As we discuss in the introduction, colors result from light that is reflected from a structure. Reflection spectrum can be obtained from RCWA or FDTD simulations, but what is then needed is to convert the reflection spectrum into colors. Humans perceive colors through photoreceptor 'cones' in the retina of the eye. The three types of cones: Long, Medium and Short, have overlapping sensitivities to different wavelengths, but are associated with their most sensitive colors: red, green and blue for Long, Medium and Short cones. Mathematical functions have been developed and improved over the years to emulate the cones in the eye. One such formulation that is commonly used is the CIE 1931 Standard Observer [32], developed to match the 2° fovea of the eye. The three color matching functions are plotted in Fig 2.8 (a). Reflected color can be estimated by taking the overlap integral of a particular reflection spectrum with the three color matching functions. The three overlap values give x, y, and z coordinates, that can

then be used to find the color through the standard chromaticity diagram plotted in Fig. 2.8 (b), for a particular luminosity. This method was also used to calculate colors in another similar application of the HCG for tunable coloration [33].

Now that we have discussed the mechanism of getting color from reflection spectrum, it is useful to get a qualitative understanding of how the colors are related to different types of reflection spectrum. To do so, in Fig. 2.9 we plot three hypothetical reflection spectrums along with their associated colors, calculated with the method discussed in this section. The first and second spectrums both have the same center wavelength, but since the second spectrum has larger spread, the color looks duller than it does for the first spectrum. Thus, very sharp narrow-band reflections are preferred for vibrant colors. Furthermore, colors beyond the red, green and blue, require reflection spectrums with multiple peaks, as depicted with the third spectrum in Fig. 2.9 (a). The spread is the same as that in the first spectrum, but the two components of the spectrum result in the vibrant purple color.

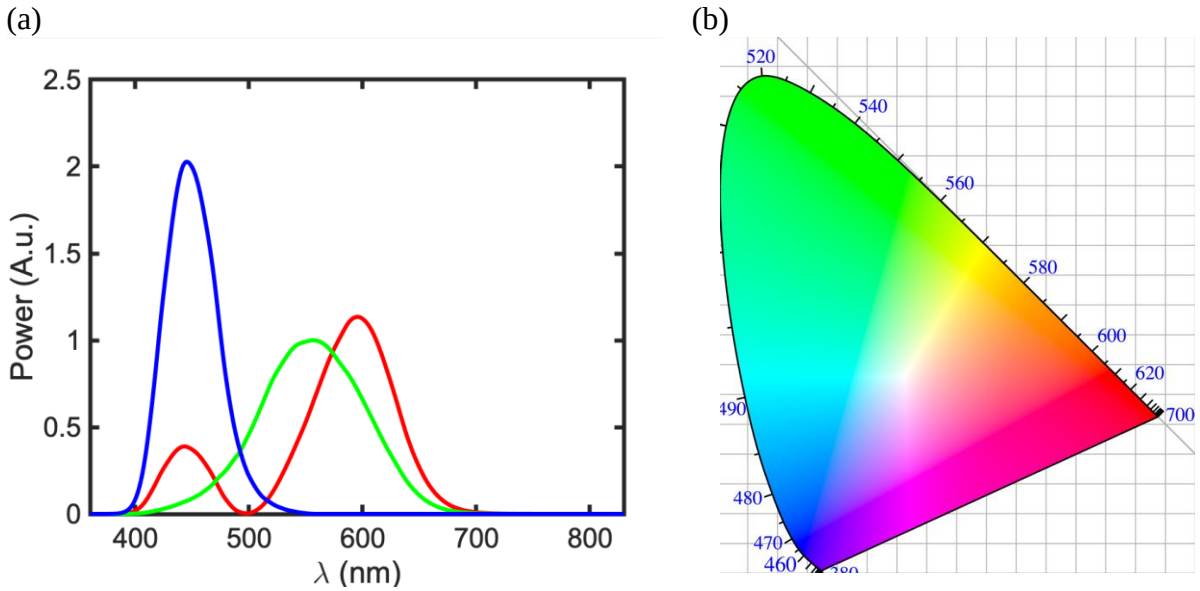

Figure 2.8: a) The red, green and blue (x, y and z) CIE 1931 color matching functions. b) A standard matching CIE 1931 chromaticity diagram plotted for a particular luminosity.

(a)

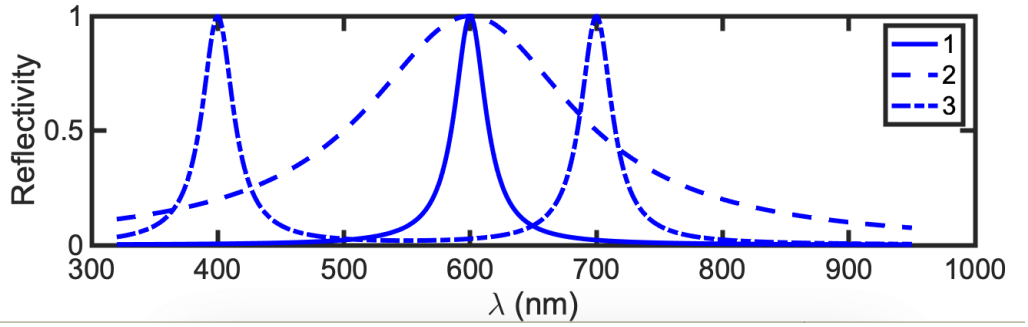

(b)

Figure 2.9: a) Three hypothetical spectrums, and their corresponding colors in (b).

2.4 Colorful Perovskite Solar Cells

We now use the principles developed above to design colorful and efficient Perovskite solar cells and show preliminary experimental results. As was mentioned in the introduction in Chapter 1, Perovskite solar cells are lead-based hybrid organic-inorganic solar cells. Their high efficiencies, low-cost and ease of manufacturability make them very attractive. Researchers have developed ways to make the cells look colorful, but have done so at a considerable loss in efficiencies [9], [10], [34]. Here, we explore the use HCG to achieve this objective.

We start with a discussion of the material layers in a Perovskite solar cell structure. Perovskite is a crystal type and has many variations. We use the Methylammonium Lead Iodide ($CH_3NH_3PbI_3$), also referred as $MAPbI_3$, based solar cells due to their high efficiency [35]–[37]. The full material stack for these kind of Perovskite cells is illustrated in Fig. 2.10. Fluorine-doped tin oxide (FTO) coated glass is used as a transparent top electrode, and Gold (Au) is used as the back contact. To enhance the electrical conductivity, a layer of organic material doped with Li+ and Co3+ ions is used as the hole-transporting layer and is commonly referred by its molecular structure called Spiro. Similarly, Titanium Dioxide (TiO_2) is used as an electron transport layer. The optical properties that we used in our RCWA and FDTD simulations for all these layers were taken from a published result [38].

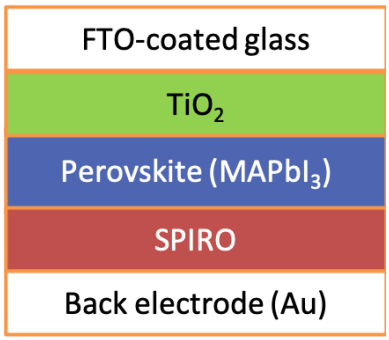

Figure 2.10: Material stacks of a Methylammonium Lead Iodide ($CH_3NH_3PbI_3$) based Perovskite solar cell structure.

To test our idea, we first optimized the HCG for a simplified $MAPbI_3$ structure, without Spiro and Au. The thickness of FTO, TiO_2 and the Perovskite layers were fixed, and the design parameters of the HCG were optimized, similar to the method in Section 2.2. The resulting FDTD simulations, shown in Fig. 2.12 (b), show the enhanced coupling of TM light due to HCG, and is in stark contrast to the structure without the A-Si HCGs. We further investigated the impact of HCGs by measuring the Photoluminescence (PL) of Perovskite layer, with and without optimized HCGs, and the results are shown in Figure 2.13. The PL for samples with A-Si HCGs shows an enhancement of 24% for p-polarized light, thus verifying he veracity of our approach.

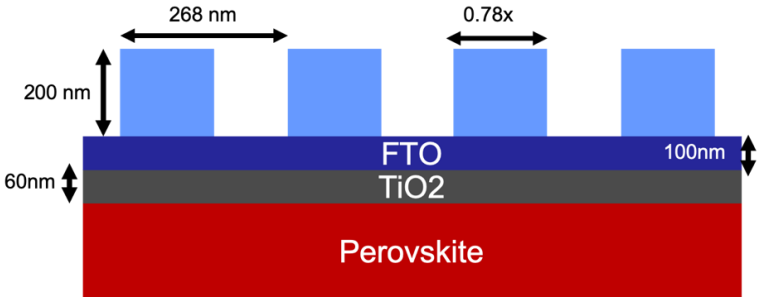

Figure 2.11: Optimized structure for the simplified Perovskite structure with HCG.

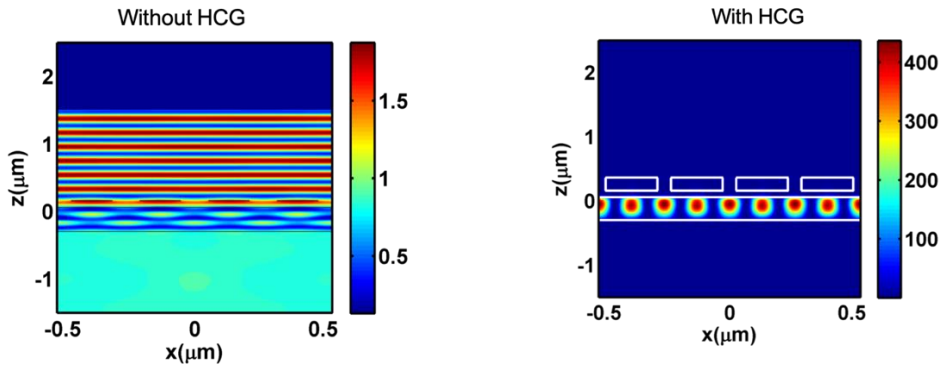

Figure 2.12: FDTD simulations showing enhanced coupling for structure in 2.11, a) without HCG and b) with HCGs.

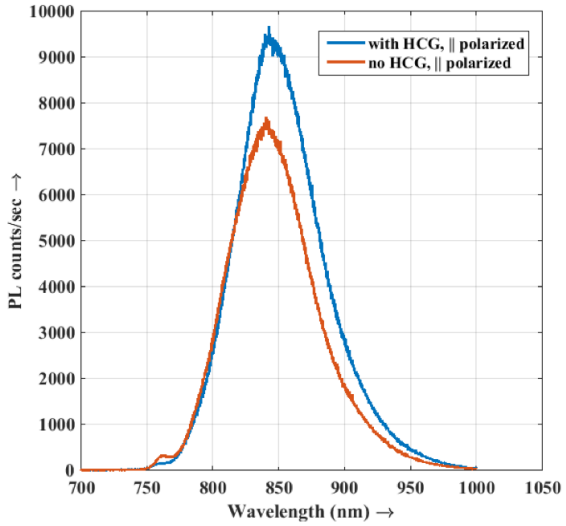

Figure 2.13: Photoluminescence (PL) of $MAPbI_3$, with and without optimized HCGs,

Having confirmed the principle, we then optimized the entire A-Si HCG integrated solar cell structure. The simulation stack is shown in Fig 2.14 (a). The A-Si HCGs were designed to be embedded inside the mesoporous TiO_2 (M-TiO_2) layer and were separated from the Perovskite layer with a finite M-TiO_2 thickness, t_b. The parameters t_b, t_g, Period Λ and duty cycle were all tuned to simultaneously obtain narrow band reflections for color, and enhanced coupling at other wavelengths. As shown in Fig. 2.14 (b), the loss in absorption, due to the narrowband reflections, is partially recovered by enhanced coupling at other wavelengths. This particular optimization provided yellow color with just about 5% loss in efficiency. To verify that the absorption enhancement was indeed because of HCG-enabled coupling, we ran FDTD simulations at 540 nm, and the results shown in Fig. 2.15 show clear evidence of coupling.

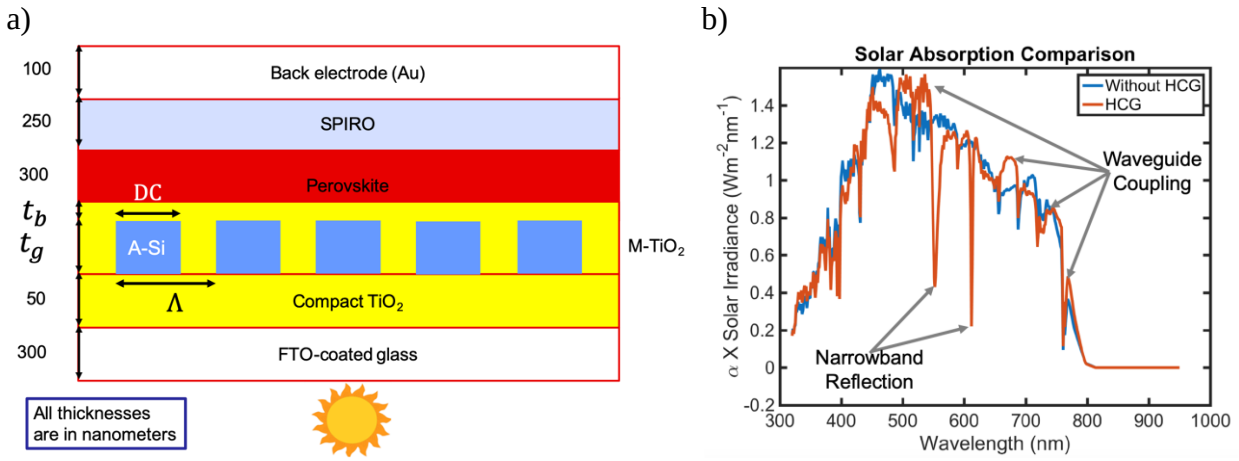

Figure 2.14: a) A schematic of A-Si embedded Perovskite solar cell stack. The design parameters were tuned to get simultaneous reflection and enhanced coupling. b) Absorption of the solar light with and without an optimized parameter of the HCG.

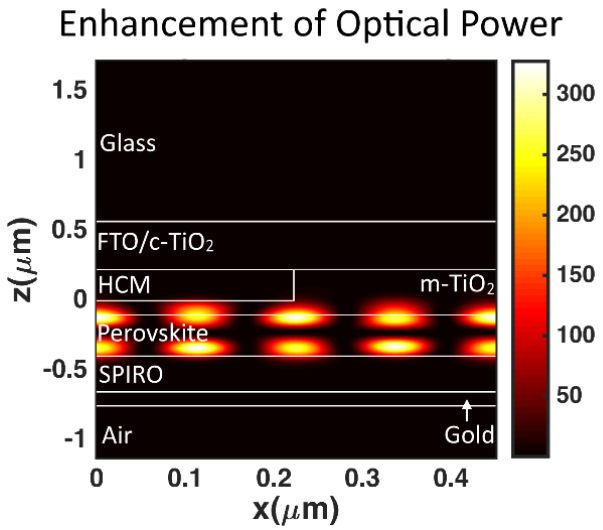

Figure 2.15: FDTD simulation at 540 nm for the design in Fig. 2.14 verifying that the enhanced absorption is indeed due to coupling of light into the Perovskite region.

To tune the color, we would have to change at least one of four tunable parameters. The HCG thickness and the M-TiO_2 thickness are determined by the deposition steps, and thus cannot vary from sample to sample on the same wafer. The period and duty cycle of the HCG, however, are determined by the lithography step, and are easy to vary. We optimize our parameters together and arrive at classes of optimized structures with vibrant colors and small losses in efficiency, as shown in Fig 2.16. We show results for various period and thickness of the HCG, and plot the color, in Fig 2.16 (a), and the relative impact on J_{sc} in Fig. 2.16 (b) for solar spectrum incident at 45°. The results are reasonable because the relative absorption, with and without HCG, converge

to 1 as the thickness of HCG converge to zero. As the graphs show, we can obtain colors from pink to green to purple, and tune them with varying period, but with a loss of up to 10% in efficiency. Later in this chapter we explore alternative designs with SiO_2 HCG that give colors for even smaller losses in efficiencies.

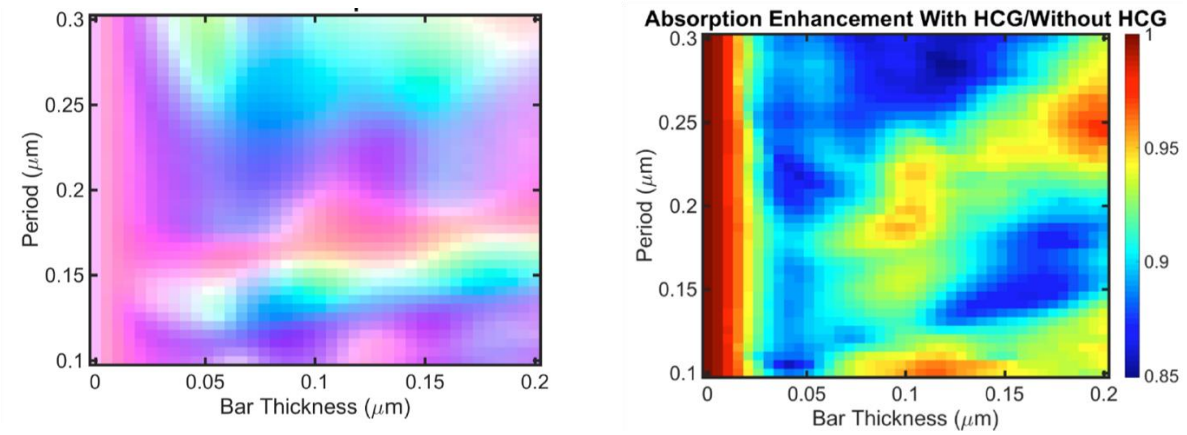

Figure 2.16: Simulated color in (a) and relative absorption in (b) for solar light incident at 45° on the optimized $MAPbI_3$ Perovskite solar cell with A-Si HCG.

To evaluate if it is feasible to embed HCG inside the M-TiO_2 layer of a Perovskite solar cell, we fabricated the entire solar cell structure. This fabrication was done together with Dr. Jonas Kapraun and our collaborator, Dr. Firdaus Bin Suhaimi, from Nanyang Technological University (NTU) in Singapore, as part of the Singapore-Berkeley Research Initiative for Sustainable Energy (SinBeRISE) program. The structure starts with FTO-coated glass that is purchased from vendors, and our collaborators at NTU first deposit compact-TiO_2 at 450 °C through spray pyrolysis. We then deposit Amorphous-Silicon (A-Si) through Chemical Vapor Deposition (CVD) at temperatures lower than 350 °C, and typically at 300 °C. Long exposures to temperatures above 350 °C flake the compact-TiO_2 coating, and therefore it is important to deposit below this temperature. The A-Si is patterned by standard photolithography process: depositing, exposing, and developing photoresist, and etching the A-Si layer. The M-TiO_2 solution is freshly prepared and spun on to the device through spin-coating at 450 °C. Similarly, the Perovskite ($MAPbI_3$) solution is also freshly prepared and spin-coated at 70-100 °C. The SPIRO solution is also spin-coated, but at room-temperature. And finally, Gold is deposited with thermal evaporation, and patterned with photolithography and lift-off techniques. For an equitable comparison, we fabricated the Perovskite solar cells both with and without the HCG, together and side-by-side. These processing steps are summarized in Fig. 2.17.

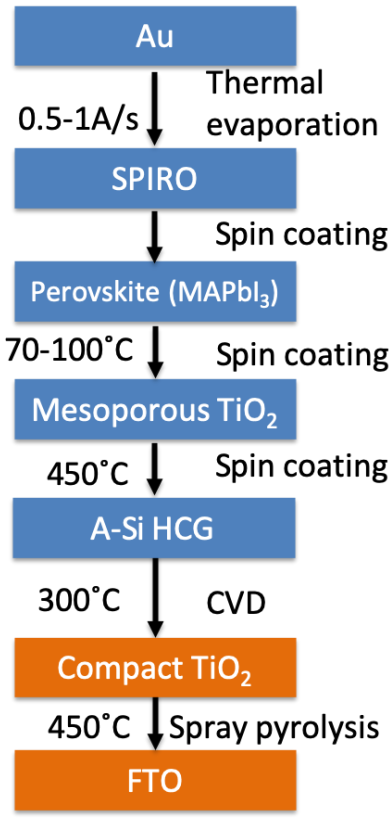

Figure 2.17: Summary of fabrication steps for a full stack $MAPbI_3$ Perovskite solar cell with HCGs. Process steps in orange were done by vendors or collaborators.

We use these fabricated structures to analyze our hypothesis. In our simulations, we assume that the M-TiO2 is conformally deposited over the A-Si gratings, and to verify this assumption, we took cross-sectional Scanning Electron Microscopy (SEM) images. The SEM shown in Fig 2.8 (a) verifies that the deposition is indeed conformal. In Fig. 2.8 (b), we show three 2x2 cm^2 $MAPbI_3$ Perovskite solar cells that were fabricated together. On the top left corner is a cell that was fabricated without gratings, and thus looks black. The other two colorful cells were fabricated with A-Si gratings, with a period of 2 μm. The colors seen here are due to the first order reflection of light, and not because of the 0^{th} order reflection discussed in the proceeding paragraphs. But these experiments give us a sense of how the gratings impact the short-circuit current and the fill factor. The solar IV curve, taken under a commercial solar simulator that emulates the AM 1.5 spectrum of the sun, is plotted in Fig. 2.19 for cells fabricated together, with and without the HCGs. We see that the cells with the HCG are slightly more efficient, but the performance of the two cells is comparable. Also, notable here is the slightly worse fill factor of the cells with the HCGs that can be attributed to the restricted electron flow due to the HCGs, but is a topic that is beyond the scope of this dissertation. While these experiments are not done at the designed periods of HCGs that are discussed in the previous paragraphs, they show the potential and promise of HCG-integrated Perovskite solar cells.

(a) (b)

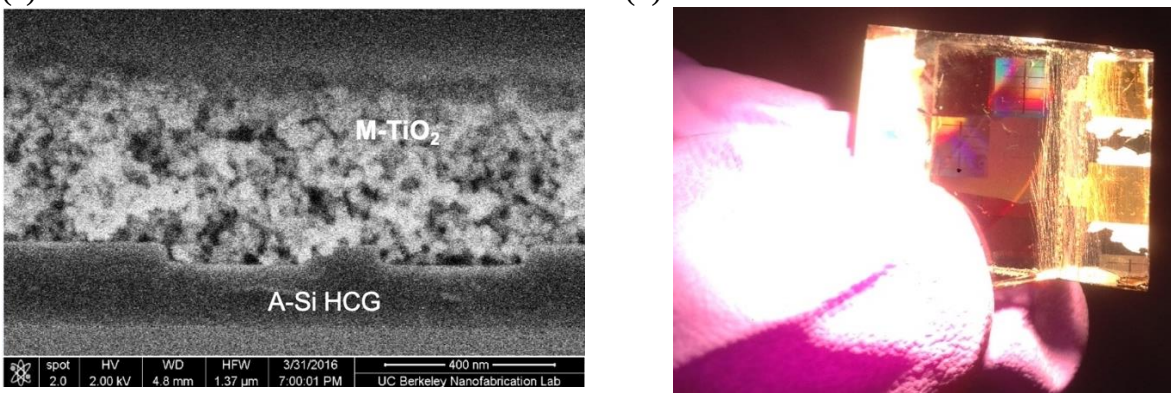

Figure 2.18: a) cross-sectional SEM of M-TiO_2 deposition on A-Si HCG. b) Three fully fabricated $MAPbI_3$ Perovskite solar cells. The black cell on the top left corner is without any gratings, while the other two colorful cells on the diagonal have A-Si HCGs with a period of 2 μm.

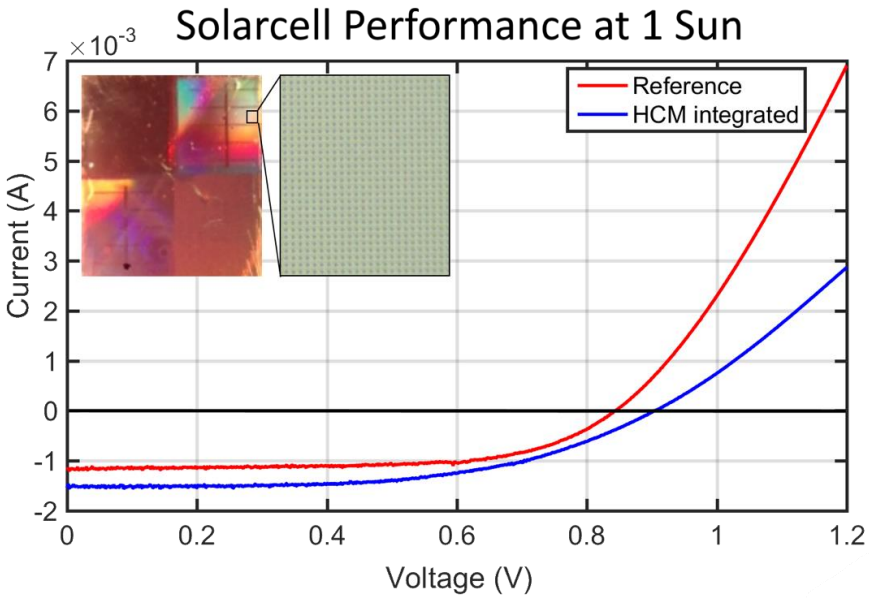

Figure 2.19: A comparison of the IV curve for $MAPbI_3$ Perovskite solar cells with and without the HCGs. The cells shown in the inset are the same as those discussed in Figure 2.18.

Another design parameter is the material of the HCGs. The HCG material for all our previous designs was Amorphous Silicon, because of its higher refractive index ($n \approx 3.5$) than the surrounding materials: TiO2 ($n \approx 2.2$), and air ($n \approx 1$). The materials are dispersive with wavelength, but these refractive index number give a sense of the contrast between the materials. To benefit from the unique properties of HCGs, we need to have a high contrast, and not necessarily, a higher index than the surroundings. Configurations where the HCG has a high contrast but lower index than the surrounding materials have been explored in the past [39]. A

disadvantage of using A-Si is that it is lossy, and thus decreases the efficiency when used in solar cells. SiO_2 ($n \approx 1.5$). is a viable alternative because it is lossless and has a high contrast to TiO2 ($n \approx 2.2$). The optimization design for SiO_2 HCG enhanced $MAPbI_3$ Perovskite solar cells is shown in Fig. 2.20 and was optimized with the same strategy as stated in the previous paragraphs. The perceived color and relative J_{sc} results are shown in Fig. 2.21 for different thickness and periods of HCG. These two plots show that we can chose to operate at either of two modalities: 1) Enhanced efficiencies with little reflection and dull colors, or 2) Colorful cells with tunable colors, but with a degradation in efficiency. The increased efficiency in the first modality can be understood by looking at the simulated absorbed solar spectrum with and without HCG, plotted in Fig. 2.22. The simulated current density with HCG is higher because of enhanced coupling at many wavelengths. Alternatively, an example of narrow band reflections and some enhanced coupling has already been given in Fig. 2.14 (b). The region boxed in pink in Fig. 2.21 is an example of the second modality, where colors can be tuned across the spectrum from blue to pink, by simply changing the HCG period. These colors come at the cost of up to 4% degradation in the current density. These results are far better than the A-Si HCG designs discussed above, and any other simulated or experimental results in literature, and thus very promising for the realization of colorful and efficient solar cells.

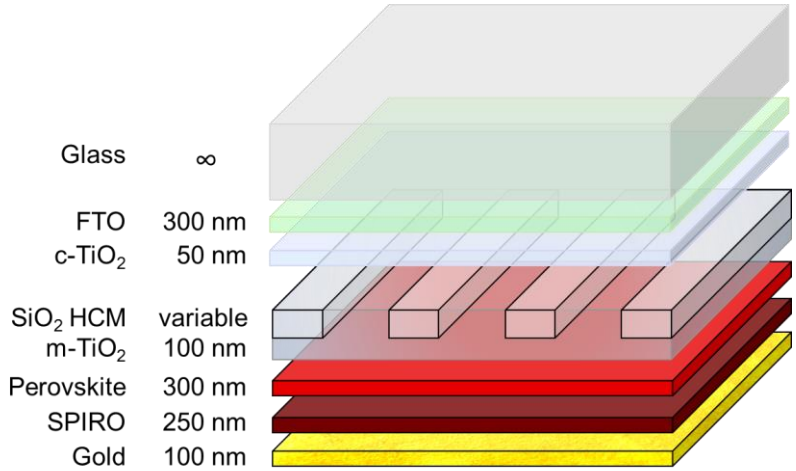

Figure 2.20: A schematic of Perovskite solar cell stack with embedded SiO_2-HCGs. The design parameters were tuned to get simultaneous reflection and enhanced coupling for light incident at 45° from top.

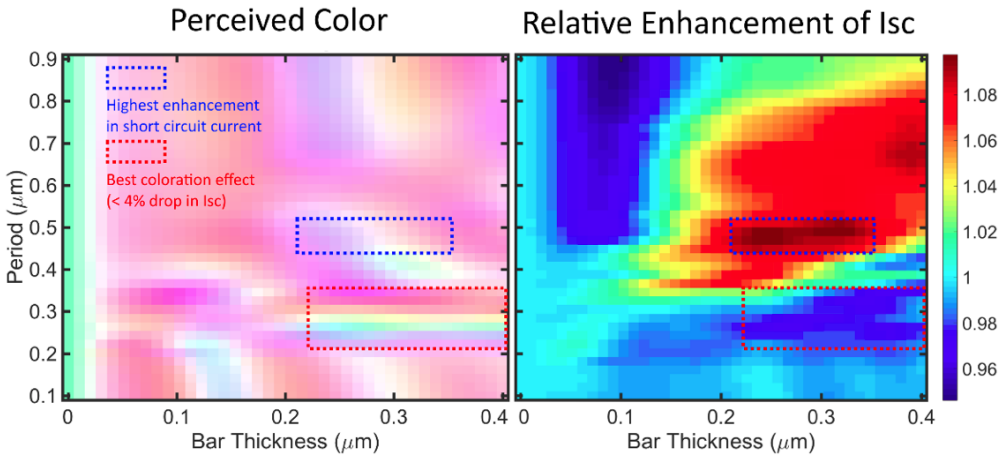

Figure 2.21: Simulated perceived color and relative J_{sc} results are shown in Fig. 2.21 for different thickness and periods of optimized solar cell designs.

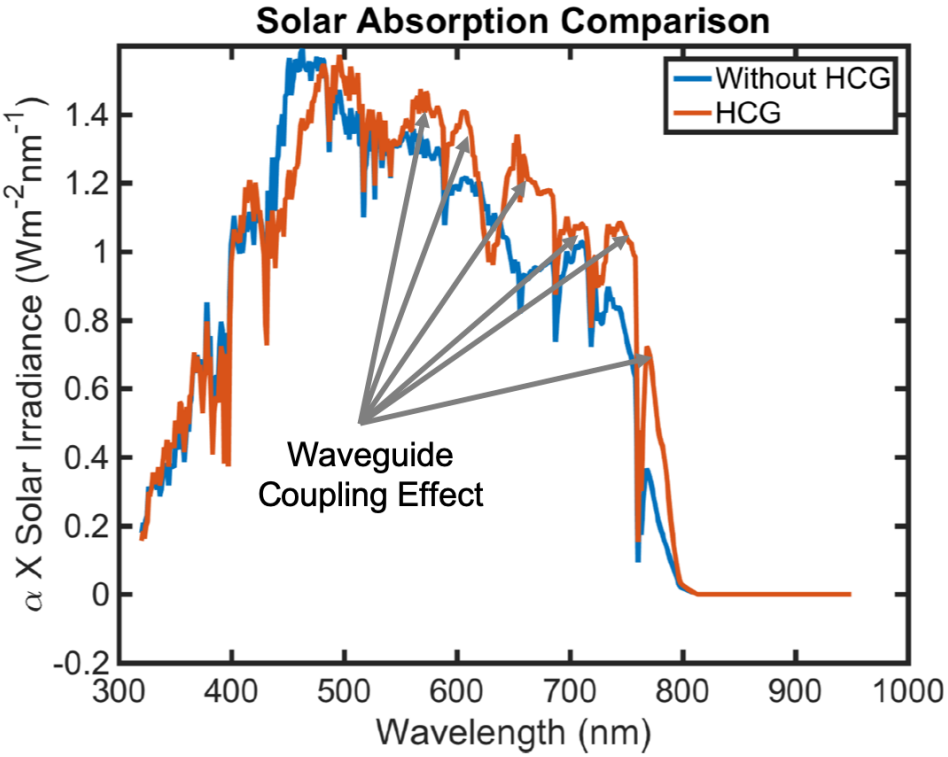

Figure 2.22: An example of a design with SiO2-HCG enabled improved short circuit current density. The absorption is enhanced at many wavelengths.

2.5 Polarization and Incidence Angle Sensitivity

The one-dimensional HCG inherently have a polarization sensitivity, and gratings, in general, are sensitive to the angle of incidence. Most of the designs in this chapter were specifically optimized for p-polarized light. While it is challenging to optimize structures to make them polarization insensitive with 1D HCG, it is possible to make the performance for s-polarized and p-polarized similar. As an example, we optimized an A-Si HCG | ITO | InP solar cell structure for enhanced solar light absorption at both p and s polarizations. The results for the ratio of absorption with and without the HCGs are shown in Fig. 2.23. While there are stark differences between the two polarizations, the area marked with the black square highlights a region of comparable enhancement for both s and p polarizations. It is also possible to make these designs polarization independent by transitioning to two-dimensional HCG [40].

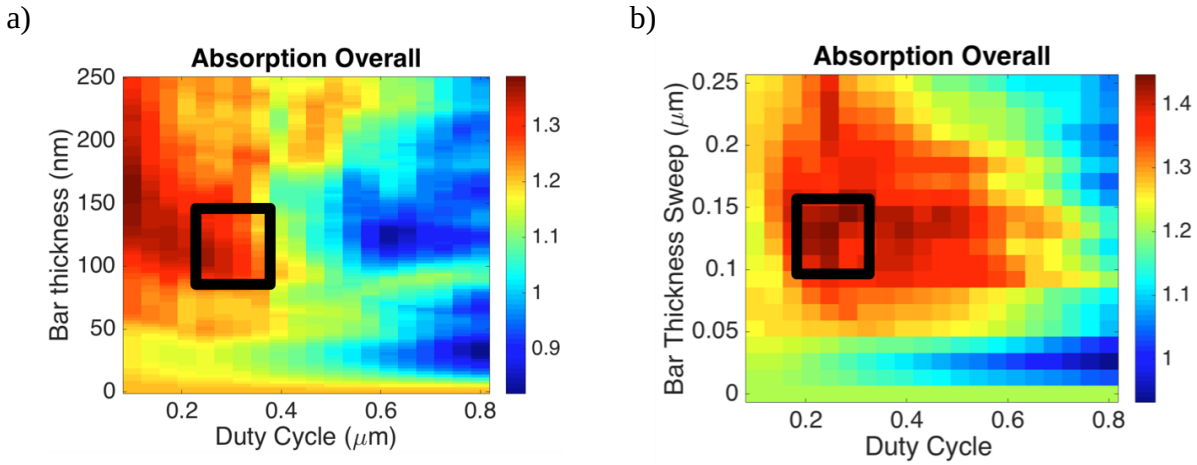

Figure 2.23: Relative absorption of optimized A-Si HCG | ITO | InP with and without HCG, optimized for enhanced solar light absorption at both a) p-polarized solar light and b) s-polarized solar light.

We also found the simulated perceived color to be sensitive to the angle of incidence. Our designs were optimized for 45° incident solar light, and strategies to design wide-angle HCG [41], [42] were not explored. However, for completion, we are adding an example of how the perceived color for designs in Fig. 2.24 responds to different angles of incidence. All the colors lie on a diagonal line, and that verifies that our designs suppressed the leakage of light at higher orders. While the color does change, it still exhibits vibrant colors at other angles, and can be utilized to even make smart designs that look different at different angles.

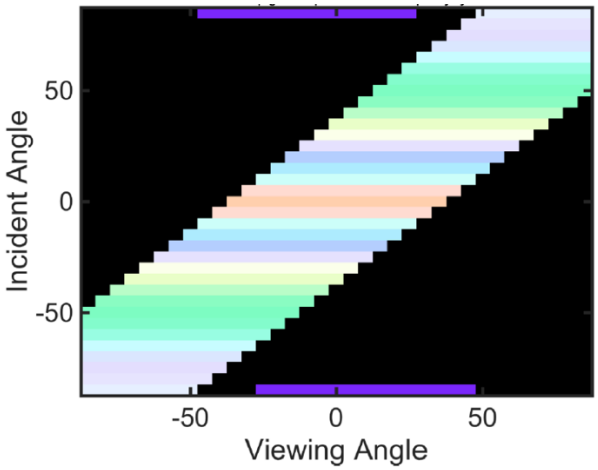

Figure 2.24: An example of the dependence of simulated perceived color for different angles of incidence

Chapter 3: Single-Wavelength Interferometer

Light waves accumulate phase as they travel in space and time. This information is often lost as only the intensity, and thus the amplitude, is detected on a photodetector. The principles of interference can be employed to measure the phase difference of two spatially and temporally coherent waves. If the behavior of one of the two waves can be controlled, the phase information of the other wave can be recovered. This technique gives us a way to meticulously quantify the propagation of light in space and time, however, it comes with its own set of limitations.

In this chapter, we look at the use of single wavelength interferometry for metrology and study its limitations. We carefully look at the theory to gain a concrete sense of how the accuracy is affected by factors like the laser phase noise and measurement technique, and how it can be made more robust.

3.1 Michelson Interferometers

An electric field of an electromagnetic wave can be represented by having an amplitude and phase: $\vec{E} = E_0 e^{j\phi}$. The phase encodes the propagation of light in space and time, and can be expressed as:

$$\phi = \int \omega dt + \int \vec{k} d\vec{r} = \omega t + \vec{k} \cdot \vec{r} = \omega t + k_x x + k_y y + k_z z \tag{3.1}$$

where $\omega = 2\pi/f$ is the temporal frequency, and $\left|\vec{k}\right| = \frac{\omega}{c} = \sqrt{k_x^2 + k_y^2 + k_z^2}$. When two spatially and temporally plane waves interfere, the intensity of the interference can be expressed as follows:

$$I = E_{o1}^2 + E_{02}^2 + 2E_{01}E_{02}\cos(\phi_1 - \phi_2) \tag{3.2}$$

where E_{o1} and $\phi_1$are the amplitude and phase of the first wave, and similarly, E_{o2} and ϕ_2 are the amplitude and phase of the second wave. Thus, the intensity of the interference signal not only encodes the amplitudes of the constituent waves, but also the difference of their phase. The traditional Michelson interferometer, proposed in 1891, first splits a single coherent light source into two separate paths, and then after letting the light propagate in the two paths, interferes them together. By controlling the length and conditions of one of the two paths, hereafter referred to as the *reference path*, useful deductions can be made about the other variable and unknown *sample path*.

Fig. 3.1(a) shows a schematic of a free-space Michelson interferometer, where E_0 is the amplitude of the laser, and $l_1/2$ and $l_2/2$ are the distances of the two mirrors to the beamsplitter. The intensity of light is split evenly between the two paths. The phase accumulated by the light due to the double pass from the beamsplitter to the top mirror is $\omega t + kl_1$, and the phase accumulated in the path to the right of the beamsplitter is $\omega t + kl_2$. The intensity of the interference can be expressed as the following:

$$I = \frac{1}{2}|E_0|^2 + \frac{1}{2}|E_0|^2\cos[k(l_1 - l_2)] = \frac{1}{2}|E_0|^2 + \frac{1}{2}|E_0|^2\cos[kd] \tag{3.3}$$

where $d = l_1 - l_2$. This is also illustrated through the fiber-based setup depicted in Fig. 3.1(b), where d represents the length difference of the two paths. Conversely, meaningful information about the path difference can be extracted by analyzing the argument of the cosine, *the phase of the interference*, $\phi = kd$. In section 3.3 of this chapter, we will discuss on how this phase can be extracted from the interferograms.

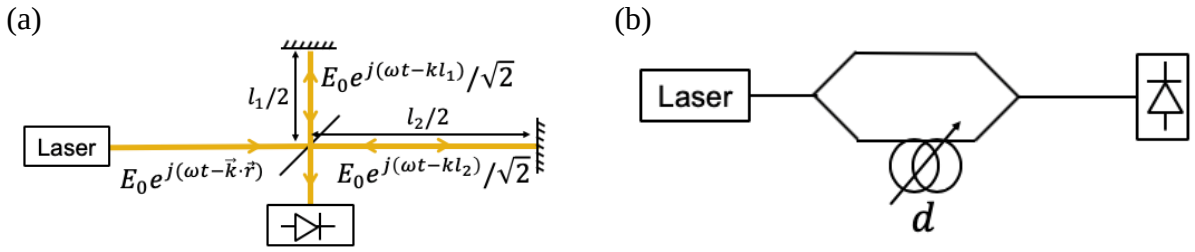

Figure 3.1: A traditional Michelson interferometer in (a) free space and (b) fiber-based setup.

The accuracy, or the depth resolution, simply depends on $\Delta\phi$, the accuracy with which this phase of the interference can be measured. Thus, the depth resolution, Δd, can be expressed as:

$$\Delta d = \frac{\Delta\phi}{k} = \Delta\phi \frac{2\pi}{\lambda} \tag{3.4}$$

However, since the phase has a periodicity of 2π, it can only be measured modulo 2π: $\phi_m = \phi \bmod 2\pi$. Hence, the measurement of the path difference, d_m, too is fundamentally ambiguous and can only be measured modulo λ.

$$d_m = d \bmod \lambda \tag{3.5}$$

Thus, the maximum unambiguous range for a single wavelength interferometer is λ.

3.2 Dependence on Laser Noise

Only coherent waves interfere, and this coherence requirement sets the spotlight on lasers, the light source that is used in the Michelson interferometer. Due to frequency and phase noise in lasers, the electric field is not just a simple perfect sinusoidal wave. This frequency and phase noise stems from intrinsic properties of the laser, primarily spontaneous emission, and extrinsic sources like temperature and current fluctuations [43].

In this section, we analyze how the laser phase noise, also denoted by the linewidth $\Delta\omega$, impacts the uncertainty in phase measurements, and how this uncertainty improves with time integration or averaging.

Redefining the E-field of our laser to include the phase noise, $\phi_p(t)$, we get:

$$E = E_0 e^{i\left(\omega_0 t + \phi_p(t)\right)} \tag{3.6}$$

Consequently, the interference current can be given as:

$$i(t,\tau) = |E(t) + E(t-\tau)|^2 = E_0^2 \left| e^{i\left(\omega_0 t + \phi_p(t)\right)} + e^{i\left(\omega_0 (t-\tau) + \phi_p(t-\tau)\right)} \right|^2 \tag{3.7}$$

Simplifying this equation,

$$i(t,\tau) = 2E_0^2 + 2E_0^2 \cos\left(\omega_0 \tau + \Delta\phi_p(t,\tau)\right) \tag{3.8}$$

where $\Delta\phi_p(t,\tau) = \phi_p(t) - \phi_p(t-\tau)$. The interferometric phase, ϕ_i, can be extracted from Eq. 3.6 using the techniques in Section 3.3, and can be expressed as:

$$\phi_i = \omega_0 \tau + \Delta\phi_p(t,\tau) \tag{3.9}$$

Since phase noise fundamentally stems from a large number of independent spontaneous emission events, $\Delta\phi_p$ must be a zero-mean Gaussian random variable, and the uncertainty in ϕ_i would reduce with time averaging. Thus, the time-averaged phase that is measured can be expressed as:

$$\phi_m = \omega_0 \tau_m = \frac{1}{T}\int_0^T \phi_i \, dt = \omega_0 \tau + \frac{1}{\mathrm{T}}\int_0^{\mathrm{T}} \Delta\phi_p(t,\tau) \, dt \tag{3.10}$$

The phase-noise-limited difference between the measured phase and actual phase, $\delta\phi_{PN}$, can thus be expressed as:

$$\delta\phi_{PN} = \frac{1}{T\omega}\int_0^{\mathrm{T}} \Delta\phi_p(t,\tau) \, dt \tag{3.11}$$

Using the expression for the standard error for mean: $\sigma_{\bar{x}} = \frac{\sigma}{\sqrt{n}}$, the standard deviation of uncertainty in $\delta\phi_{PN}$, $\sigma_{\delta\phi_{\mathrm{PN}}}$,can be expressed as:

$$\sigma_{\delta\phi_{\mathrm{PN}}} = \frac{\sigma_{\Delta\phi_{\mathrm{p}}}}{\sqrt{f_S T}} \tag{3.12}$$

Where f_S is the sampling frequency, and T is the integration time. Eq 3.12 can be used to express the standard deviation of uncertainty in delay measurements, $\Delta\tau$, $\sigma_{\Delta\tau}$, as:

$$\sigma_{\Delta\tau} = \frac{1}{\omega}\frac{\sigma_{\Delta\phi_p}}{\sqrt{f_S T}} \tag{3.13}$$

We will thus take a slight detour to evaluate $\sigma_{\Delta\phi_p}$, and then return towards the end of this section to evaluate Eq. 3.13. Following the formulation in [44], we first write out the autocorrelation of $\Delta\phi_p(t,u)$, and express it in-terms of the autocorrection of $\phi_p(u)$:

$$\mathcal{R}_{\Delta\phi_p}(s,u) = \ < \Delta\phi_p(t,u)\Delta\phi_p(t-s,u) >_t \tag{3.14}$$

Where *s* is the shift variable. By expanding $\Delta\phi_p$, we obtain:

$$\mathcal{R}_{\Delta\phi_p}(s,u) =< \left[\phi_p(t-u) - \phi_p(t)\right]\left[\phi_p(t-u-s) - \phi_p(t-s)\right] >_t \tag{3.15}$$

By multiplying out the expression and casting in-terms of the autocorrelation of ϕ_p, $\mathcal{R}_{\phi_p}$, we obtain:

$$\mathcal{R}_{\Delta\phi_p}(s,u) = \mathcal{R}_{\phi_p}(s) - \mathcal{R}_{\phi_p}(s-u) - \mathcal{R}_{\phi_p}(s+u) + \mathcal{R}_{\phi_p}(s) \tag{3.16}$$

To find an expression for $\sigma_{\Delta\phi_p}$, we will first have to go through the intermediary step of finding the power spectrum density (PSD) of $\Delta\phi_p$. We do so by utilizing the Wiener-Khinchin theorem [45] that relates the power spectral density (PSD) and the autocorrelation of a variable x:

$$S_x = \mathcal{F}\left(\mathcal{R}_x(u)\right) = \int_{-\infty}^{\infty} \mathcal{R}_x(u) e^{-i\omega u} du \tag{3.17}$$

Expressing the Fourier transform of $\mathcal{R}_{\phi_p}(s)$ as $S_{\phi_n}(\omega)$, and knowing that the Fourier transform of a shifted function is multiplication with an exponential, the Fourier transform of Eq. 3.16 can be written as:

$$S_{\Delta\phi_p}(\omega,u) = S_{\phi_n}(\omega)\left(2 + e^{j\omega u} + e^{-j\omega u}\right) = 4S_{\phi_n}(\omega)\sin^2\left(\frac{\omega u}{2}\right) \tag{3.18}$$

The spectrum of phase noise, $S_{\dot{\phi}_p}(\omega)$, is flat and equal to a constant value denoted by the linewidth $\Delta\omega$ [46].

$$S_{\dot{\phi}_p}(\omega) = \Delta\omega \tag{3.19}$$

Using this definition, we write out the expression for $S_{\phi_n}(\omega)$, and solve Eq. 3.18:

$$S_{\phi_n}(\omega) = \omega^2 S_{\dot{\phi}_p}(\omega) = \omega^2\Delta\omega \tag{3.20}$$

$$S_{\Delta\phi_p}(\omega,u) = 4u^2\omega^2\,\mathrm{sinc}^2\left(\frac{\omega u}{2}\right)\Delta\omega \tag{3.21}$$

Now we return to the objective of finding an expression for $\sigma_{\Delta\phi_p}$, and do so by integrating the PSD in Eq. 3.21.

$$\sigma^2_{\Delta\phi_p}(u) = \frac{1}{2\pi}\int_{-\infty}^{\infty} S_{\Delta\phi_p}(\omega, u)\, d\omega \tag{3.22}$$

$$\sigma^2_{\Delta\phi_p}(u) = \frac{1}{2\pi}\Delta\omega \int_{-\infty}^{\infty} 4u^2\omega^2\, \mathrm{sinc}^2\left(\frac{\omega u}{2}\right) d\omega \tag{3.23}$$

$$\sigma^2_{\Delta\phi_p}(u) = |u|\Delta\omega \tag{3.24}$$

Plugging the results of this equation into Eq. 3.12, we arrive at the phase-noise limited error in integrated measured phase, $\sigma_{\delta\phi_{PN}}$.

$$\sigma_{\delta\phi_{PN}}(T, z) = \frac{z\Delta\omega}{c\sqrt{f_S T}} \tag{3.25}$$

Where z is the optical path length difference that is measured, and c is the speed of light. Similarly, we use the results from Eq. 3.24 and Eq. 3.13 to evaluate the phase-noise limited accuracy, $\sigma_{\Delta z_{PN}}$:

$$\sigma_{\Delta z_{PN}}(T, z) = \frac{1}{k\sqrt{T f_S}}\sqrt{\frac{z}{c\tau_c}} \tag{3.26}$$

Where z is the optical path length difference that is measured, T is the integration time, f_s is sampling frequency, and $k = \omega/c$ is the wave-vetor. The coherence time, τ_c, is defined as $\frac{1}{\Delta\omega}$, and $\Delta\omega$ is the linewidth of the laser. For a laser operating at 1550 nm with a 100 KHz linewidth, the plot between the uncertainty $\sigma_{\Delta z}$, measured with sampling frequency of 1 GHz and integrated over 1 μs, and z is given in Fig. 3.2. As expected, the uncertainty is higher for longer measured distances. However, even for a small integration time of 1 μs, the uncertainty only exceeds $2\pi/1550$ for distances over 61.2 m. Therefore, for interferometry done at 1550 nm, the phase-noise limited single sigma accuracy is within a nanometer for measured distances that are smaller than 61.2 m. To extend the range for phase-noise limited sub-nanometer accuracy, we will simply have to integrate longer, as evident in Eq. 3.27 and plotted in Fig. 3.3 for a 100 KHz linewidth laser and a sampling frequency of 1 GHz.

$$T_{required} > \left[\frac{z\Delta\omega}{c\sqrt{f_s}}\frac{1550}{2\pi}\right]^2 \tag{3.27}$$

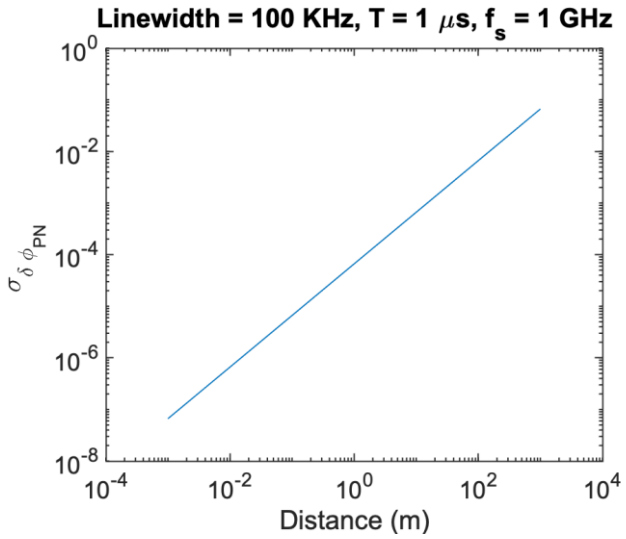

Figure 3.2: The phase-noise-limited error in measurement phase is plotted against the distance measured. Laser linewidth is assumed to be 100 KHz, and the measured phase is integrated for 1 μs at sampling frequency of 1 GHz.

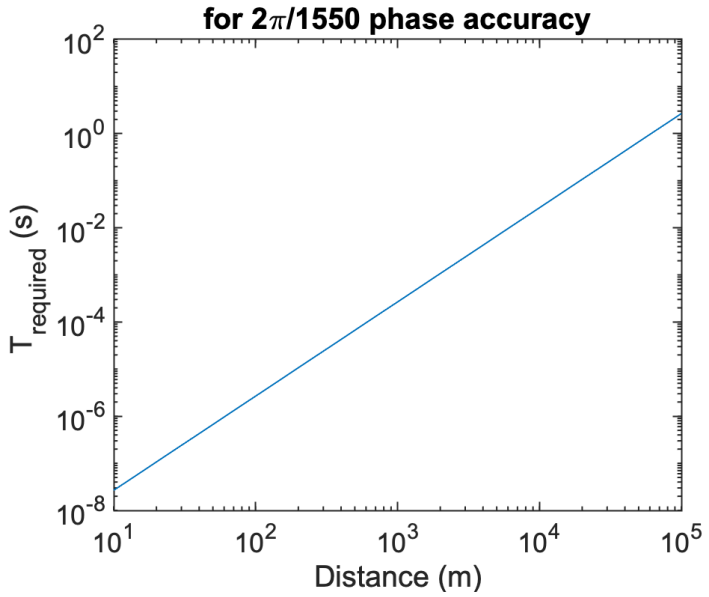

Figure 3.3: The integration time required as a function of measured distance, for a $2\pi/1550$ phase-noise limited measured phase sigma accuracy. $f_s = 1\ GHz$, laser linewidth is assumed to be 100 KHz.

However, just analyzing the phase-noise limited accuracy is not sufficient. Rather, we also have to look at the errors in phase resulting from the way the interferometric phase is extracted from the measured interferometric power. We look at those techniques in the next section of this chapter, and then later return in Section 5.5 to quantify the accuracy.

3.3 Extracting Interferometric Phase

The most useful component of an interferometric signal is the interferometric phase, ϕ, embedded in the cosine term of Eq. 3.1. Even if the interference signal is normalized with the measured powers from the sample and reference arm, the phase has to be extracted:

$$\phi = \operatorname{acos}\left(\frac{I_I - I_r - I_S}{2\sqrt{I_R I_s}}\right) \tag{3.28}$$

Where I_I is the interferometric intensity from Eq. 3.2, and I_r and I_s are the reference and sample intensities, measured separately by individually blocking the sample and reference arms respectively. Although ϕ is modulo 2π and is bijective for when the normalized distance, d/λ, is between 0 and 1, the cosine and arccosine functions are not bijective with ϕ, and thus do not have a one-to-one correspondence with the measured phase. The illustration is Fig 3.4 shows that within the $d = \lambda$ range, the same values of $\cos\phi$ and $\operatorname{acos}(\cos(\phi))$ correspond to two different distances, and are ambiguous on either side of the $d/\lambda = 0.5$ line. Thus, unless the ambiguity between these pair of values is resolved, the measured distance is ambiguous at a much smaller range than λ, and the range of the system is dependent on the starting distance.

(a)

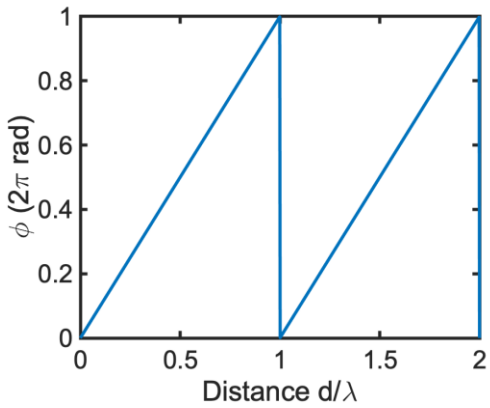

(b)

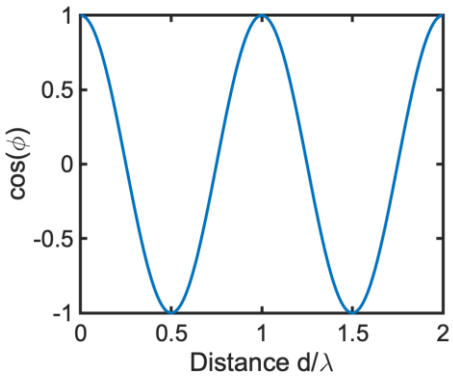

(c)

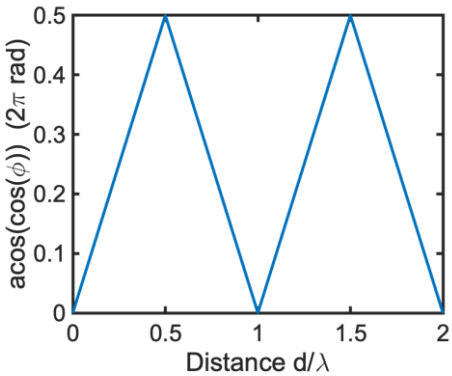

Figure 3.4: a) Phase ϕ as a function of the normalized measured distance d/λ wraps around at 2π. b) The cosine function is not bijective with ϕ and is thus ambiguous. c) similarly, the arccosine of the cosine function is also not bijective with ϕ

To resolve this ambiguity, we have to measure not just the value of the $\cos\phi$, but also its slope. To do so, we first added a Lithium Niobate phase modulator in the reference path to introduce a small known phase shift, θ, to the interferometric signal. The modulator was driven with a square wave with a small amplitude of 0.12 V and synchronized with the oscilloscope used to measure the photodetector current. The phase shift, corresponding to the small voltage applied to the phase modulator, is first calibrated, and then used to resolve the dual-value ambiguity. The setup we used in shown in Fig. 3.5. Mathematically, this added phase, θ, modifies Eq 3.2 in the following way:

$$I = E_{o1}^2 + E_{02}^2 + 2E_{01}E_{02}\cos(\phi + \theta) \tag{3.29}$$

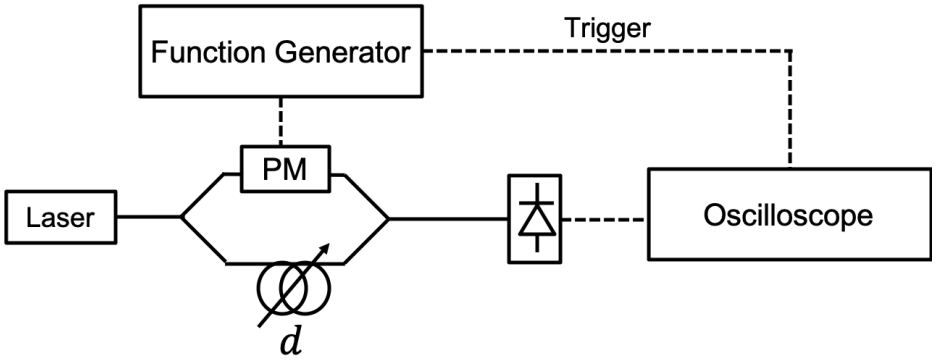

Figure 3.5: Setup to introduce a small phase shift to the interferometric signal. An electrical actuated phase modulator (PM) is added to the reference path and synchronized to the measurement setup via the trigger signal. Dotted lines indicate electrical signals whereas solid lines indicate optical signals.

Fig. 3.6 is an example from the experimental data on how the $\cos(\phi + \theta)$, for a stationary target, is modulated by the square wave driven phase modulator. The result of the small phase modulation on the cosine is one of four cases depicted in Fig. 3.7. Green circles indicate the initial pre phase-shifted cosine value, and the black circles indicate the post phase-shifted value. Filled circles indicate the positions on unambiguous phase, whereas hollow circles indicate the values projected onto the measured ambiguous cosine. The depictions assume that $\theta > 0$. If the measured phase shift is θ, and the cosine value increases, this indicates case 1, and the initial position is resolved to lie in the first half of d/λ. Similarly, if the measured phase shift is θ, but the cosine value decreases, this indicates that the original position was in the second half of d/λ. The more unlikely edge cases are depicted in Fig 3.7 (c) and (d) and are a consequence of the phase-shift perturbing the interferometric phase across the trough or peak of the cosine curve. But such cases are easy to catch because the measured phase shift is smaller than the intended phase shift, and cases three and four, illustrated in Fig 3.7 (c) and Fig. 3.7 (d) can be resolved by identifying if the cosine value increased or decreased. A small phase shift value makes the occurrence of these edge cases increasingly unlikely and is therefore favorable in such a configuration.

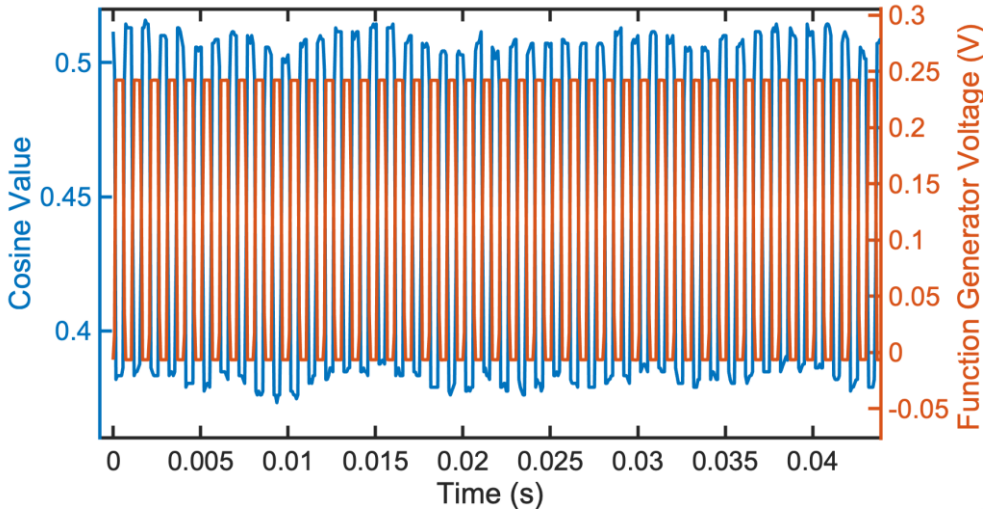

Figure 3.6: An example of $\cos(\phi + \theta)$ value modulated by a square wave driven phase modulator.

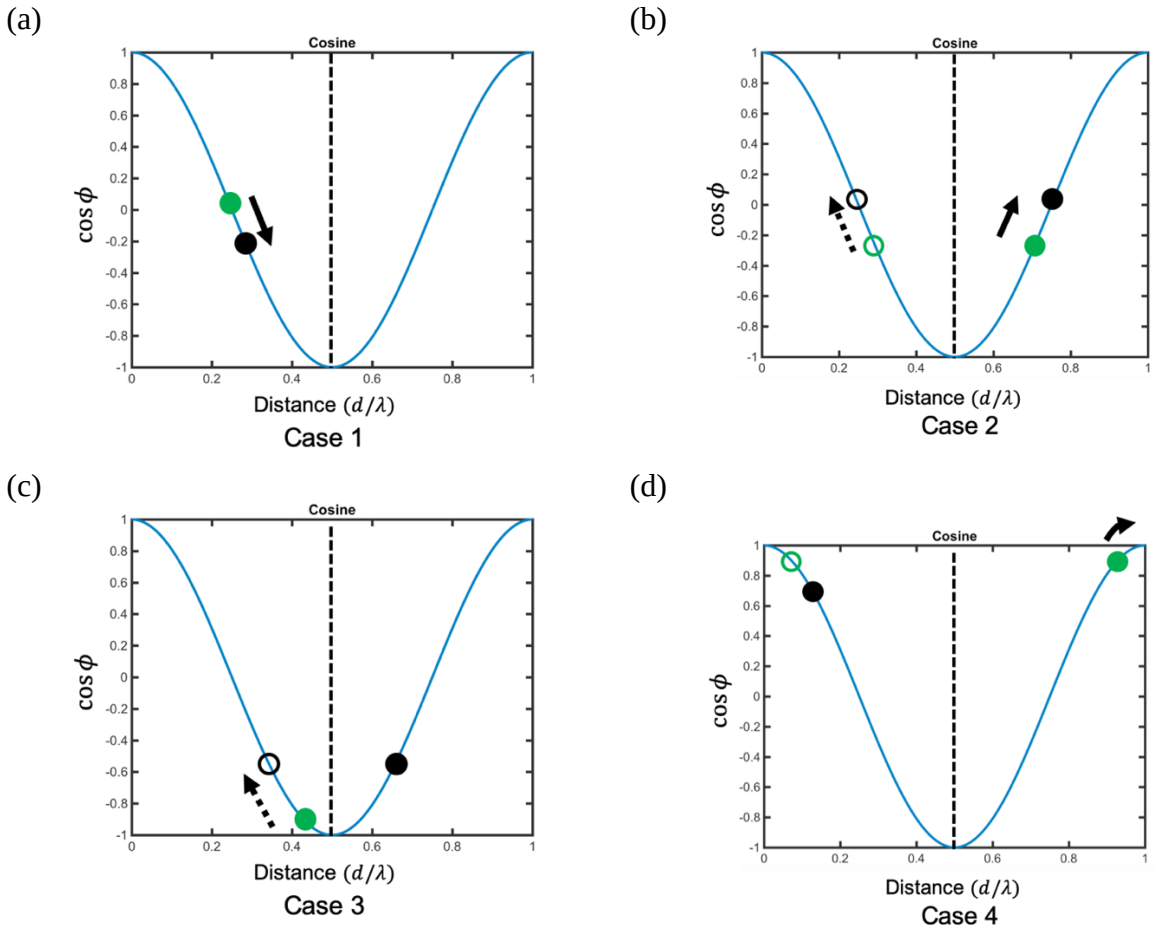

Figure 3.7: The four possible outcomes of applying a small phase shift to the interferometric signal. Filled circles indicate the positions based on unwrapped phase, and the hollow circles indicate the positions on ambiguous cosine.

Utilizing the algorithm discussed in the previous paragraph and illustrated in Fig. 3.7, we can unwrap the interferometric phase of the cosine signal shown in Fig. 3.8. A comparison of the wrapper and unwrapped phases is added in Fig. 3.9.

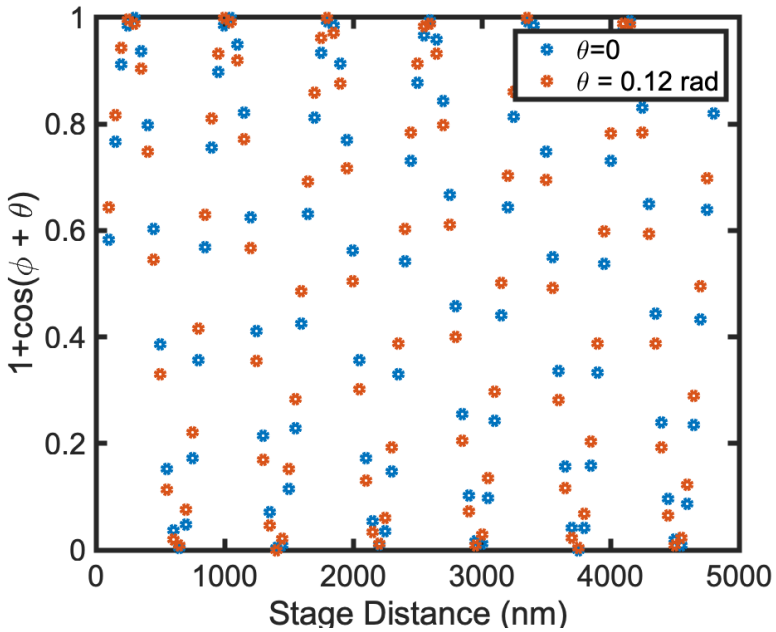

Figure 3.8: Cosine and the phase shifted cosine

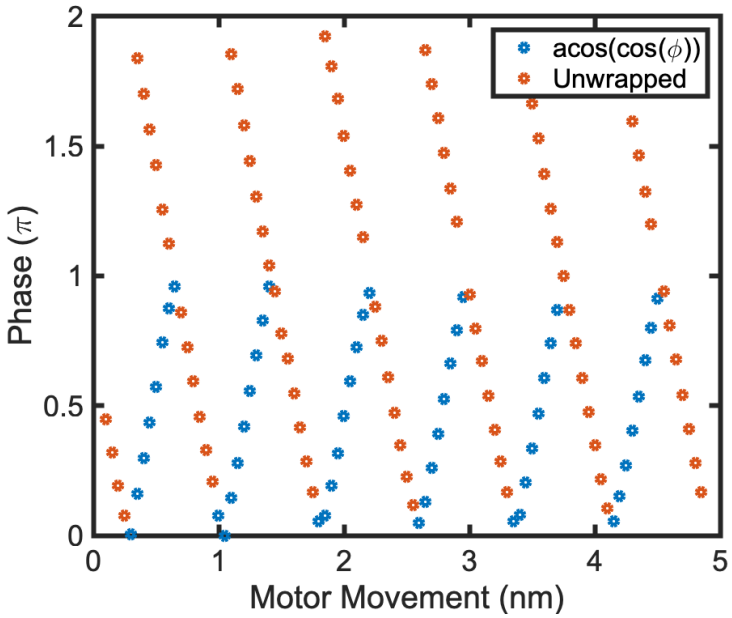

Figure 3.9: Wrapped and unwrapped phase as function of the motor movement.

An alternative to a single phase shifting system discussed above is the technique involving multiple phase shifts. The concepts of phase shifting interferometry [47]–[49] can be used to extract phase from the detected interferometric currents. These phase shifts may be induced in time through a piezo-motor controlled reference arm, or simultaneously with the use of polarization optics, and mathematically expresses itself as follows:

$$I(\alpha) = I_R + I_s + 2\sqrt{I_R I_s}\cos(\phi + \alpha) \tag{3.30}$$

Where α is the induced phase shift. A minimum of three phase shifts is required for this technique [50] and is commonly referred to as the three-bucket method. The three phase shifts are:

$$\begin{aligned} I_1 = I\left(\frac{\pi}{4}\right) &= I_R + I_s + \sqrt{2}\sqrt{I_R I_s}[\cos(\phi) - \sin(\phi)] \\ I_2 = I\left(\frac{3\pi}{4}\right) &= I_R + I_s + \sqrt{2}\sqrt{I_R I_s}[-\cos(\phi) - \sin(\phi)] \\ I_3 = I\left(\frac{5\pi}{4}\right) &= I_R + I_s + \sqrt{2}\sqrt{I_R I_s}[-\cos(\phi) + \sin(\phi)] \end{aligned} \tag{3.31}$$

To extract the phase, we can utilize the following equation:

$$\phi = atan2\left(\frac{I_3 - I_2}{I_1 - I_2}\right) \tag{3.32}$$

Alternatively, a more noise-tolerant configuration is the four-bucket solution [51] that requires four phase shifts.

$$\begin{aligned} I_1 = I(0) &= I_R + I_s + 2\sqrt{I_R I_s}\cos(\phi) \\ I_2 = I(\pi/2) &= I_R + I_s + 2\sqrt{I_R I_s}\cos\left(\phi + \frac{\pi}{2}\right) = I_R + I_s - 2\sqrt{I_R I_s}\sin(\phi) \\ I_3 = I(\pi) &= I_R + I_s + 2\sqrt{I_R I_s}\cos(\phi + \pi) = I_R + I_s - 2\sqrt{I_R I_s}\cos(\phi) \\ I_4 = I\left(\frac{3\pi}{2}\right) &= I_R + I_s + 2\sqrt{I_R I_s}\cos\left(\phi + \frac{3\pi}{2}\right) = I_R + I_s + 2\sqrt{I_R I_s}\sin(\phi) \end{aligned} \tag{3.33}$$

And the interferometric phase can be extracted with the following operations:

$$\phi = atan2\left(\frac{I_1 - I_3}{I_4 - I_2}\right) \tag{3.34}$$

In chapter 5, we will return to how we use geometric optics to induce phase-shifted I_1 and I_2 from Eq. 3.33 to extract the phase. Furthermore, we discuss how all four phase shifted signals can be induced in a compact setup.

Chapter 4: Arithmetic formulation of De-Multiplexed Multiwavelength Interferometry

As explained in the previous chapter, the fundamental limitation of a single wavelength interferometer is the range that is limited to one λ due to the phase wrapping around 2π. Interferometry with multiple wavelengths, or multiwavelength interferometry, can be used to extend this unambiguous range, however, the exact range and accuracy are dependent on how the system is configured.

In this chapter, we first explore different multiwavelength techniques in literature and their drawbacks. We then present an analytical formulation that is algebraic, noise-tolerant, and efficient. We then comprehensively analyze how our mathematical formulation responds to noise and define the noise bounds for error-free unwrapping of distance.

4.1 Beat-Wavelength Techniques

Perhaps the most common instantiation of multiwavelength solutions is the beat-wavelength approach [52], and is also called the synthetic wavelength technique. Interferometry is simultaneously performed with multiple wavelengths and the interferometric signal is detected on a single photodetector, as depicted in Fig. 4.1. The interference signal can be expressed as:

$$I = I_{\mathrm{r}} + I_{\mathrm{s}} + 2\sqrt{\mathrm{I_S I_r}}\begin{bmatrix} \cos\big((\omega_1-\omega_2)t\big) + 2\cos(k_1 d) + \\ 2\cos\big((\omega_1-\omega_2)t - k_2 d\big) + 2\cos\big((\omega_1-\omega_2)t + k_1 d\big) + \\ 2\cos(k_2 d) + \mathbf{2\cos\big((\omega_1-\omega_2)t + (k_1-k_2)d\big)} \end{bmatrix} \tag{4.1}$$

Where I_r and I_s are the reference and sample powers. ω_1 and k_1 are the frequency and wavevector of the first wavelength, and similarly, ω_2 and k_2 are the frequency and wavevector of the second wavelength. And d denotes the path length difference between the two arms. The most interesting term in Eq. 4.1 is bold faced, and enables a longer range equal to the beat wavelength:

$$\lambda_b = \frac{2\pi}{k_1 - k_2} = \frac{\lambda_1\lambda_2}{|\lambda_1 - \lambda_2|} \tag{4.2}$$

However, while the range is extended, the accuracy suffers by a factor of λ/λ_b since it is inversely proportional to $\Delta k = k_1 - k_2$.

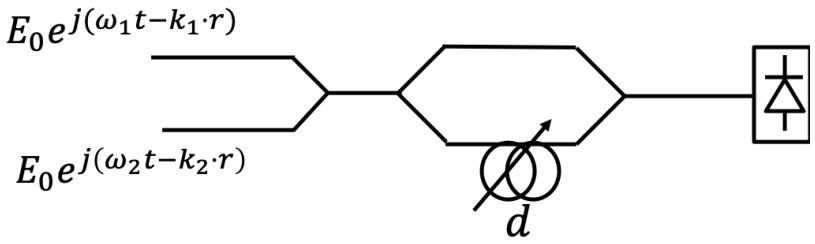

Figure 4.1: A typically configuration for a beat-wavelength based system. Interferometry is performed with multiple wavelengths but the interferometric signal is detected on a single photodetector.

4.2 De-multiplexed Multiwavelength Techniques

To alleviate this range-accuracy trade-off, prior to the detection of the interference signal, the wavelength interferograms have to be de-multiplexed. This configuration is illustrated in Fig. 4.2 (a). The accuracy of such a system is the same as that of a single-wavelength interferometer discussed in the previous chapter. The theoretical limit for the range is the lowest-common-multiple, lcm, of all the wavelengths used in the system.

(a)

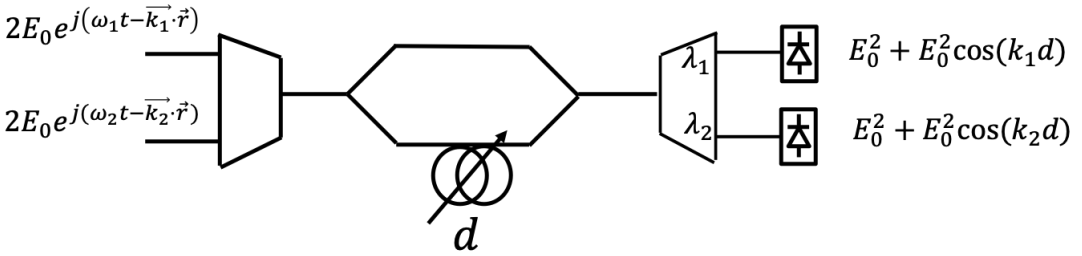

(b)

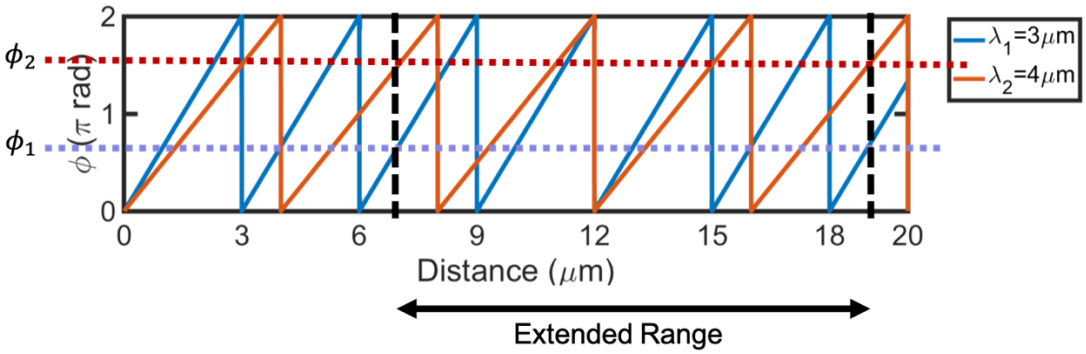

Figure 4.2: a) Configuration of a demultiplexed multiwavelength interferometry system. b) Illustration of the extended range with wavelengths 3 µm and 4 µm

Intuitively, the measurement range is extended by separately detecting the interferometric phases ϕ_i from measurement performed with each wavelength λ_i, and analyzing the combination of all the phase values. Fig 4.2 (b) shows an illustration of this concept with wavelengths $\lambda_1 = 3\ \mu$m and $\lambda_2 = 4\ \mu$m. The distance ambiguity fundamentally stems from the 2π ambiguity of phase. Two particular phases ϕ_{1_0} and ϕ_{2_0} are measured at a particular measurement distance d_0. The next distance at which $\phi_1 = \phi_{1_0}$ and $\phi_2 = \phi_{2_0}$ occurs at $d_0 + \text{lcm}(\lambda_1, \lambda_2)$, which in this case is 12 μm.

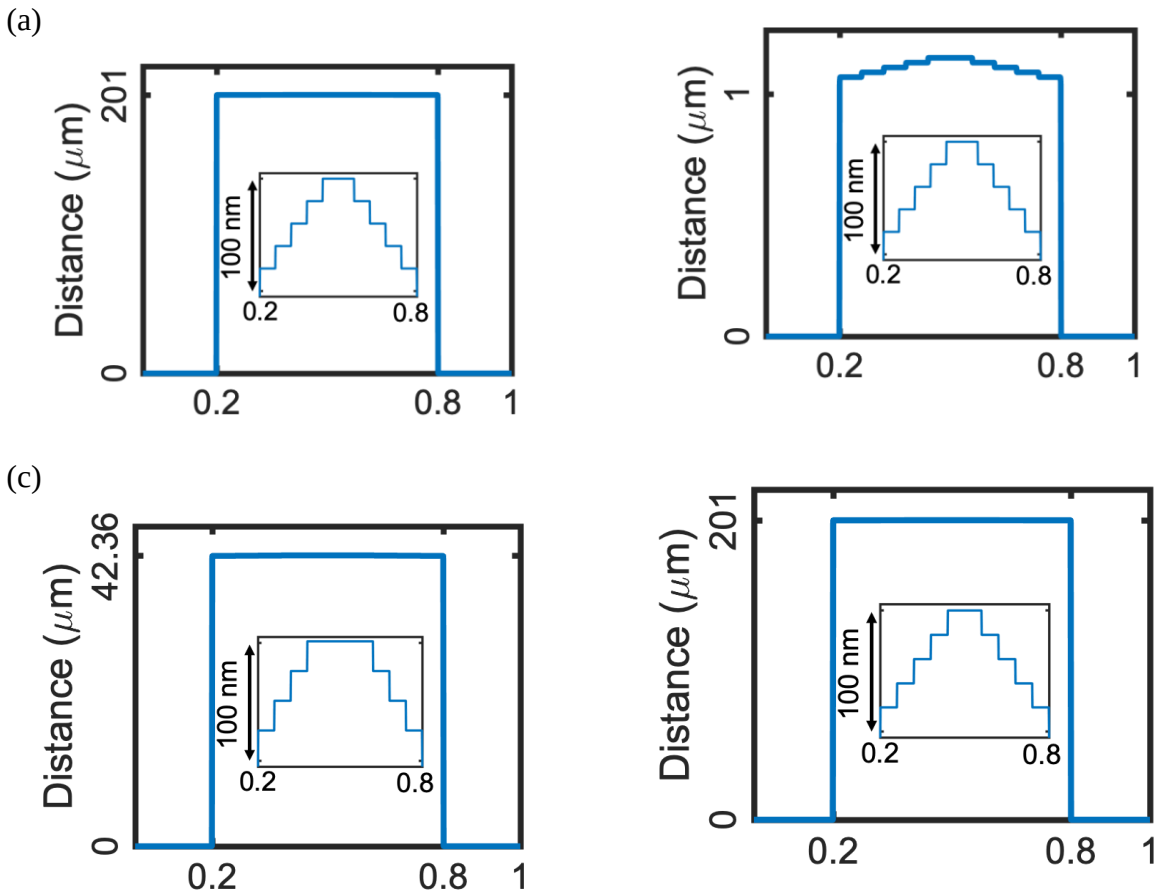

Figure 4.3: Simulations of how a sample (depicted in (a)) with both large and fine features on top is measured with (b) single wavelength interferometer, (b) Beat-wavelength technique, and (c) Demultiplexed wavelength technique. λ_1 and λ_2 are assumed to be 1535 nm and 1550 nm. $3\sigma_\phi$ is taken to be 0.005 for all three simulations.

To highlight the differences between beat-wavelength and demultiplexed-wavelength interferometry, we ran simulations on a how a particular target would be measured by these techniques. Fig. 4.3 (b), (c) and (d) shows simulated results of how the target in Fig. 4.3 (a) is measured with single-wavelength, beat-wavelength and demultiplexed-wavelength interferometry techniques respectively. Single-wavelength interferometry correctly interprets the finer features but misrepresents the height of 201 μm due to its limited range of 1.55 μm. Synthetic-wavelength technique, utilizing wavelengths 1535 nm and 1550 nm, has a range of

158.62 μm, and a resolution which is 102x worse, and thus the technique incorrectly extracts the large height and more importantly, the smaller features in the plateau region of the simulated target. Wavelength-demultiplexed interferometry, with the range of the lcm, 307 μm, is the only technique that correctly extracts both the large height and the smaller features. The simulation for demultiplexed-wavelength interferometry was run using the algorithm discussed in Section 4.4.

4.3 De-multiplexed Techniques

Over the years, a few algorithms have been developed to extract the unambiguous distance from a multiwavelength interferometer, however, these algorithms have drawbacks. The first set of algorithms converges onto the fringe order with the smallest mean square error. This includes the Excess Fractions (EF) [53]–[56] technique which is computationally expensive because of the inherent need to perform an exhaustive search, and techniques that use look-up tables [57]–[59] that additionally significantly burden the memory resources and necessitate a serial search. These issues become more serious as the measurement range increases.

A second set of algorithms aims to algebraically calculate the fringe order and is thus computationally efficient. Among them is the Chinese Remainder Theorem (CRT) based approach [60] which gives an explicit expression for the unwrapped distance utilizing number theory. It works with coprime wavelengths and has a theoretical range of the lcm but is impractical to implement as it is inaccurate in the presence of noise. The noise sensitivity of the CRT approach is discussed in more detail at the end of Section 4.5. Supplementary techniques to make the CRT noise tolerant, using lookup tables [61] or iterative algorithms [62]–[64], significantly increase the computational complexity of the solution. Alternatively, beat-wavelength inspired formulations approach the theoretical maximum for noise tolerance, limited by fundamental statistics, but have a limited range of the beat-wavelength. This beat-wavelength range can be enhanced through the De Groot formulation [65], but still falls shy of the lcm for many choices of wavelengths. Additionally, these techniques are prone to error in the wavelength configuration for which the range approaches, but does not reach, the limit of lcm. Furthermore, adding multiple wavelengths in such formulations has also been explored [66], but the range is largely determined by the largest beat-wavelength, therefore necessitating the generation and demultiplexing of two closely spaced wavelengths.

In this chapter, we present a new arithmetic algorithm for multiwavelength interferometer that has a theoretical maximum range of the lcm, the resolution of a single-wavelength interferometer, and achieves the theoretical maximum noise tolerance of an algebraic approach.

4.4 Mathematical Derivation

In this section we derive the analytical formulation to extend the unambiguous range with two wavelengths. In section 4.6, we will build upon this formulation to show how it can be extended to multiple wavelengths.

Fundamentally, the measures phases ϕ_1 and ϕ_2, are a function of the path length distance d through the following formulation:

$$\phi_1 = k_1 d \bmod 2\pi \tag{4.3}$$

$$\phi_2 = k_2 d \bmod 2\pi \tag{4.4}$$

Where k_1 and k_2 are the wavevectors for the first and second wavelength respectively. Re-arranging terms in Eq. 4.3 and Eq. 4.4, we arrive at:

$$k_1 d = \phi_1 + m(2\pi) \tag{4.5}$$

$$k_2 d = \phi_2 + n(2\pi) \tag{4.6}$$

Where m and n are the fringe numbers of the interferometric phase for λ_1 and λ_2 respectively. Fig. 4.3 shows how these fringe numbers vary over the extended unambiguous range for a system with wavelengths $\lambda_1 = 3\ \mu m$ and $\lambda_2 = 4\ \mu m$. Generally, for most situations, the m and n are unknown. Setting m and n in Eq. 4.5 and Eq 4.6 to zero results in an unambiguous range equal to the wavelengths λ_1 and λ_2, respectively. If a steadily changing surface, such as a lens or a mirror, is being measured, the m and n can simply be determined by counting the fringes. However, for a more practical application, such as measuring an etch depth, this is not possible. The use of multiple wavelengths enables the determination of these fringe numbers, and thus the extension of the unambiguous range.

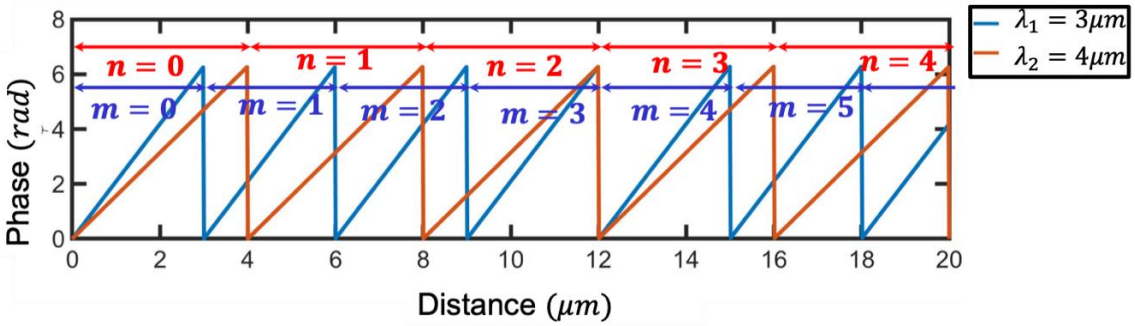

Figure 4.4: Interferometric phase vs Distance plot for two wavelengths of $\lambda_1 = 3\ \mu m$ and $\lambda_2 = 4\ \mu m$. The plot also shows the fringe numbers m and n for the phase from λ_1 and λ_2 respectively.

Since the same path length difference is measured through the phases ϕ_1 and ϕ_2, we combine Eq. 4.5 and Eq. 4.6 to write the path length difference d as:

$$d = \frac{\phi_1}{2\pi}\lambda_1 + m\lambda_1 = \frac{\phi_2}{2\pi} + n\lambda_2 \tag{4.7}$$

We then define a new variable L, that is then solved for m and n, as:

$$L = m\lambda_1 - n\lambda_2 \tag{4.8}$$

Rearranging the terms of Eq. 4.7, we can write L as a function of the measured phases:

$$L = \frac{\phi_2}{2\pi} - \frac{\phi_1}{2\pi} \tag{4.9}$$

Since Eq. 4.8 is a non-homogeneous equation, the solution for m comprises of a particular solution, m_0, to Eq 4.8, and a solution, m_h, to the homogeneous equation. Therefore, m can be expressed as:

$$m = m_0 + \zeta m_h, \tag{4.10}$$

Where $\zeta \subseteq \mathbb{N}$. ζ is similar to m in Eq. 4.5 but cannot be determined in a two-wavelength configuration. It thus defines the maximum value of m that can be determined. Alternatively, m can be written as:

$$m = m_0 \bmod m_h \tag{4.11}$$

We first solve for m_0 and then solve m_h. To find a particular solution to *m*, we assume that λ_1 and λ_2 are integers and utilize Bezout's identity which states that for any two integers *x* and *y*, with greatest common divisor $\gcd(x, y)$, there are unique coefficients a and b such that:

$$ax + by = \gcd(x, y) \tag{4.12}$$

These coefficients can be evaluated using many algorithms, including the Extended Euclidean Algorithm. Utilizing the Bezout's identity, we write a similar equation for our integer wavelengths λ_1 and λ_2:

$$\mu\lambda_1 + \nu\lambda_2 = \gcd(\lambda_1, \lambda_2) \tag{4.13}$$

Multiplying both sides of Eq. 4.13 with $L/\gcd(\lambda_1, \lambda_2)$ yields:

$$\frac{L}{\gcd(\lambda_1, \lambda_2)}[\mu\lambda_1 + \nu\lambda_2] = L \tag{4.14}$$

Comparing the coefficients of λ_1 and λ_2 is Eq. 4.14 and Eq. 4.8, we arrive at particular solutions, m_0 and n_0, for m and n respectively:

$$m_0 = \frac{\mu L}{\gcd(\lambda_1, \lambda_2)} \tag{4.15}$$

$$n_0 = \frac{\nu L}{\gcd(\lambda_1, \lambda_2)} \tag{4.16}$$

Next, to completely solve for m and n, we solve the homogeneous case of Eq. 4.8:

$$m_h\lambda_1 - n_h\lambda_2 = 0 \tag{4.17}$$

The smallest solution for which Eq. 4.17 is true is when:

$$m_h = \frac{\lambda_2}{\gcd(\lambda_1, \lambda_2)} \tag{4.18}$$

$$n_h = \frac{\lambda_1}{\gcd(\lambda_1, \lambda_2)} \tag{4.19}$$

Plugging the particular solution and the non-homogeneous solution in Eq. 4.10, we arrive at:

$$m = \frac{\mu L}{\gcd(\lambda_1, \lambda_2)} + \zeta \left[\frac{\lambda_2}{\gcd(\lambda_1, \lambda_2)}\right] \tag{4.20}$$

And similarly, for n,

$$n = \frac{\nu L}{\gcd(\lambda_1, \lambda_2)} + \zeta \left[\frac{\lambda_1}{\gcd(\lambda_1, \lambda_2)}\right] \tag{4.21}$$

While we have solved for m and n, the objective is to find an expression for d as a function of the measured phases, ϕ_1 and ϕ_2. To this end, we first plug in the expression for L from Eq. 4.9 into Eq. 4.20.

$$m = \frac{\mu}{2\pi} \frac{(\phi_2 \lambda_2 - \phi_1 \lambda_1)}{\gcd(\lambda_1, \lambda_2)} + \zeta \left[\frac{\lambda_2}{\gcd(\lambda_1, \lambda_2)}\right] \tag{4.22}$$

Plugging this expression back into Eq. 4.7, we arrive for an algebraic formulation for d:

$$d(\phi_1, \phi_2) = \frac{\phi_1}{2\pi}\lambda_1 + \lambda_1 \frac{\mu}{2\pi} \frac{(\phi_2 \lambda_2 - \phi_1 \lambda_1)}{\gcd(\lambda_1, \lambda_2)} + \zeta \left[\frac{\lambda_1 \lambda_2}{\gcd(\lambda_1, \lambda_2)}\right] \tag{4.23}$$

The last term $\lambda_1 \lambda_2 / \gcd(\lambda_1, \lambda_2)$ is the definition of the lowest-common-multiple (lcm) of λ_1 and λ_2. Since ζ cannot be solved, the last term also defines the extended unambiguous range, and d can thus be written as:

$$d(\phi_1, \phi_2) = \left[\frac{\phi_1}{2\pi}\lambda_1 + \lambda_1 \frac{\mu}{2\pi} \frac{(\phi_2 \lambda_2 - \phi_1 \lambda_1)}{\gcd(\lambda_1, \lambda_2)}\right] \bmod [\mathrm{lcm}(\lambda_1, \lambda_2)] \tag{4.24}$$

The expression in Eq. 4.24 clearly shows that it is just a function of the measured phases ϕ_1 and ϕ_2, and has a range of the lowest-common-multiple (lcm). μ and $\gcd(\lambda_1, \lambda_2)$ are pre-calculated for the choices of $\lambda_1$and λ_2 because they do not depend on the measured phases, and thus do not add computational complexity. Furthermore, our formulation, summarized in Eq 4.24, is computationally efficient because it is simply algebraic.

Eq. 4.24 is written with λ_1 and μ, but it can also be expressed with λ_2 and ν using the same steps discussed above.

$$d(\phi_1, \phi_2) = \left[\frac{\phi_2}{2\pi}\lambda_2 + \lambda_2 \frac{\nu}{2\pi}\frac{(\phi_2\lambda_2 - \phi_1\lambda_1)}{\gcd(\lambda_1, \lambda_2)}\right] \bmod [\mathrm{lcm}(\lambda_1, \lambda_2)] \quad (4.25)$$

Eq. 4.24 and Eq. 4.25 are redundant but show that the range can be extended by solving for either m or n. The accuracy, however, has a preferred wavelength, and is better with the shorter of the two wavelengths. Examples of the values for μ and ν for different wavelength combinations are given in the following table:

λ_1	λ_2	$\gcd(\lambda_1, \lambda_2)$	μ	ν
1549	1550	1	-1	1
1535	1550	5	103	-102
1540	1550	10	-1	1
1525	1550	25	-1	1

Table 4.1: Values of gcd, μ and ν for different combinations of wavelengths λ_1 and λ_2

A requirement in our system is that the wavelengths are integers. This can be satisfied by changing the units to calculate in integer field. For instance, if the wavelengths are 1550 nm and 1551 nm, the unit can be chosen to be nanometers such that the wavelengths are integers. Similarly, if the wavelengths are 1550.1 nm and 1550.2 nm, the unit can be chosen to be 0.1 nm such that the integer wavelengths are 15501 and 15502. Even with similar gcd, larger numbers have a large lcm, and thus range, but these wavelengths cannot be chosen arbitrarily. Rather, the choice is determined by the noise in phase measurements and is explained in the next section.

4.5 Noise tolerance analysis

One of the key features of our formulation is that not only is it algebraic, but unlike the Chinese-Remainder-Theorem based approaches, it is also noise-tolerant. Noise is inherent in any measurement and designing an algorithm that can tolerate a certain degree of noise, and still operate accurately, is a key requirement for a practical system.

The interferometric current signals, detected on photodetectors, are used to calculate and extract the interferometric phase. Noise in these current measurements results in an uncertainty in the calculated interferometric phase. The relation between the uncertainty in phases and noise in currents, depends on the measurement setup, and will be derived in the next chapter when we discuss our measurement setup. How this uncertainty impacts the calculated fringe number, however, depends on the technique used to extend the unambiguous range. In our formulation, we treat photodetector currents and interferometric phases as normal distributions with a standard deviation σ.

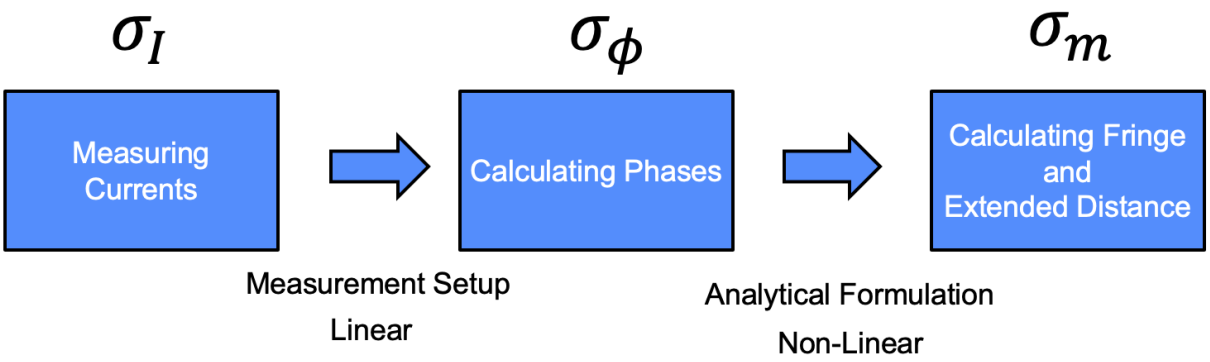

Figure 4.5: An illustration of how noise in measurement current propagates in the system. How this noise impacts the calculated phases depends on the measurement setup. However, how the uncertainty in measured phases impacts the fringe calculation solely depends on the mathematical formulation.

To understand how our mathematical formulation reacts to uncertainty in noise measurements, the standard deviation σ_ϕ, we look at the particular solution of m, m_0, expressed in Eq. 4.15. Since m, n, λ_1 and λ_2 are all integers, L is also an integer. Furthermore, since λ_1 and λ_2 are related by the gcd, the quantity L/gcd is an integer and increases monotonically. We define a new parameter γ, and set it equal to L/gcd, such that, by definition:

$$\gamma(\phi_1, \phi_2) = \frac{L}{\text{gcd}(\lambda_1, \lambda_2)} = \frac{\phi_2\lambda_2 - \phi_1\lambda_1}{\text{gcd}(\lambda_1, \lambda_2)} \tag{4.26}$$

Since γ is a function of ϕ_2 and ϕ_1, uncertainty in these phases, σ_ϕ, causes uncertainty in γ, and γ deviates from an integer value. The standard deviation of γ, σ_γ, can be expressed using the principles of error propagation:

$$\sigma_\gamma^2 = \left(\frac{\delta\gamma}{\delta_{\phi_1}}\right)^2 \sigma_{\phi_1}^2 + \left(\frac{\delta\gamma}{\delta_{\phi_2}}\right)^2 \sigma_{\phi_2}^2 \tag{4.27}$$

Since both phases are calculated similarly, their uncertainty is also expected to be similar, and thus we assume:

$$\sigma_{\phi_1} = \sigma_{\phi_2} = \sigma_\phi \tag{4.28}$$

And use Eq. 4.28 to simplify Eq. 4.27 to get:

$$\sigma_\gamma^2 = \left[\left(\frac{\delta\gamma}{\delta_{\phi_1}}\right)^2 + \left(\frac{\delta\gamma}{\delta_{\phi_2}}\right)^2\right] \sigma_\phi^2 \tag{4.29}$$

Solving the partial derivatives, and taking the square root of the variance, we find the standard deviation of γ, σ_γ:

$$\sigma_\gamma = \sqrt{\left(\frac{\lambda_1}{2\pi\,\gcd(\lambda_1,\lambda_2)}\right)^2 + \left(\frac{\lambda_2}{2\pi\,\gcd(\lambda_1,\lambda_2)}\right)^2}\,\sigma_\phi \tag{4.30}$$

Since γ is expected to be an integer, we can round it to the nearest integer. However, the rounding operation will cause errors if the γ value deviates by more than 0.5. Thus, assuming a normal distribution of γ with a σ_γ standard deviation, for a 99.7% accuracy, we want the $3\sigma_\gamma$ value to be less than 0.5.

$$3\sigma_\gamma < 0.5 \tag{4.31}$$

Plugging in the condition of Eq. 4.31 into Eq. 4.30:

$$6\sigma_\phi\sqrt{\left(\frac{\lambda_1}{2\pi\,\gcd(\lambda_1,\lambda_2)}\right)^2 + \left(\frac{\lambda_2}{2\pi\,\gcd(\lambda_1,\lambda_2)}\right)^2} < 1 \tag{4.32}$$

Simplifying the expression, we arrive at:

$$\frac{6\sigma_\phi}{2\pi\,\gcd(\lambda_1,\lambda_2)}\sqrt{\lambda_1^2+\lambda_2^2} < 1 \tag{4.33}$$

To find the tolerance to uncertainty in phase, we make σ_ϕ the subject,

$$3\sigma_\phi < \pi\ \frac{\gcd(\lambda_1,\lambda_2)}{\sqrt{\lambda_1^2+\lambda_2^2}} \tag{4.34}$$

An expression similar to Eq. 4.34 can be found in approaches inspired by the beat-wavelength, where gcd is replaced by the difference of wavelengths [67], however that expression is invalid unless the beat-wavelength is much smaller than the lcm. Since the order of magnitude of λ_1 and λ_2 are the same, and much different from the magnitude of $\gcd(\lambda_1,\lambda_2)$, we assume $\lambda_1 \approx \lambda_2 = \lambda$ and simplify Eq. 4.34 to:

$$3\sigma_\phi < \pi\ \frac{\gcd(\lambda_1,\lambda_2)}{\sqrt{2}\lambda} = \frac{\pi\lambda}{\sqrt{2}\,\mathrm{lcm}(\lambda_1,\lambda_2)} \tag{4.35}$$

As deducted from Eq. 4.25, for a dual-wavelength system, the $\mathrm{lcm}(\lambda_1,\lambda_2)$ signifies the unambiguous range of the system. Thus rearranging Eq. 4.35 to make the range, $\mathrm{lcm}(\lambda_1,\lambda_2)$, the subject of the formulation, we obtain:

$$\mathrm{lcm}(\lambda_1,\lambda_2) < \frac{\pi\lambda}{3\sqrt{2}\,\sigma_\phi} \tag{4.36}$$

As evident from Eq. 4.36, the range for a dual-wavelength system is inversely related to the uncertainty in phase measurements. The smaller the uncertainty is, the larger the range can be. This stems from the fact that a system with a small uncertainty in phase measurements can afford to use wavelengths with a small gcd. From the definition of the lcm, a smaller gcd results in a larger lcm, and thus a longer range.

If the uncertainty in phase exceed the bounds established in Eq. 4.35, the extended distance is evaluated incorrectly because of an incorrect fringe number, m, calculation. Although the uncertainty causes γ, in Eq. 4.26, to be rounded to the next integer, m can deviate by more than an integer because it is multiplied by μ in Eq. 4.13.Values of μ can be, but is most usually, not 1, and thus the large deviation of m causes a huge change in the extended distance and cannot be averaged out. Values of μ for different combinations of wavelengths around 1550 nm are given in Table 4.1. Therefore, it is essential to ensure that the interferometric system is configured such that Eq. 4.34 is always satisfied.

More fundamentally, the noise in phase measurements, σ_ϕ, sets a requirement on the choice of wavelengths λ_1 and λ_2, such that their greatest-common-divisor satisfies Eq. 4.34. For a fixed σ_ϕ, since the dual-wavelength range has a theoretical upper limit, a way to extend the range beyond that in Eq. 4.36 is to transition to a multiwavelength system.

The closest algorithm to our work is the Chinese Remainder Theorem (CRT), as it is also algebraic and has a range of the lcm. However, the CRT is not tolerant to noise and thus unreliable. A detailed comparison of our technique with the CRT is added here for clarity. The CRT-based solution to this problem, first proposed by Gushov & Solodkin [60], has been widely adopted [68]–[70]. This approach enables the direct calculation of the unwrapped distance through the equation: $d_u = \left(\sum_{i=1}^{k} \gamma_i \gamma_i' d_i'\right) mod \prod_{j=1}^{k} \lambda_j'$, where $\gamma_i = \frac{1}{\lambda_i}\prod_{j=1}^{k} \lambda_j'$, and γ_i' is the inverse of γ_i modulo λ_i' and can be calculated from the Extended Euclidean Algorithm, and $d_i' = \lambda_i' \phi_i/(2\pi)$. A major limitation of the original CRT method is that it works correctly only in the absence of any deviation from the expected phase values, ϕ_i.

Unlike our algorithm which rounds the quantity that is expected to be an integer, $L/\gcd(\lambda_1, \lambda_2) = (\mathrm{d}_1 - d_2)/\gcd(\lambda_1, \lambda_2)$, to the nearest integer, in CRT methods $d_1/\gcd(\lambda_1, \lambda_2)$ and $d_2/\gcd(\lambda_1, \lambda_2)$ are rounded independently. Since neither $d_1/\gcd(\lambda_1, \lambda_2)$ nor $d_2/\gcd(\lambda_1, \lambda_2)$ is expected to be an integer, rounding these results in artifacts in the presence of noise.

Any deviation in phases, due to measurement noise or slight inaccuracies in the wavelength settings, results in an incorrect unwrapped distance that is off by a factor of $\gamma\gamma'$at arbitrary measured positions. To convey the severity of the issue, we analyze the impact of a deviation of $\delta\phi_1$ in one of the phases measured, ϕ_1. This deviation will result in an incorrect unwrapped distance for a length of $\lambda_1\delta\phi_1/2\pi$ after every length of (gcd $-\frac{\lambda_1\delta\phi_1}{2\pi}$). The proportion of incorrectly unwrapped distance is $\frac{\lambda_1\delta\phi_1}{2\pi}$/gcd. For $\delta\phi_1 = 2\pi/1325$ and gcd=25, about 4.6% of the measured distances will be unwrapped incorrectly. Furthermore, the errors due to the

deviation of expected interferometric phase values at other wavelengths compound, thus exacerbating the problem. Extended-CRT techniques that can tolerate noise are not algebraic, and thus do so at the expense of computational efficiency.

4.6 Multiwavelength System

Just as the use of two wavelength enables an extended unambiguous range, adding more wavelengths, and analyzing the interferometric phases from all wavelengths, results in an even longer unambiguous range. The challenge however it to formulate multiwavelength phase unwrapping in a way that is not only computationally inexpensive and noise tolerant, but also one in which the noise tolerance does not become worse with increasing number of wavelengths. Our analytical formulation achieves all this.

The multiwavelength formulation is simply an extension of our two-wavelength system. We decompose the multiwavelength problem into many two "wavelength" cases, and solve the multiwavelength problem, recursively. In this section, we begin by rewriting the two-wavelength formulation, extend it to a three-wavelength case, and then generalize it to an N-wavelength case. For this analysis, it is more intuitive to formulate it with measured ambiguous distances, instead of phases. Analogous to Eq. 4.4 and Eq. 4.4:

$$d_i = d \bmod \lambda_i \tag{4.37}$$

Where $d_i = \phi_i \lambda_i/(2\pi)$ is the ambiguous distance measured from the interferometer using the wavelength λ_i. Fundamentally, the ambiguity stems from the 2π ambiguity of the measured phase. While it is always the phase that is measured, here we convert it to a distance using the formulation discussed in Chapter 2. Rephrasing Eq. 4.24 with ambiguous distances d_1 and d_2, we get:

$$d_{u,2}(d_1, d_2) = \left[d_1 + \mu\lambda_1 \left[\frac{d_2 - d_1}{\gcd(\lambda_1, \lambda_2)} \right]_{NINT} \right] \bmod [\mathrm{lcm}(\lambda_1, \lambda_2)] \tag{4.38}$$

Where $d_{u,2}$ is the distance extended with two wavelengths, $d_1 = \phi_1 \lambda_1/(2\pi)$, and $d_2 = \phi_2 \lambda_2/(2\pi)$.

For a three-wavelength system, an unambiguous distance $d_{u,2}$ can first be obtained up to a range of $\mathrm{lcm}(\lambda_1, \lambda_2)$ using wavelengths λ_1 and λ_2. Using $d_{u,2}$ and λ_3, the unambiguous distance can further be extended to $d_{u,3}$ with a range of $\mathrm{lcm}(d_{u,2}, \lambda_3)$. The formulation can be expressed as:

$$d_{u,3}(d_{u,2}, d_3) = \left[d_{u,2} + \mu_3 \lambda_{e,2} \left[\frac{d_3 - d_{u,2}}{\gcd(\lambda_1, d_{u,2})} \right]_{NINT} \right] \bmod \left[\mathrm{lcm}(\lambda_1, \lambda_{e,2}) \right] \tag{4.39}$$

Where μ_3 is obtained by solving the following equation using the Extended Euclidean Algorithm:

$$\mu_3\lambda_{e,2} + \nu_3\lambda_3 = \gcd(\lambda_{e,2}, \lambda_3) \tag{4.40}$$

Where $\lambda_{e,2} = \text{lcm}(\lambda_1, \lambda_2)$. The range for a three-wavelength system, expressed as $\text{lcm}\big(\lambda_1, \lambda_{e,2}\big)$ in Eq. 4.39, can be simplified by using the expression for $\lambda_{e,2}$ to obtain:

$$\text{lcm}\big(\lambda_3, (\lambda_1, \lambda_2)\big) = \text{lcm}(\lambda_1, \lambda_2, \lambda_3) \tag{4.41}$$

Thus, the range, in our formulation, is indeed the theoretical maximum range of the lowest-common-multiple of the three wavelengths used in the system. From Eq. 4.34, we know that the noise tolerance only primarily depends on the greatest common divisor, and thus the noise-tolerance for a three-wavelength system is not any worse than the two-wavelength system if the following relation holds true:

$$\gcd\big(\lambda_{e,2}, \lambda_3\big) \geq \gcd(\lambda_1, \lambda_2) > \frac{\sqrt{2}\lambda}{\pi} 3\sigma_\phi \tag{4.42}$$

The order and values of λ_1, λ_2 and λ_3 have to be chosen such that they satisfy Eq 4.42. Where λ is approximately the mean value of the three wavelengths.

This three-wavelength formulation can be extended to N-wavelengths. Similar to the two and three-wavelength expressions, the final expression for the unwrapped distance with N wavelengths is as follows:

$$d_{u,N}\left(d_{u,N-1}, d_N\right) = \left[d_{u,N-1} + \mu_N\lambda_{e,N-1}\left[\frac{d_N - d_{u,N-1}}{\gcd\big(\lambda_N, \lambda_{e,N-1}\big)}\right]_{NINT}\right] \text{mod}\left[\text{lcm}\big(\lambda_N, \lambda_{e,N-1}\big)\right] \tag{4.43}$$

Where μ_N is found by solving the following equation using the Extended Euclidean algorithm:

$$\mu_N\lambda_{e,N-1} + \nu_N\lambda_N = \gcd(\lambda_N, \lambda_{e,N-1}) \tag{4.44}$$

Where $\lambda_{e,N-1} = \text{lcm}(\lambda_1, \lambda_2, \cdots, \lambda_{N-1})$, and $d_{u,N-1}$ is found by recursively solving Eq 4.43 for N-1 wavelengths. This is solved until the problem is reduced to the two-wavelength case solved in Eq. 4.38. More graphically, the four-wavelengths instantiation is illustrated in Fig. 4.6. The unambiguous distance with four wavelengths, $d_{u,4}$ is calculated using λ_3 and $d_{u,3}$. $d_{u,3}$ is evaluated using λ_2 and $d_{u,2}$, and finally, $d_{u,2}$ is evaluated using λ_1 and λ_2. For an N-wavelength system, Eq. 4.43 has to be evaluated for a total of N-1 times. The calculations for μ_1 to μ_N in Eq. 4.44 do not add to the real-time running complexity because they can be precalculated based on the choices of wavelengths, and do not have a dependence on the phase measurements.

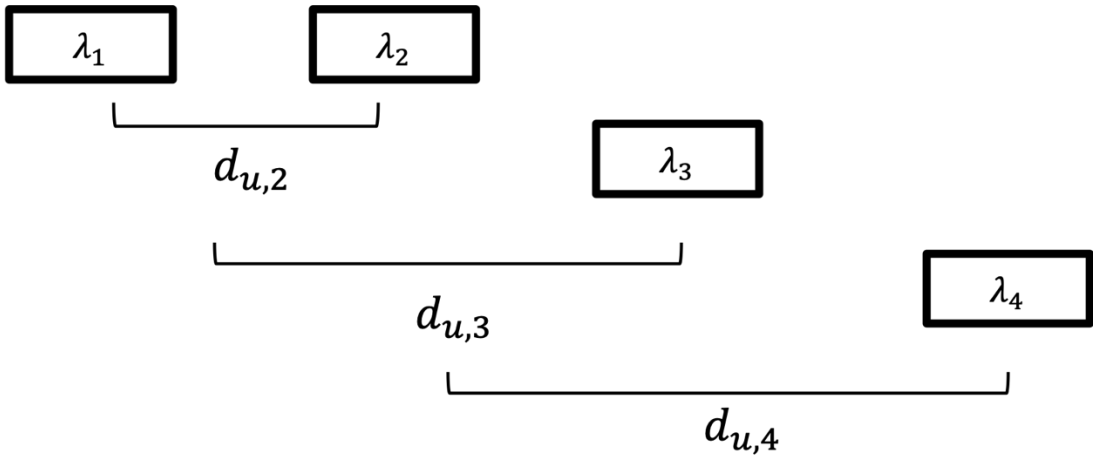

Figure 4.6: An illustration of how a four-wavelength system can be analyzed through our formulation.

Our multiwavelength formulation is also noise-tolerant and reaches the maximum theoretical range. As evident from Eq. 4.43, the range for the N-wavelength case is $\text{lcm}(\lambda_N, \lambda_{e,N-1}) = \text{lcm}(\lambda_1, \lambda_2, \cdots, \lambda_N)$, and is thus equal the maximum theoretical range. Similar to the three-wavelength case, the noise tolerance of the system does not deteriorate if the greatest common divisor or each step is similar. Mathematically, this condition can be expressed as:

$$\text{gcd}(\lambda_N, \lambda_{e,N-1}) \geq \text{gcd}(\lambda_{e,N-1}, \lambda_{e,N-2}) \geq \cdots \geq \text{gcd}(\lambda_1, \lambda_2) > \frac{\sqrt{2}\lambda}{\pi} 3\sigma_\phi \qquad (4.45)$$

The condition in Eq. 4.45 ensures that the nearest integer rounding is executed in an error-free way, and the nearest integer rounding at each step prevents the errors, due to uncertainty in phase measurements, from propagating. The order of λ_1 to λ_N should be chosen to satisfy Eq. 4.45.

The accuracy of the multiwavelength system is the same as a single-wavelength interferometric signal and is the finest when computed when the smallest wavelength λ_s, amongst the N-wavelengths.

To get a better sense of range in a multiwavelength system, we plug some numbers for wavelengths, and compute the range. If the measurement error in phase is such that a system with a gcd of 25 nm can be constructed, the range with two, three and four wavelength system is about 0.1 mm, 6 mm, and 38 cm. If the uncertainty in phase measurements can be decreased such that a gcd of 10 nm can be tolerated, the four-wavelength system, constructed with $\lambda_1 = 1530\ nm$, $\lambda_2 = 1540\ nm$, $\lambda_3 = 1550\ nm$, and $\lambda_4 = 1570\ nm$, has a range up to 5.7 m. The following table gives details of these cases:

gcd (nm)	Wavelengths (nm)	Range
25	1525, 1550	~ 0.1 mm
	1525,1550, 1575	~ 6 mm
	1525,1550, 1575, 1625	~ 38 cm
10	1550, 1560	~ 0.25 mm
	1550,1560, 1570	~ 38 mm
	1530, 1540, 1550, 1570	~ 5.7 m

Table 4.2: Demultiplexed Multiwavelength Interferometry range for different gcd and choices of wavelengths.

Table 4.2 is grouped with different gcd, because the minimum gcd is determined by the noise in phase measurements. Another critical consideration for a multiwavelength system is that the wavelengths cannot always be equally spaced. This is evident in the four-wavelength case listed in Table 3.1. For the gcd = 25 nm case, wavelength 1600 nm is skipped because 1550 nm and 1600 nm have a larger gcd of 50 nm instead, and this results in a smaller lcm and range. Similarly, for the gcd = 10 nm case, wavelength 1560 nm is skipped because 1530 nm and 1560 nm have a larger gcd of 30 nm.

For systems with a large range, such as 5.7 m achieved with four wavelengths in Table 4.2, the uncertainty in phase measurements stems not only from the noise in photodetector current measurements, but also from the laser phase noise. As elaborated in Chapter 3, the integration time has to be increased sufficiently so that the uncertainty is limited by the noise in photodetector currents again. For a 100 KHz linewidth laser, the integration time only needs to be at least 0.1 μs when measuring an interferometric distance of 5.7 m with a 1 GHz sampling frequency. The integration time has to be increased for longer distances.

4.7 Error due to Wavelength Deviation

In section 4.3, we discussed that the wavelengths have to be integers, and the unit is set to calculate in integer field. However, practically, the actual wavelengths might be different from what was intended. This section analyzes the impact of this.

To simplify our analysis, we treat the wavelength deviation as a special case of deviation in the measured phases. We begin with our definition of measured phases expressed in Eq. 4.2 and take the derivative with respect to λ.

$$\delta\phi = \frac{2\pi d}{\lambda^2}\delta\lambda \tag{4.46}$$

Where $\delta\lambda$ is the deviation in the wavelength. While there is a direct relation between $\delta\phi$, the deviation in measured phase, and $\delta\lambda$, $\delta\phi$ also scales with d. Thus, the impact is more severe at

longer distances. From section 4.3, we know that the γ factor is rounded to the nearest integer, and an error in the fringe calculation occurs only when γ deviates by more than 0.5. Plugging Eq. 4.46 into Eq. 4.30, and setting it to the required condition, we get:

$$\sqrt{2}\left(\frac{1}{\gcd(\lambda_1,\lambda_2)}\right)\frac{d}{\lambda}\delta\lambda \ < \frac{1}{2} \tag{4.47}$$

Simplifying Eq. 4.47, and making $\delta\lambda$ the subject:

$$\delta\lambda < \frac{1}{2\sqrt{2}}\gcd(\lambda_1,\lambda_2)\frac{\lambda}{d} \tag{4.48}$$

Our algorithm can still work correctly if $\delta\lambda$ is adequately small such that there is no fringe calculation error within the entire unambiguous range. Thus, the maximum tolerable wavelength deviation for a two-wavelength system can be expressed by plugging in the range, $\mathrm{lcm}(\lambda_1,\lambda_2)$, for distance, d in Eq. 4.48:

$$\delta\lambda_{\max} = \frac{1}{2\sqrt{2}}\gcd(\lambda_1,\lambda_2)\frac{\lambda}{\mathrm{lcm}(\lambda_1,\lambda_2)} = \frac{1}{2\sqrt{2}}\frac{[\gcd(\lambda_1,\lambda_2)]^2}{\lambda} \tag{4.49}$$

For the choices of wavelengths, $\lambda_1 = 1525\,nm$ and $\lambda_2 = 1550\,nm$, used in our experimental setup, a wavelength deviation of up to 0.14 nm can be tolerated. If the starting position is adequately calibrated, such a deviation in wavelength values will not result in an inaccurate fringe calculation within a range. Since Eq. 4.49 scales inversely with the range, the tolerable deviation is smaller for multiwavelength systems.

Chapter 5: Measurement Setup for Demultiplexed Dual-Wavelength Interferometry

In this chapter, we take the concept of demultiplexed multiwavelength interferometry beyond the mathematical formulation discussed in the previous chapter and demonstrate its use in practical dual-wavelength measurement systems, with a large range-accuracy ratio of > 10^5. The two fundamental requirements for our measurement system are: 1) demultiplex the multiwavelength interferograms, and 2) for each wavelength, measure both the sine and cosine phases to resolve the phase ambiguity, as explained in chapter 3. Furthermore, as explained in the previous chapter, to truly extend the range to the lowest-common-multiple of the multiple wavelengths, we need to limit the uncertainty in phase measurements.

In this chapter, we discuss different demultiplexed dual-wavelength interferometry setups, including those that, for reasonable values of wavelength and range, can limit measurement uncertainties in phase and can thus be used to reliably extend the range with our algorithm. We first discuss fiber-based setups, the steps we took to stabilize the system, and the remaining challenges that motivated us to transition to free-space optics. We then discuss the need for simultaneous phase shifting interferometry, and explain our measurement setup, together with a technique to image samples. We then discuss the implications of our measurement methodology on the calculation uncertainties on interferometric phases. And lastly, we propose a way to make the apparatus more compact.

5.1 Fiber Based Setup

Our first demultiplexed multiwavelength interferometry setup was primarily constructed with optical fibers. Such systems are popular because they are quick to assemble since there is no need to align optics. Because of the high-volume communication optical products, the demultiplexing technologies around 1550 nm are mature, inexpensive, and readily available in the market. However, fiber-based systems come with their own set of challenges because the fibers are sensitive to mechanical and thermal variations.

To multiplex and demultiplex the wavelengths, we used a commercial DWDM multiplexer, based on Arrayed Waveguide (AWG) Technology [71], with a small insertion loss of 1 dB. The optical path was then split into reference and sample powers through a 10/90 directional coupler, with the majority of the power going into the sample arm. The reference path connected the first 2x2 10/90 directional coupler to the second combining 3x1 50/50 directional coupler via a phase modulator (PM). The phase modulator was driven with a small square wave, with an amplitude of 50 mV and a frequency of 10 KHz and synchronized to the measuring DAQ. The sample path was sent to a three-port circulator. Light incident from the second port was collimated and incident on a mirror, which was then aligned so that the light was coupled back into the second port of the circulator. To control and alter the path length difference between the sample and reference paths, the mirror was mounted on a piezoelectric motorized stage. For combining the signal from the sample branch to the reference branch, the third port of the collimator was connected to the other port of the 3x1 receiving 50/50 coupler. The output port of the 3x1 50/50 coupler was then connected to the receive port of the DWDM demultiplexer, and the wavelength

demultiplexed ports were connected to fiber-coupled photodetectors, that were then read by the computers through the data acquisition cards that converted the analog voltages to digital signals with high precision. Fig. 5.1(a) shows a schematic of our fiber-based setup. The lines in yellow indicate fiber-based components that include fibers and couplers. Connections shown in black indicate electrical connections.

a)

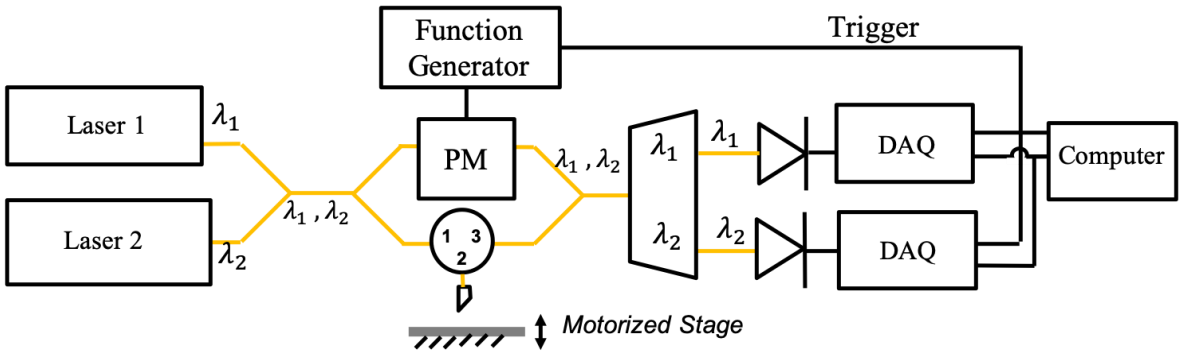

b)

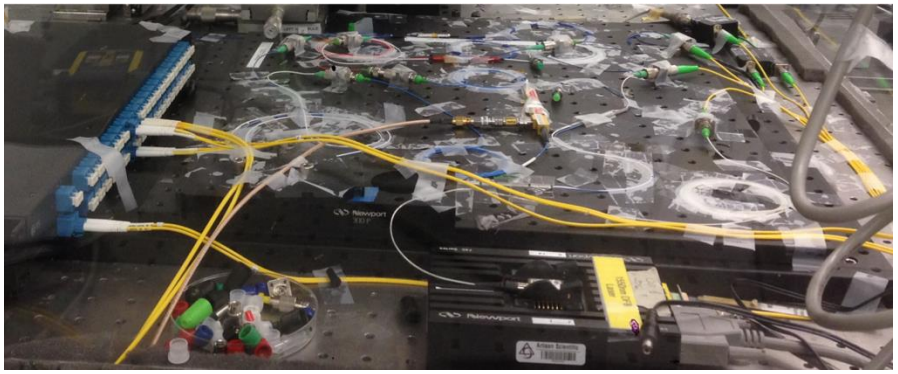

Figure 5.1: a) Schematic of fiber-based interferometry setup. PM is a phase modulator, and DAQ is a data acquisition board. b) A photograph of our fiber-based demultiplexed multiwavelength interferometry setup on a floating optical table. Tapes were used to secure the fibers to the table to stabilize micromovements of the fiber.

The interferometric phase is sensitive to 1) the path length difference between the sample and reference paths, and 2) relative polarizations of the sample and reference powers. The dependence on the path length difference has already discussed in Chapter 3 in great detail. The polarization sensitivity of the interferometric phase is because only electric fields with the same polarization interfere. If one of the two polarization is rotated, it is the projected field, with a smaller amplitude, that interferes. The optical path length of a fiber, and the polarization of light inside it, can vary if the fiber is bent or subjected to temperature gradients, and can thus cause a large variation in the measured phase [72], [73]. To decrease the polarization variability, we used single-mode bow-tie polarization maintaining fibers [74], [75] and polarization maintaining-directional couplers. As pictured in Fig 5.1 (b), we also wrapped extra fiber length into circular

loops, and taped down all the fibers to make it less sensitive to vibrations and atmospheric turbulence.

a) b)

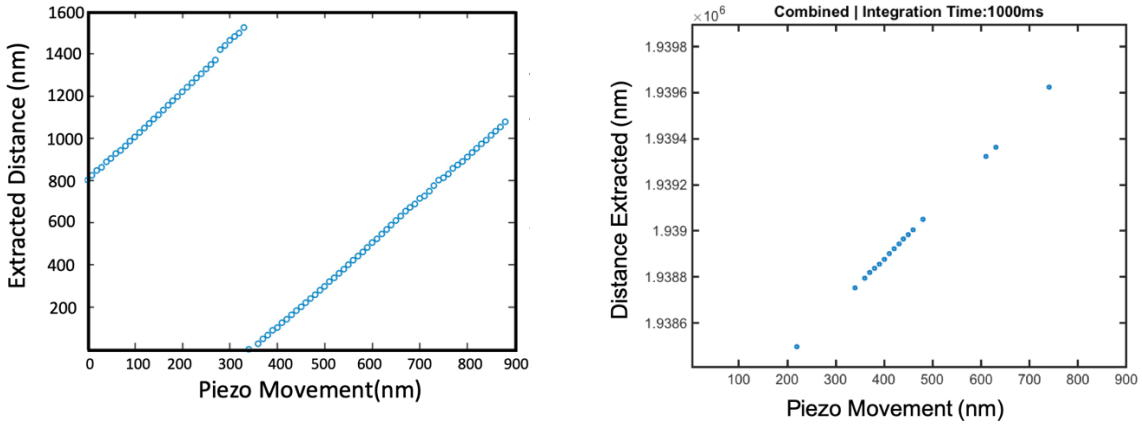

Figure 5.2: a) Phase unwrapped extracted distance from one-wavelength interferometer. The extracted distance wraps around 1λ. b) Extended distance ranging from two wavelength fiber-based multiwavelength interferometry. Some points are not wrapped correctly and expressed in the next figure.

The mirror in Fig 5.1(a) was moved with a motorized stage, and we used the fiber-based setup to measure the movement beyond one wavelength. To unwrap the ambiguity in single wavelength phase measurements, we slightly perturbed the interferometric phase using the phase modulator (PM) and the techniques discussed in Chapter 3. Figure 5.2 (a) shows an example of the distance extracted with a single wavelength: 1550.11 nm. The graph has a slope of two because light is incident onto and reflected from the mirror, and thus the measured distance is twice the distance moved. Figure 5.2 (b) shows the distance extracted through the demultiplexed dual-wavelength interferometry performed with 1550.11 nm and 1550.91 nm. It shows that the extracted distance indeed goes beyond 1λ, but the sparse distribution of points is because of errors in fringe number calculations. This is more evident in Fig 5.3 which shows multiple data points lying on parallel lines separated by λ. It has been added here as an example of running the extended distance algorithm, developed in Chapter 4, on interferometric phases with a large uncertainty.

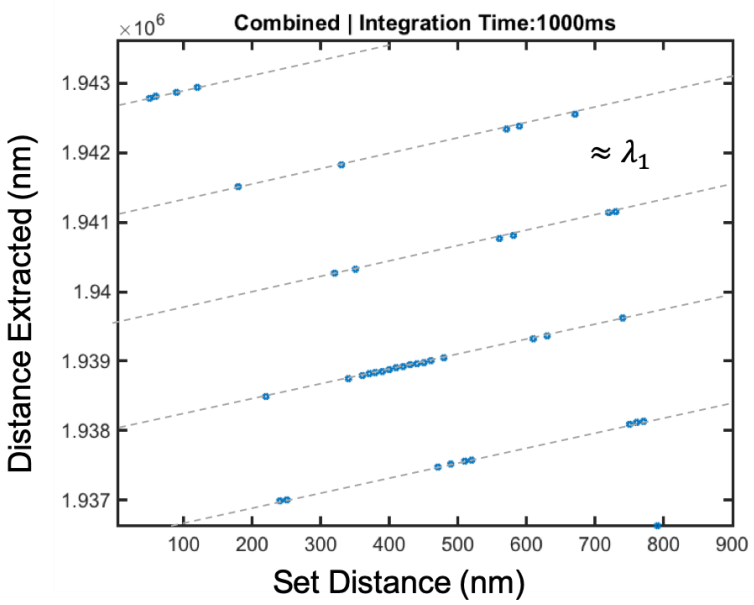

Figure 5.3: Unwrapped distance with fiber-based two-wavelength interferograms. A large uncertainty in phase measurements results in unreliable phase unwrapping.

Despite our best attempts to stabilize the fiber-based setups, the interferometric phases proved to be too noisy to reliably use in a demultiplexed wavelength configuration. This was primarily due to two reasons: 1) our setup was not thermally insulated and temperature gradients at different parts of the fiber setup caused a large uncertainty in phase measurements, and 2) although our wavelengths were multiplexed and demultiplexed simultaneous, the phase-shifting was time-multiplexed and done through the phase modulator driven with a square-wave. Environmental vibrations faster than the phase modulation caused a completely different phase to be detected for the two perturbed phase states, and thus the unwrapped phase from the two had a larger uncertainty. We were thus motivated to transition to a setup with free-space optics, and a method to also simultaneously perform the phase-shifting to unwrap the individual interferometric phases.

5.2 Simultaneous Phase-Shifting Interferometry

In this section, we introduce a simultaneous phase shifting demultiplexed dual-wavelength interferometer, with an extremely low uncertainty in phase measurements. Earlier in this chapter, we discussed two requirements for a measurement setup that is suitable for the demultiplexed multiwavelength technique.

Due to the challenges of a fiber-based time-multiplexed system discussed in Section 5.1, we have to add two more requirements for our measurements setup. To make it insensitive to temperature gradients, it has to be built from free-space optics. Furthermore, to make the setup insensitive to environmental vibrations, it needs to simultaneously multiplex/demultiplex wavelengths, simultaneously induce phase shift phase to get both sine and cosine, and simultaneously detect and measure all the photodetector currents.

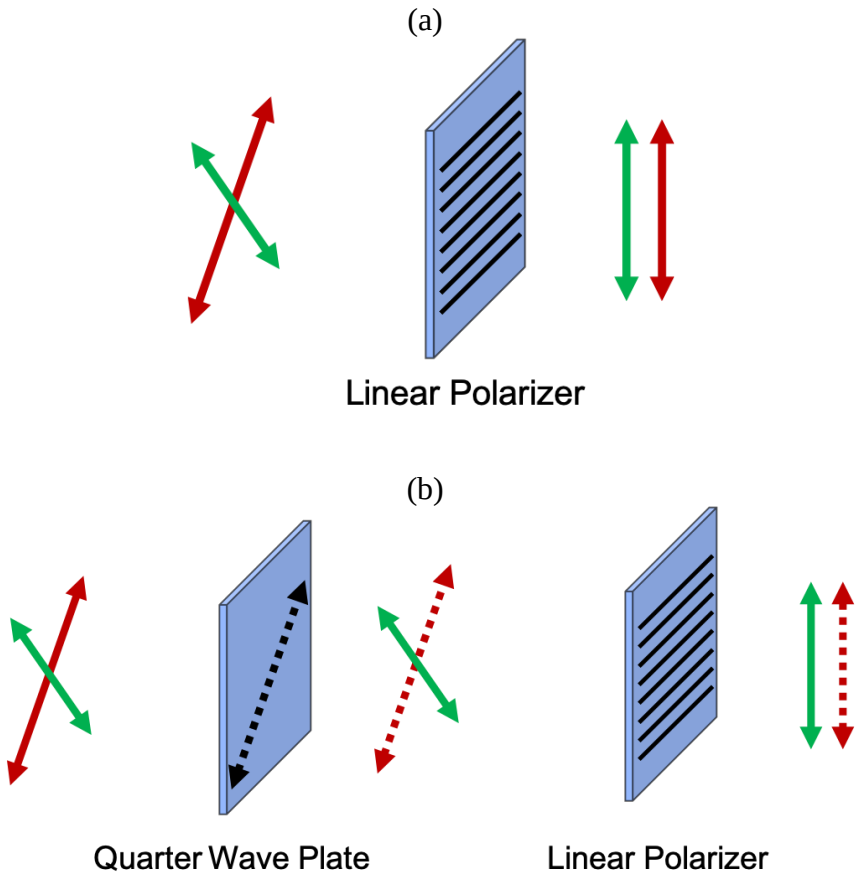

Figure 5.4: An illustration of how polarized optics can be used to induce a $\pi/2$ phase shift. A quarter wave plate with its fast axis oriented along with one of two orthogonally polarized induced a quarter-wave delay to one of the polarizations. In (a), the absence of the QWP results in a cosine of the phase, and in (b), due to QWP, the interferometric power has a contribution for the sine of the phase.

We first discuss a technique to perform phase-shifting with free-space polarization optics. As discussed in Chapter 3, it is critical to measure both the sine and cosine of the interferometric phase. But unlike in fiber-based systems, we cannot use a phase modulator. A need then arises to do this with free space optics. Fig 5.4 shows the two configurations to get the cosine and sine. If the light coming from the sample and reference arms is orthogonally polarized, depicted with green and red polarization axis in Fig 5.4, they do not interfere. However, if they first pass through a linear polarizer, both polarizations get mapped to the same polarization axis, and they thus do interfere. If E_S and E_r is the intensity of orthogonally polarized light coming from the sample and reference power, the interference intensity, I_c, in Fig 5.4 (a) is as follows:

$$I_c = \frac{E_s^2}{2} + \frac{E_r^2}{2} + E_s E_r \cos(\phi) \tag{5.1}$$

Where ϕ is the interferometric phase, and the attenuation of power by a factor of 2 is because of Maulus' law and angle of 45° between the linear polarizer and the polarizations of the reference and sample beams. However, as it is in Fig. 5.4 (b), the interferometric intensity is different if we add a quarter wave plate before the linear polarizer. A quarter wave plate with its fast axis parallel to the polarization axis of either the reference or sample beams, will by the definition of a quarter wave plate, induce an extra $\pi/2$ phase shift between the two arms. The interference intensity for the configuration in 5.4 (b) is therefore:

$$I_s = \frac{E_s^2}{2} + \frac{E_r^2}{2} + E_s E_r \cos\left(\phi + \frac{\pi}{2}\right) = \frac{E_s^2}{2} + \frac{E_r^2}{2} - E_s E_r \sin(\phi) \tag{5.2}$$

The only difference between Eq. 5.1 and Eq. 5.2 is the sine and cosine of the phase. But in addition to the phase shifting, we also have to demultiplex the interferograms for each wavelength. The schematic for the full setup, inspired from the simultaneous phase shifting interferometry setup in [76], is shown in Fig. 5.5.

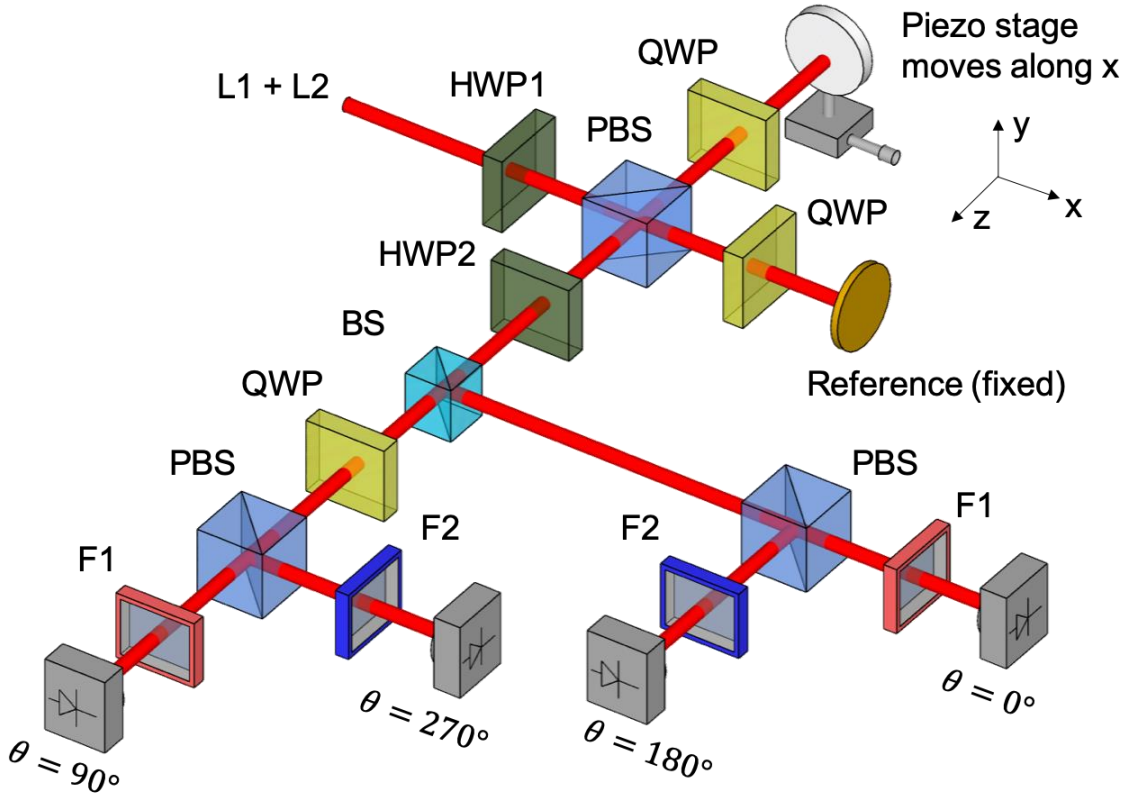

Figure 5.5: Free space based dual-wavelength simultaneous phase shifting interferometry setup.

In our dual-wavelength system, we use two semiconductor lasers that are fiber coupled. To make the two laser beams colinear, we first combine the laser beams with a 2x1 fiber-based 3dB directional coupler, and then connect the output port to a collimator. The laser beams are inherently polarized, so we do not need to add a linear polarizer. A polarizing beam splitter

(PBS) splits light based on polarization. It reflects s-polarized but transmits p-polarized light and is used to split the incident beam to the sample and reference arms. But before the PBS, the beams are passed through a half-wave-plate (HWP). The HWP induces a π phase shift between its orthogonal axis and rotates the polarization of a linearly polarized light by 2α, where α is the angle between the polarization axis of the linearly polarized light and the fast axis of the HWP. The purpose of the HWP1 here is to control the ratio of light that is split between the sample and reference paths. Since the sample path typically loses more power because of the imperfect reflections from the target, it is generally preferred to rotate the HWP such that more power is sent to the sample arm. The beam in the reference arm is reflected from a stationary gold mirror, while the beam in the sample arm is reflected from a sample target.

Optical Element abbreviation	Description
L1 and L2	Fiber coupled lasers for λ_1 and λ_2
HWP	Half wave plate π phase delay on orthogonal axis
QWP	Quarter wave plate $\pi/2$ phase delay on orthogonal axis
PBS	Polarizing Beam Splitters. Light is reflected or transmitted based on its polarization
BS	(non-polarizing) Beam splitter Light is evenly split between the two sides
F1 and F2	Narrow bandpass wavelength filters for λ_1 and λ_2

Table 5.1: Brief descriptions of optical elements used in Fig. 5.5

The inclusion of a quarter wave plate (QWP) in the reference and sample arms is essential for an interferometer. Unless the light in the sample and reference arms is rotated by 90°, it gets sent back to the lasers upon reflection from the mirror and target. But because of the $\pi/2$ phase shift of a quarter wave plate (QWP), if a linearly polarized light is incident on to it, and the QWP is rotated such that its fast axis makes a 45° angle with the polarization of the linearly polarized light, it converts the linearly polarized light to circularly polarized. Upon reflection from the mirror or target, the circularly polarized light encounters the QWP again, and converts back to being linearly polarized but with the orthogonal polarization. Thus, the QWP in the reference and sample arms rotates the linearly polarized light by 90°, so the s-polarized light is converted to p-polarized and vice-versa. Due to the use of the PBS, the light beams from the reference and sample arms are orthogonally polarized at the output port of the PBS. We can now use the ideas discussed in Fig. 5.4 for simultaneous phase shifting interferometry. Because we need to take the sine and cosine of the phase, the reference and sample beams are evenly split with the use of a (non-polarizing) beam splitter (BS).

The simultaneous phase shifting and demultiplexing is done with additional optical elements. Since sample and reference beams are orthogonally polarized, they cannot interfere unless they are projected on to the same polarization axis. For this, we could use a linear polarizer as explained earlier in this section and in Fig. 5.4, but we also need to do it twice for the two

wavelength interferograms. This is achieved through the use of a HWP and a PBS. HWP2, placed between the PBS and BS, rotates the two orthogonally polarized beams by 45°. The PBS in the cosine branch acts like a BS with two orthogonally polarized, horizontal and vertical, linear polarizers on the two sides. The beams transmitted through the PBS acquire a phase shift of 0°, and give an interference intensity with the cosine term, and expressed in Eq. 5.1. The beams reflected through the PBS acquire a shift of 180° and result in a similar expression as Eq. 5.1, but with the opposite sign for the cosine term. Furthermore, since a requirement of our demultiplexed-multiwavelength interferometry system is to demultiplex the wavelengths, we do so by using narrowband wavelength filters. The sine branch is identical to the cosine branch, but with the addition of a QWP to induce the $\pi/2$ phase shift. The QWP is rotated to match the configuration discussed earlier in this section. Instead of the interferometric terms with the cosine and negative cosine, we obtain terms similar to Eq. 5.2, but with the sine and negative sine of the interferometric phase. Similar to the cosine branch, the wavelength interferograms in the sine branch are also demultiplexed with identical narrowband bandpass wavelength filters. Thus for λ_1, we obtain interference terms with cosine and negative sine. For λ_2 we obtain interference terms with negative cosine and sine. The sign of the terms is not critical, and what is important is that for both wavelengths, we separately obtain interferometric intensities with both the sine and the cosine of the phase. Four free-space single-pixel photodetectors were used to measure the interferometric intensities of the four branches, and they were read through a four-channel oscilloscope and processed on a computer.

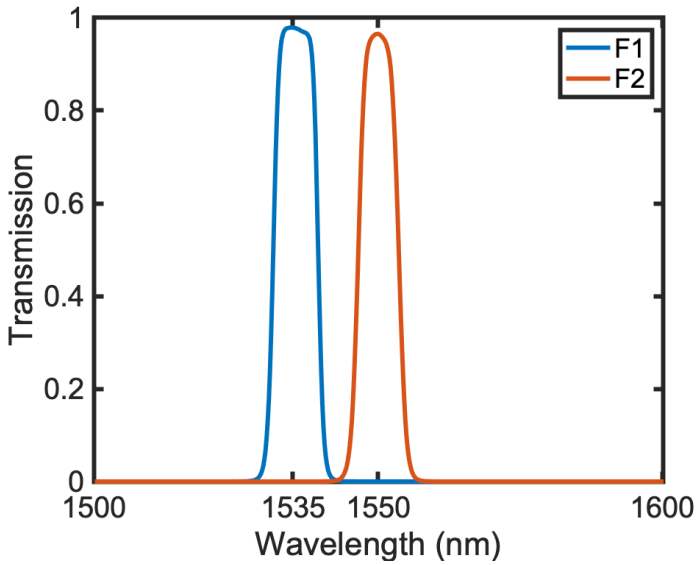

Figure 5.6: Transmission spectrum of the two narrowband wavelength filters, NIR01-1535/3-25 and NIR01-1550/3-25, purchased from Semrock with spectrum centered at 1535 nm and 1550 nm

The two lasers we used were Agilent 81680A, set at 1525 nm, and Thorlabs SFL SFL1550P, set at 1550 nm. Our lasers had a power of 4 mW. The waveplates and optics were purchased from Thorlabs. The bandpass filters were from Semrock NIR01-1535/3-25, with the bandpass centered at 1535 nm, and NIR01-1550/3-25, with a bandpass centered at 1550 nm, and their transmission spectrum is plotted in Fig. 5.6. It is known that the center wavelength of any

spectral filter decreases for an off-normal angle of incidence [77]. Because we wanted to use the 1535 nm filter to filter out the 1525 nm laser, we tilted the filter, and relied on the following relationship:

$$\lambda_c(\theta) = \lambda_{c0}\sqrt{1 - \left(\frac{\sin\theta}{n_{eff}}\right)^2} \tag{5.3}$$

Where λ_C is the center frequency of the rotated filter, λ_{C_0} is the center frequency of the filter at normal incidence, θ is the rotation angle of the filter and is equal to the angle of incidence of light on the filter, and n_{eff} is the effective refractive index of the filters. For our filters from Semrock, n_{eff} is 2.08 and 1.62 for s-polarized and p-polarized light. Using Eq. 5.3, the required rotation to shift the center bandpass wavelength can be expressed as:

$$\theta = \sin^{-1}\left[\sqrt{\left(1 - \frac{\lambda_c^2}{\lambda_{c0}^2}\right)n_{eff}}\right] \tag{5.4}$$

To use our 1535 nm filter to filter 1525 nm light ($\lambda_c = 1525\ nm$, $\lambda_{c0} = 1535$ nm), we had to rotate the filter by 8.34° for p-polarized light. As depicted in Fig. 5.5, since both F1 filters were on the transmission side of the PBS, and thus p-polarized, the rotation angle was the same for the sine and cosine branches.

A caveat for working with free-space systems is that they have to be properly aligned. Alignment is not only important to minimize losses but is also critical to make the beams from the sample and reference arms colinear in tilt and translation. For the beams to interfere, they have to intersect on the photodetector. But if the beams from the sample and reference arms are at an angle to one another, they will form multiple fringes on the detector. In our simplified analysis in Chapter 3, we assumed that k_x and k_y are zero and therefore $k = k_z$. The path length difference was in the z-direction, and thus the phase could be written as $\phi = k_z d = kd$. However, that's most often not the case, and we have small, but non-negligible k_{xy} components, and they cause multiple fringes to form when the beams interfere. Because the setup is physically large, it has to be the case that $k_{xy} \ll k_z$ for the sample and reference beams to intersect. We thus also make the reasonable assumption that k_{xy} and k_z is the same for both the sample and reference beams. For each wavelength in the multiwavelength interferometer, if the k_{xy} of the sample beam makes an angle of θ_1 with the x-plane, and similarly if the k_{xy} of the reference beam makes an angle of θ_2 with the x-plane, the electric field at the photodetector is:

$$E = E_s e^{[j(k_{xy}\cos\theta_1 x + k_{xy}\sin\theta_1 y + k_z d_1)]} + E_r e^{[j(k_{xy}\cos\theta_2 x + k_{xy}\sin\theta_2 y + k_z d_2)]} \tag{5.5}$$

The interference intensity is simply the magnitude of the complex electric field in Eq. 5.5, and is therefore:

$$I = I_R + I_S + 2\sqrt{I_R I_S}\cos\left[k_{xy}x(\cos\theta_1 - \cos\theta_2) + k_{xy}y(\sin\theta_1 - \sin\theta_2) + k_z(d_1 - d_2)\right] \tag{5.6}$$

Where I_s and I_r are E_s^2 and E_r^2 respectively. x and y are the coordinates of the photodetector active area, and $k_z = \sqrt{k^2 - k_{xy}^2}$. For the phase shifted path in Fig. 5.5, we get the sine, instead of the cosine term, in Eq. 5.6. If $\theta_1 \neq \theta_2$, multiple fringes form on the active area of the photodetector array, and they are all averaged over. Fig 5.7 shows a simulation of how the fringes appear on a photodetector active area of 2.25 mm^2 for a fixed $k_{xy} = 0.1\,k$ and interferometric phase $\phi = k_z(d_1 - d_2) = \pi/4$, but different $\Delta\theta = \theta_1 - \theta_2$. If $\Delta\theta = 0$, we get a single fringe all across, as shown in Fig. 5.6 (a), but the number of fringes increase with increasing $\Delta\theta$, as shown in Fig. 5.6 (b) and 5.6 (c).

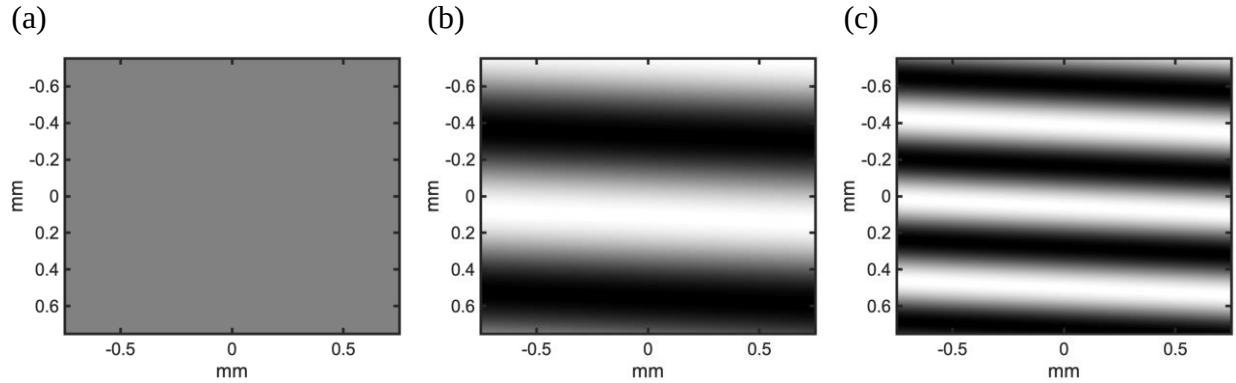

Figure 5.6: Simulations of how interferometric fringes for $\phi = \pi/4$ appear if the difference of the angles of the reference and sample beams is a) 0°, b) 1° and c) 2°. In these simulations, we assume that $k_{xy} = 0.1\,k$, and $\theta_1 = 2°$

In our system, it is critical to ensure that only a single interferometric fringe is formed on all four photodetectors. Since we're only interested in detecting the $k_z(d_1 - d_2)$ term, a non-zero $\Delta\theta$ causes multiple fringes on the active area of a single-pixel photodetector, and the photodetector thus averages over all the fringes. We could get around this problem but inserting small apertures in front of all four photodetectors, such that only one fringe passes through. However, for the multiwavelength interferometry system to work, we need to measure the same interferometric phase at all four photodetectors. We would thus need to make sure that the aperture sections the same fringe position for all four photodetectors, a requirement that is impractical. It is thus imperative to minimize $\Delta\theta$ at all four photodetectors. We do so by carefully aligning the reference and sample mirrors/targets and confirm a single fringe by imaging the fringe at all four photodetector positions. Fig. 5.7 shows a typical example of a single fringe achieved through careful alignment of the reference and sample mirrors. It is circular in shape because our beams are gaussian with an illumination waist of 1.7 mm. Different subfigures show how the fringe appears with different interferometric phases, altered by moving the sample mirror with a motorized stage. To enhance the fringe contrast, we also need to equalize the sample and reference arm powers and do so by rotating the HWP1 in Fig. 5.5.

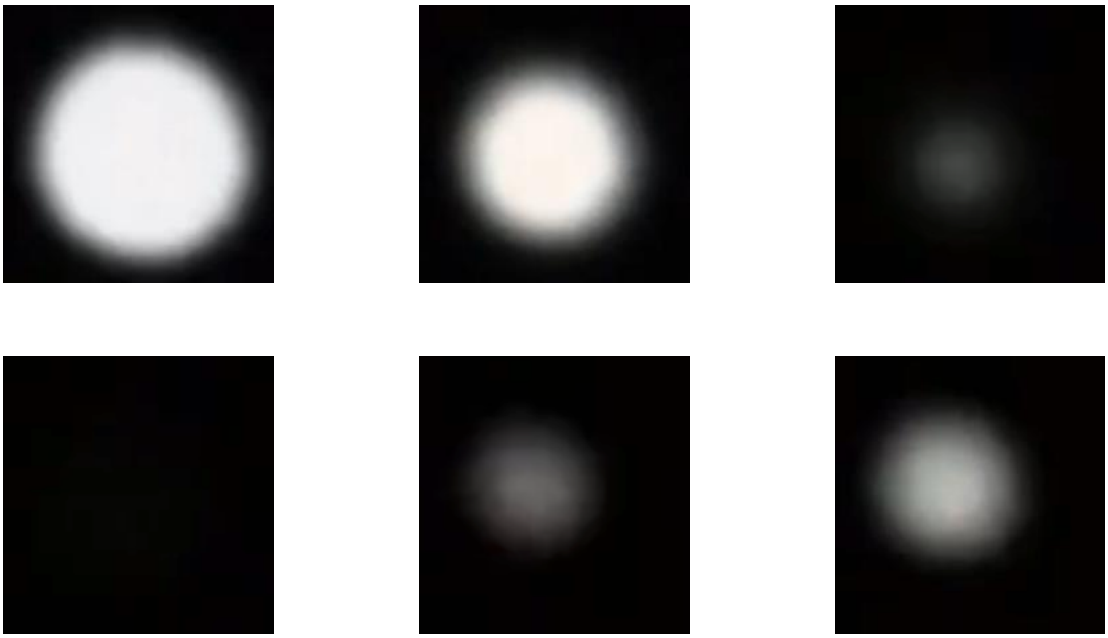

Figure 5.7: A typical result of a single interferometer fringe through the careful alignment of sample and reference reflectors. The six plots show the fringe appears as the interferometric phase is changed. We also see perfect deconstructive interference, indicating that the powers were also well matched.

Another consequence of working with free-space optics is that we have to engineer around the non-idealities of the optical components. One such component that is critical in our setup is the quarter wave plate that is used to induce the extra $\pi/2$ phase shift. A deviation in this $\pi/2$ phase shift will not lead to the sine phase term in Eq. 5.2 and will prevent us from using the arc tangent function. The exact phase shift has to therefore be measured and corrected. To do so, we use the concepts of phase perturbation, discussed in Chapter 3, to measure the phase shifts. Fig. 5.8 shows an example of the phase shifts that were measured. There are two important deductions from the figure. First, the phase shifts were different for the two wavelengths and this is due to the chromatic dispersion of the quarter wave plate. Even though we had used a broadband quarter wave plate, it is evident that it still corresponds differently to 1525 nm, and 1550 nm. Second, we see that both phase shifts deviated from the intended phase shift of 0.5 π. The measured phase shift looks noisy, and seems to blow up at times, and this is because the arc-cosine function blows up around 1 and -1. We therefore use the average of the measured phase shifts, and use that to calculate the sine of the phase:

$$\sin\phi = \frac{\cos\theta\cos\phi - \cos(\theta+\phi)}{\sin\theta} \tag{5.7}$$

Where θ is experimentally measured phase shift induced by the quarter wave plate and is used to calculate $\cos\theta$ and $\sin\theta$. $\cos\phi$ is directly extracted from the interferometric intensity through the cosine branch and expressed in Eq. 5.1, and $\cos(\theta+\phi)$ is extracted from the interferometric

intensity through the 'sine' branch. Details on how the interferometric intensity is normalized to extract the cosine terms is explained in Section 5.5. The $\sin\phi$, calculated using Eq. 5.7, can thus be used together with $\cos\phi$ and quadratic arctangent function to extract the phase.

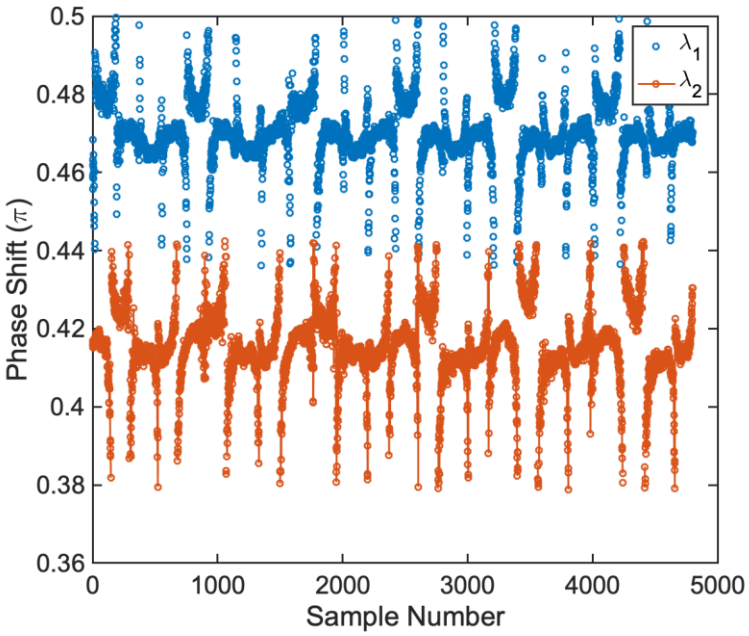

Figure 5.8: Measurements of the actual phase shifts induced by the quarter wave plate. These deviate from the intended phase shift of 0.5 π, and are used to calculate the sine of the phase.

5.3 Measuring Mirror Movements

To verify that our measurement system can indeed measure with a high precision and extended range, we first measured the distance to a gold mirror mounted on a motorized stage. The wavelengths we used were 1525 nm and 1550 nm, and we expected a range of 94.55 μm. The mirror was moved with a stepper motor (Thorlabs Z825B). At each position of the mirror, we measured the interferometric currents at the four branches of Fig. 5.5, and then normalized the signals with the reference and sample powers using the method in Section 5.5 to extract the cosine and sine of the phase for each wavelength. Thus, using the photodetector currents, we calculated $\sin\phi_1$, $\cos\phi_1$, $\sin\phi_2$ and $\cos\phi_2$. Using these four signals, and the quadrature arctangent function, we calculated ϕ_1 and ϕ_2. We then used our analytical formulation, discussed in chapter 4, to calculate the fringe number and the extended distance.

To first verify our analytical formulation, we moved the mirror in the z-direction, and compared the distance moved to the distance measured by the system. We can draw a few important conclusions from the results of this experiment, plotted in Fig. 5.9. Firstly, the slope of two is expected and occurs because of the double pass of the beam: the light beam travels twice the distance of the mirror movement because it gets reflected from the mirror. This result also shows that our system has a range beyond 1λ. Each position was measured independently of others, and unlike the fiber-based system, our free-space simultaneous phase shifting setup measures and

extends the distance reliably and thus without the fringe estimation errors in Fig. 5.3. The non-linearity of the line is due to imperfect motion of the stepper motor.

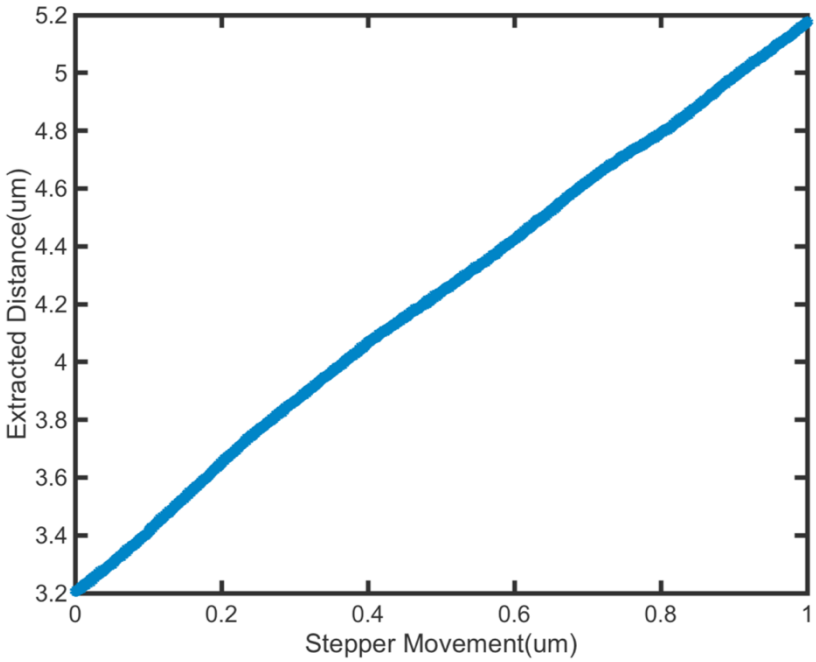

Figure 5.9: Distance to a mirror, moved through a stepper motor, was measured through our setup. The slope of two is due to the double path length because of a reflective setup.

To further validate our range and accuracy, we mounted the mirror on a piezoelectric stage (Newport NanoPZ), and to increase the sensitivity of measurement in the z-direction, we slightly tilted the mirror by 0.6° and moved it in the x-direction, as shown in Fig. 5.3. The tilt of the reference mirror was adjusted accordingly, and we used the technique, discussed in Section 5.2, to ensure single fringe formation on the photodetectors. Results of this experiment are shown in Fig. 5.10. As in the previous experiment, each position of the mirror was measured independently, and the fact that the fringe numbers of a total of 90,252 positions were all reliably calculated and the distances reliably extended, is a testament to the reliability of our experimental setup and mathematical formulation. The distance to the mirror was measured to a range of 94.55 μm, which is exactly the lowest common multiple of the wavelengths used in our interferometry: 1525 nm and 1550 nm. Furthermore, as an example of the precision of a typical measurement through our setup, Fig. 5.10 (b) shows a zoomed in plot of the area marked by the black rectangle in Fig. 5.10 (a). The abrupt fluctuations in distances are because of the typical jitter of piezoelectric stages, triggered by their closed loop position stabilization. Typically, since these movements are so small, they can't be measured by conventional metrology systems and are disregarded as noise. But our system is sensitive and fast enough to correctly measure these fast movements and can even measure them down to the nanometers.

(a) (b)

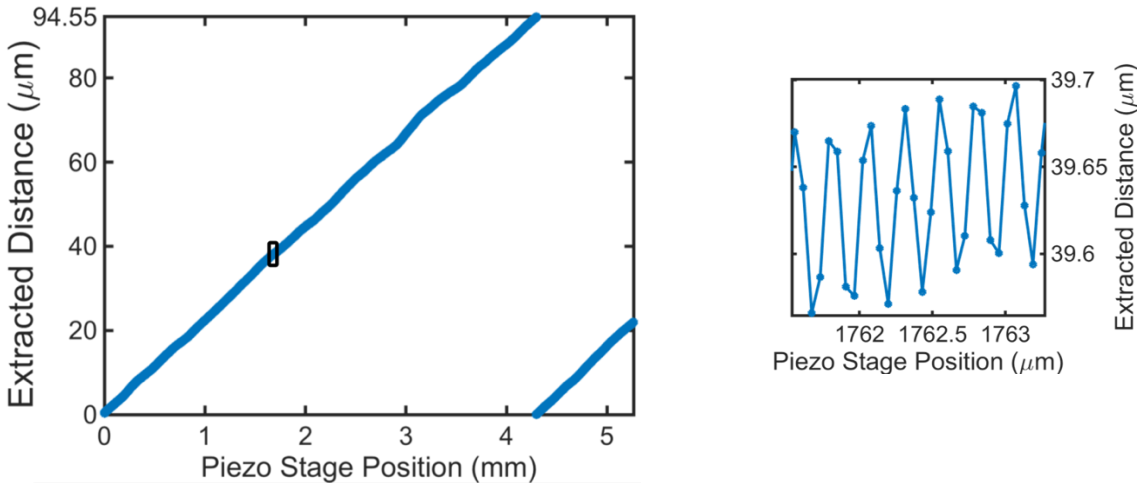

Figure 5.10: A tilted mirror is moved in the x-direction, and distance to the mirror is measured with our setup. The plot in (a) confirms our expected range of 94.55 μm. (b) is zoomed in graph of the section boxed in (a) and shows the nanometer-scale jitter of the piezo stage.

To estimate the accuracy of the system, and to empirically measure the uncertainty in phase measurements, we take a closer look at the fringe number calculation. Fig. 5.11 (a) shows an experimental example of fringe calculations for different distances to the sample mirror, as the sample is moved. Fig. 5.11 (b) shows a histogram of a particular fringe number calculation from Fig 5.11 (a). The standard deviation is measured to be 0.047. Using this number, and Eq. 4.29, the uncertainty in phase measurements, σ_ϕ, is measured to be $2\pi/1917$. This results in a single-sigma depth accuracy of 0.8 nm. To the best of our knowledge, the uncertainty in our phase measurements is the lowest ever achieved in a multiwavelength interferometry setup.

(a) (b)

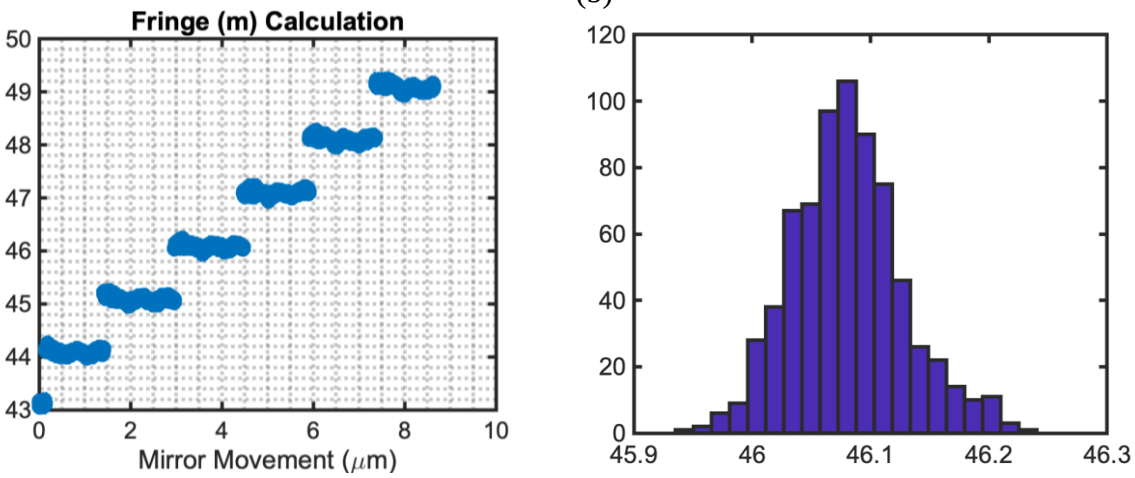

Figure 5.11: a) Experimental calculation of fringe numbers for different distances to the sample mirror. The error-free calculation of fringe order is a testament to the reliability of our system. b) the histogram of one particular fringe calculation. The standard deviation is measured to be 0.047.

5.4 Imaging Samples

In this section, we discuss additions to our measurement setup that make it possible to measure the surface of a sample. In the previous section, we verified that the measurement setup can measure distances with an extended range and high precision. We also verified that the absolute measured distances are reliable as they correctly correspond to the distance moved through the motors. To image samples, we need to add optics that can 1) reduce the beam spot size to measure smaller lateral features, and 2) configure a way to measure different parts of the sample, either through beam steering or by mounting the sample on a motorized stage and moving it.

An additional requirement for imaging with a demultiplexed multiwavelength interferometry setup is that the small uncertainty in phase measurements, achieved through the setup explained in Section 5.3, has to be preserved for reliable extended distance calculation. Since an interferometer inherently measures the differences in the sample and reference arm, selectively introducing elements in either arm worsens the uncertainty in phase measurements. For this reason, a galvo scanning system cannot be used because of the Brownian motion of mirrors. The combined use of an objective lens to narrow the spot size, and motorized stage to move the sample, also worsens σ_ϕ. As shown in Fig. 5.12, the addition of an objective lens in the sample mirrors causes multiple interferometric fringes due to aberrations. Furthermore, the use of the objective lens amplifies the imperfect stepper motor stage trajectory and causes the sample and reference beams to misalign as the sample moves. These reasons prevented us from using the objective and stepper motor combination to image samples in our setup. Instead, we resorted to an imaging setup.

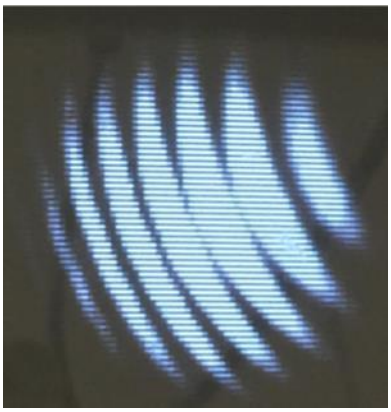

Figure 5.12: Multiple interferometric fringes caused by aberrations when an objective lens is used to reduce the spot size on the sample in the sample arm.

Since the advent of CMOS cameras, imaging systems have considerably evolved. A scene can be imaged on to the sensor of the camera with just a single lens through the imaging equation, but a 4f imaging system is more advantageous and reliable [78], [79]. A $4f$ system involves two lenses, lens 1 and lens 2, spaced apart by the sum of their focal lengths f_1 and f_2. The first lens is placed at a distance of f_1 from the first lens, and the camera sensor is placed at a distance of f_2 away from the second lens. The schematic for a simple 4f system is shown in Fig 5.13. The

lateral resolution of such systems has to do with the pixel size of the camera array, and the diffraction-limited spot size. The magnification of such systems is equal to f_2/f_1.

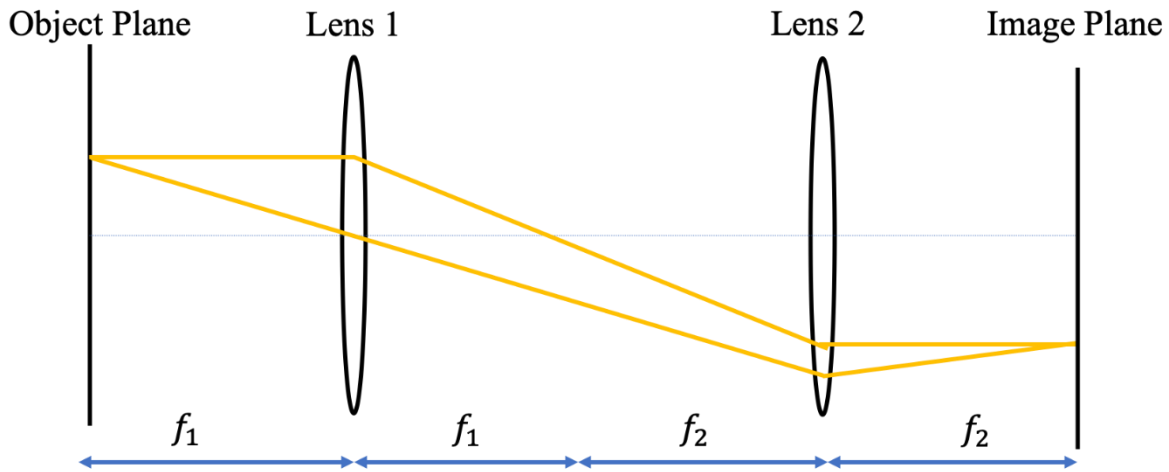

Figure 5.13: Schematic of a simple 4f imaging system

However, since our photodetectors are single pixel, we cannot image the sample on them. Instead, we need a way to parse the image piecewise. To do that we use two $4f$ imaging systems between HWP2 and BS, as shown in Figure 5.14. The first $4f$ system images the sample and reference beams on the aperture plane. The aperture moves in the x-y plane, and the second $4f$ system images the aperture plane on to the four detectors. The focal lengths for the lenses in the first $4f$ system were both 5 cm, while the focal lengths for the lenses in the second $4f$ system were both 10 cm. The selection of larger focal lengths for the second $4f$ system was due to the longer distance between the BS and photodetectors. Since both $4f$ systems were composed of lenses with equal focal lengths, the total magnification was 1. The size of the aperture must be smaller than the smallest lateral features on the sample. In our experiments we used a 200 μm pinhole. A smaller aperture size results in a better lateral resolution, but also causes less power to pass through it and a worse signal-to-noise ratio (SNR). The importance of the SNR is discussed in the next section.

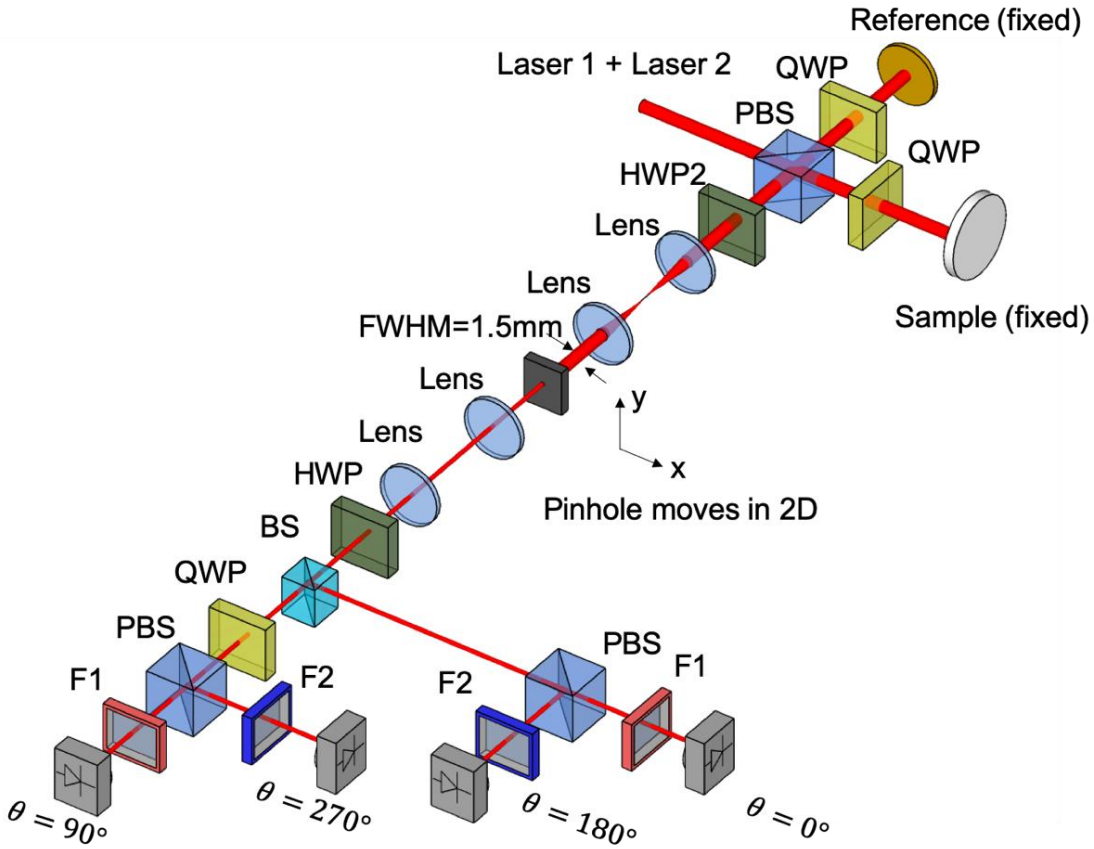

Figure 5.14: The full demultiplexed multiwavelength interferometry imaging setup with the two $4f$ imaging systems, and an aperture to section the image.

We used our setup to measure a gold-coated sample. We moved the aperture around in the x-y plane, and for each aperture position, and we independently used the photodetector currents to calculate ϕ_1 and ϕ_2. We then used the two phases with our algorithm to unwrap the distance. Fig. 5.15 shows the two phases and the distance calculated with our algorithm. Although the original step height was smaller than a wavelength, the fact that our algorithm calculated the distance correctly, without any errors in the fringe calculation, is indicative of the low uncertainty in phase measurements for our imaging setup. Furthermore, to image larger areas, we also moved the sample through a stepper motor, and stitched the images together. We first fixed the position of the sample and moved the aperture in the x-y plane to acquire a scan like the one shown in Fig. 5.15. We then moved the sample by 0.5 mm and took another scan by moving the aperture. Together, we took 13 scans and the stitched scans are shown in Fig. 5.16.

(a)

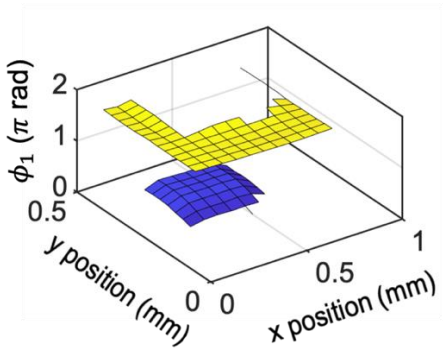

(b)

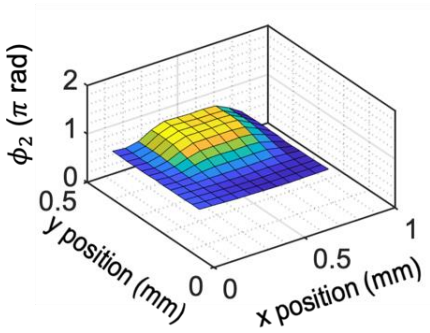

(c)

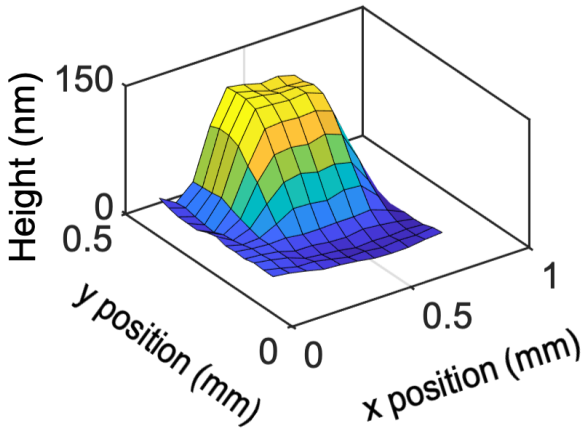

Figure 5.15: Sample measurement through our multiwavelength interferometry setup.

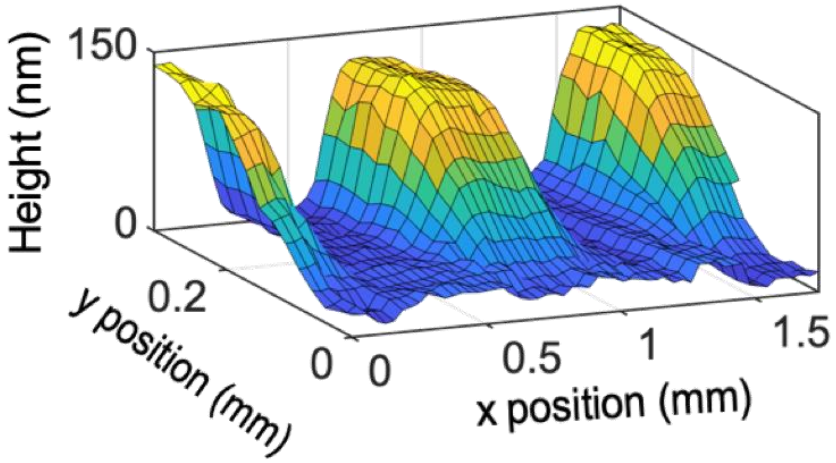

Figure 5.16: 13 scans were stitched together to image a larger section of the sample.

Our interferometry setup is bulky and can be made more compact by using a camera. A camera would eliminate the need for the two 4f systems, but it cannot be used in the current system because since we have four branches that are physically spaced apart, we would need four cameras, and they would have to be synchronized in near-simultaneous time and with extremely low latency. Such a configuration is currently not possible. Instead, in Section 5.6, we discuss a way to use circularly polarized light and linear polarizers to perform phase shifting on the pixels of a camera.

5.5 Uncertainty in phase measurements

The uncertainty in phase measurements has to do with how we extract the unwrapped interferometric phase from the photodetector currents. In this section, we elaborate on our methodology and derive a mathematical model of how the signal-to-noise ratio (SNR) of the detected currents directly impact the uncertainty in phase measurements. Ideally, as explained in Chapter 3, we would like to measure four phase shifts for phase shifting interferometry. However, because we are using two wavelengths, we would have needed a total of eight paths, instead of the four paths discussed in Section 5.3. An elegant way to perform simultaneous phase shifting with four phases and two wavelengths is explained in the next section. But until that setup is realized, we measure just two phase shifts, 0° and 90°, per wavelength demultiplexed interferogram.

For each wavelength, we have to normalize the interferometric signal with the measured reference and sample arm powers. Two phase shifts per wavelength is sufficient to unwrap the phase, but not to extract the cosine or the sine terms from the interferometric current. To do that, we have to separately measure the sample and reference powers and use them to normalize the interferometric current. Unlike the interferometric signal, the reference and sample powers are largely insensitive to environmental vibrations, allowing us to employ a time-stepped scheme to measure them. For either the setup in Fig. 5.5 or Fig 5.14, our measurement is performed in three steps or shots. We first block the reference arm to measure the sample arm power on all four photodetectors. We then block the sample arm to measure the reference arm power on all four detectors. Finally, we unblock both arms to measure the interferometric signal on all four photodetectors, and normalize it using the measured sample and reference powers. The process of blocking and unblocking is performed automatically via a custom-built servo motor-based stage, and the whole measurement, with all the three steps, takes about three seconds, and can be sped up by transitioning to more expensive, shutter-based blockers.

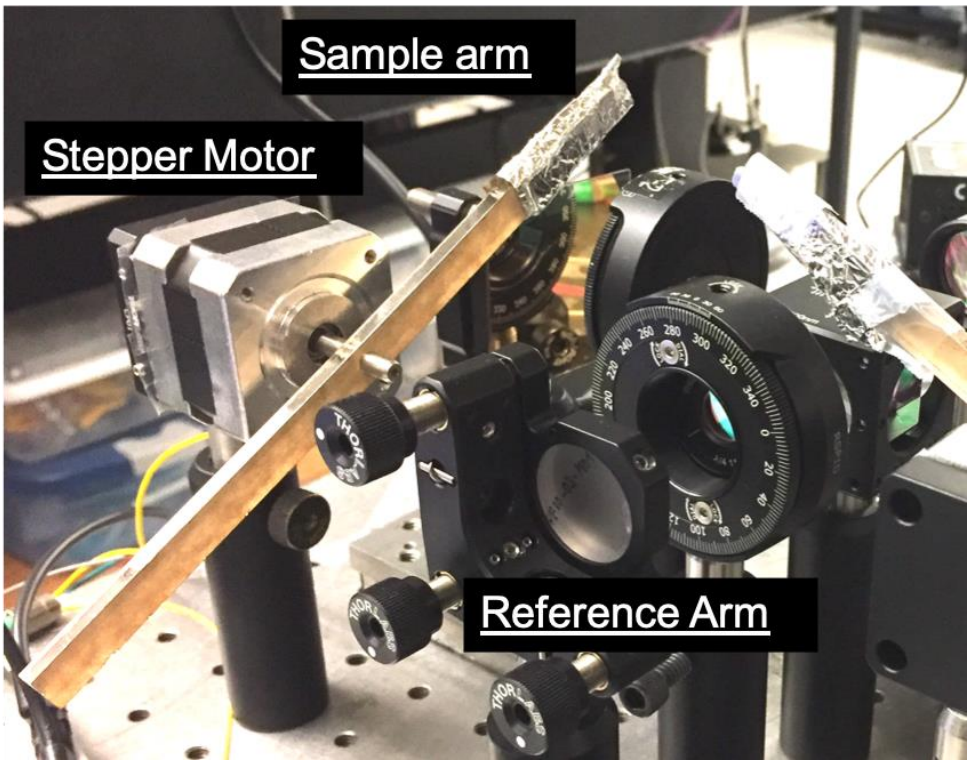

Figure 5.17: A photograph of the two customized beam blockers used to block the sample and reference arm. Two computer-controlled stepper motors rotate an aluminum foil wrapped acrylic barrier. The two motors can be independently controlled so that all blocking/unblocking configurations can be achieved.

Since the procedure for extracting the interferometric phase is the same for the two wavelengths, and because the two wavelengths are independent of one another, we derive the relation between SNR and the uncertainty in phase measurements for just one wavelength and apply it more broadly without any loss of generality.

For each wavelength, over the course of the three time shots, there are a total of six current measurements that are taken. Each current is represented by two subscripts. The first subscript denotes if it is an interferometric signal *I*, reference power *r*, or sample power *s*. The second subscript denotes if it is from the cosine arm *c*, or sine arm *s*. Thus, the interference term with the sine of the phase can be represented as:

$$I_{Is} = I_{ss} + I_{rs} + 2\sqrt{I_{ss}I_{rs}}\sin\phi \tag{5.8}$$

Where I_{ss} and I_{rs} are the reference and sample powers of the sine branch. Similarly, the interference term for the cosine branch can be written as:

$$I_{Ic} = I_{sc} + I_{rc} + 2\sqrt{I_{sc}I_{rc}}\cos\phi \tag{5.9}$$

Where I_{sc} and I_{rc} are the reference and sample powers of the cosine branch. To extract the phase, we first have to extract the sine and cosine terms in Eq. 5.8 and Eq. 5.9 by normalizing it with the respective sample and reference powers. We then have to divide the sine and cosine and take the quadrature arctan to get the phase. Mathematically, this is expressed in the following equation:

$$\phi = \operatorname{atan}\left(\frac{\sin\phi}{\cos\phi}\right) = \operatorname{atan}\left(\frac{\frac{I_{Is} - I_{ss} - I_{rs}}{2\sqrt{I_{ss}I_{rs}}}}{\frac{I_{Ic} - I_{sc} - I_{rc}}{2\sqrt{I_{sc}I_{rc}}}}\right) \tag{5.10}$$

It is pertinent to remember that all six terms inside the arc tangent function are measured quantities. Since they are independently measured, we treat them as independent normal distributions with some uncertainty that is expressed with their standard deviations σ. The uncertainty in current measurements is because of the sources of noise, including thermal noise, RIN noise, shot noise and transimpedance amplifier noise. In our experiments, due to use of the small pinhole of 200 μm for imaging, we had to use a large gain of 50 dB for our transimpedance amplifiers, and the noise was dominated by the large transimpedance amplifier noise of 670 μV. We can use the principles of error propagation to express the uncertainty in phase measurements, represented by its standard deviation, σ_I, in-terms of the measured currents and their standard deviations.

$$\sigma_\phi^2 = \left[\frac{\delta\phi}{\delta I_{IS}}\right]^2 \sigma_{I_{IS}}^2 + \left[\frac{\delta\phi}{\delta I_{ss}}\right]^2 \sigma_{I_{ss}}^2 + \left[\frac{\delta\phi}{\delta I_{rs}}\right]^2 \sigma_{I_{rs}}^2 + \left[\frac{\delta\phi}{\delta I_{Ic}}\right]^2 \sigma_{I_{Ic}}^2 + \left[\frac{\delta\phi}{\delta I_{sc}}\right]^2 \sigma_{I_{sc}}^2 + \left[\frac{\delta\phi}{\delta I_{rc}}\right]^2 \sigma_{I_{rc}}^2 \tag{5.11}$$

Solving the equation above, we get the following:

$$\begin{aligned}\sigma_\phi^2 = \frac{1}{[1+\tan^2\phi]^2}\Bigg\{&\frac{\sec^2\phi}{4I_{ss}I_{rs}}\sigma_{I_{IS}}^2 + \frac{\sec^2\phi\tan^2\phi}{4I_{sc}I_{rc}}\sigma_{I_{Ic}}^2 + \left[\frac{2}{2\sqrt{I_{rs}I_{ss}}}\sec\phi + \frac{1}{2I_{rs}}\tan\phi\right]^2 \sigma_{I_{rs}}^2 \\ &+ \left[\frac{1}{2\sqrt{I_{ss}I_{rs}}}\sec\phi - \frac{1}{2I_{ss}}\tan\phi\right]^2 \sigma_{I_{ss}}^2 + \left[\frac{1}{2I_{rc}}\tan\phi + \frac{1}{2\sqrt{I_{sc}I_{rc}}}\sec\phi\tan\phi\right]^2 \sigma_{I_{rc}}^2 \\ &+ \left[\frac{1}{2I_{sc}}\tan\phi + \frac{1}{2\sqrt{I_{sc}I_{rc}}}\sec\phi\tan\phi\right]^2 \sigma_{I_{sc}}^2\Bigg\}\end{aligned} \tag{5.12}$$

Because all six currents are measured using photodetectors of the same model from the same manufacturer, and since they have the same transimpedance gain, the standard deviation for all six currents can be taken to be similar:

$$\sigma_I = \sigma_{I_{Is}} = \sigma_{I_{ss}} = \sigma_{I_{rs}} = \sigma_{I_{Ic}} = \sigma_{I_{sc}} = \sigma_{I_{rc}} \tag{5.13}$$

Simplifying Eq 5.5 with Eq. 5.6, we get:

$$\sigma_\phi = \sigma_I \sqrt{\frac{\cos^2\phi}{4\, I_{ss}^2 I_{sc}^2 I_{rs}^2 I_{rc}^2} \left\{ \begin{array}{c} \sin^2\phi \left[I_{sc}^2 I_{rs}^2 y_2^2 + I_{ss}^2 \left(I_{rs}^2 I_{rc}^2 + I_{sc}^2 (I_{rs}^2 + I_{rc}^2) \right) \right] \\ + 2\sin\phi \ \left[I_{sc}^2 \ \sqrt{I_{ss} I_{rs}}\, (I_{ss} + I_{rs}) I_{rc}^2 + I_{ss}^2 I_{rs}^2 \sqrt{I_{sc} I_{rc}} (I_{sc} + I_{rc}) \tan\phi \right] \\ +3\, I_{ss} I_{sc} I_{rs} I_{rc} [I_{sc} y_2 + I_{ss} I_{rs} \tan^2\phi \ ] \end{array} \right\}} \quad (5.14)$$

Since the reference and sample arm powers can be equalized using the first half-wave-plate (HWP) in Fig. 5.14, we can set $I_{ss} = I_{rs} = I_s$ and $I_{sc} = I_{rc} = I_c$. Using these simplifications, we can now write Eq. 5.7 as:

$$\sigma_\phi = \sigma_I \sqrt{\frac{3}{4 I_s I_c} + \frac{\left({I_s}^2 + {I_c}^2 \right)}{2 {I_s}^2 {I_c}^2} \sin^2\phi \cos^2\phi + \frac{(I_s + I_c)}{2 I_s I_c \sqrt{I_s I_c}} (\sin\phi \cos^2\phi + \cos\phi - \cos^3\phi)} \quad (5.15)$$

Since power between the two sine and cosine branches is, in principle, equally split, we can make one final simplification of setting $I = I_S = I_c$. Doing so, we simplify Eq. 5.15 to:

$$\sigma_\phi = \frac{\sigma_I}{I} \sqrt{\left(\frac{3}{4} + \sin^2\phi \cos^2\phi + \sin\phi \cos^2\phi + cos\phi \sin^2\phi \right)} \quad (5.16)$$

An important deduction from Eq. 5.16 is that even for a fixed σ_I / I, the uncertainty in phase also depends on the value of the measured phase, which varies from 0 to 2π. To confirm our analytical formulation, we compared it with a Monte-Carlo simulation with ten million random points. Figure 5.18 shows, our model conforms very well to the full Monte-Carlo simulations.

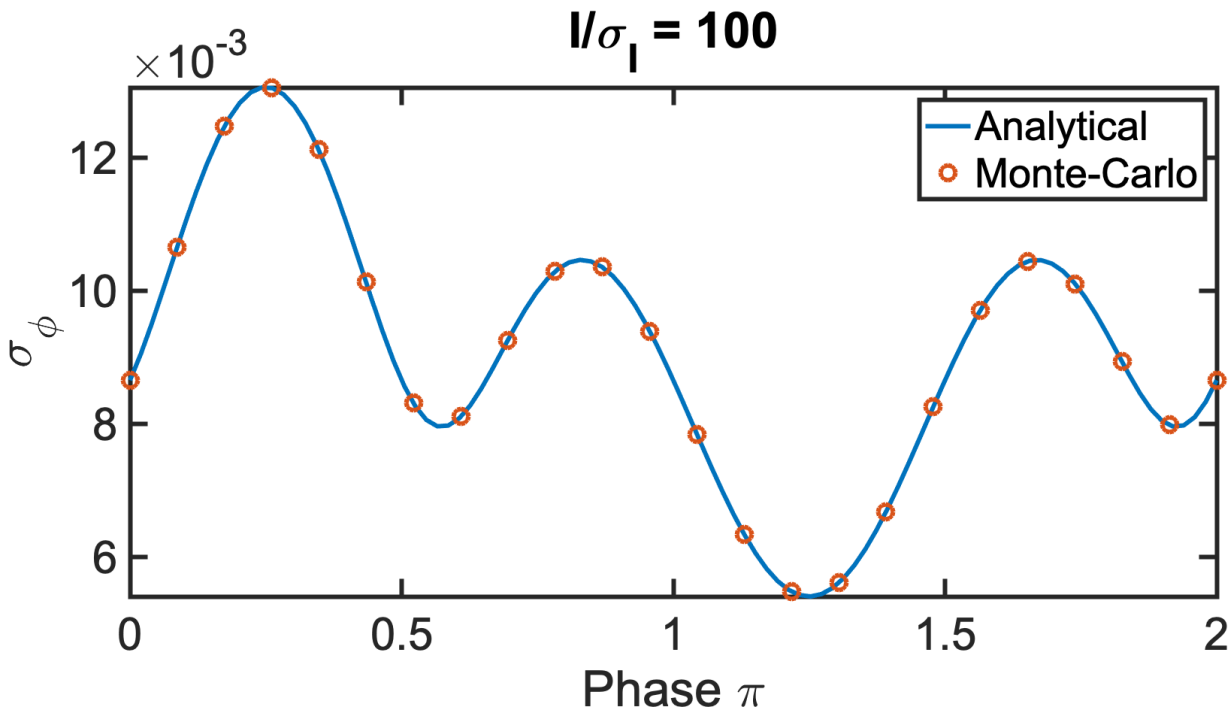

Figure 5.18: Comparison of the simplified analytical model, expressed in Eq. 5.9, and full Monte-Carlo simulations for a fixed I/σ_I of 100. The uncertainty in phase measurements is worse at $\pi/4$

As evident from the plot, the uncertainty is worse at $\phi = \pi/4$, and thus for our analysis, we take this worst-case-situation and plug $\phi = \pi/4$ in Eq. 5.16 to get:

$$\sigma_\phi = \frac{\sigma_I}{I}\sqrt{\left(1+\frac{1}{\sqrt{2}}\right)} \tag{5.17}$$

Defining σ_I/I as the Signal-to-Noise ratio (SNR) of the detected currents, allows us to express the uncertainty in phase as a function of the SNR:

$$\sigma_\phi = \frac{1}{\mathrm{SNR}}\sqrt{\left(1+\frac{1}{\sqrt{2}}\right)} \tag{5.18}$$

Conforming to our intuition, Eq 5.18 reveals that the σ_ϕ is inversely proportional to the SNR with a small proportionality factor of $\sqrt{\left(1+\frac{1}{\sqrt{2}}\right)}$.

We are now in a position to derive a direct expression for the SNR requirements of our demuliplexed multiwavelength interferometry system. Previously, in Chapter 4, we discussed the

relation between uncertainty in phase measurements and the extended distance algorithm. We derived the noise tolerance bounds for a 99.7% reliability, and expressed it as:

$$3\sigma_\phi < \frac{\pi \gcd(\lambda_1, \lambda_2)}{\sqrt{\lambda_1^2 + \lambda_2^2}} \tag{5.19}$$

Plugging the expression for σ_ϕ in Eq. 5.11 into Eq. 5.19, we write:

$$\frac{1}{\mathrm{SNR}}\sqrt{\left(1 + \frac{1}{\sqrt{2}}\right)} < \frac{\pi \gcd(\lambda_1, \lambda_2)}{3\sqrt{\lambda_1^2 + \lambda_2^2}} \tag{5.20}$$

To find a simplified direct relation between the SNR and the gcd, we make SNR the subject of the formula, and similar to our simplification in chapter 3, assume $\lambda_1 \approx \lambda_2 = \lambda$.

$$\mathrm{SNR} > \frac{3\sqrt{2 + \sqrt{2}}\lambda}{\pi \gcd(\lambda_1, \lambda_2)} \tag{5.21}$$

The SNR of the measured currents will dictate the minimum greatest-common-divisor that can be reliably used in the system. A larger SNR will allow us to choose and use wavelengths with a small gcd, and thus a larger lcm and range. For a measurement system with a gcd of 25 nm, the minimum SNR required is 20.4 dB. An SNR of 2.4 dB implies a phase accuracy of $2\pi/527$. Such a system will have a resolution, the standard deviation of distance estimates, ≈3 nm, and the range will increase with the number of wavelengths. Furthermore, an SNR of 25 dB implies a phase accuracy of $2\pi/1521$. If an SNR of 25 dB is achieved, the ranging accuracy will be ≈ $1\ nm$, and the range, with a gcd = 10 nm and a four-wavelength system with wavelengths 1530 nm, 1540 nm, 1550 nm and 1570 nm, will be ≈ $5.7\ m$.

5.6 Towards a Compact Setup

In this chapter, we discuss a way to use geometric phase to make our demultiplex multiwavelength interferometry setup compact. The use of a single camera can eliminate the need for the two 4f systems and aperture scanning, but we first need to bring the phase shifting and demultiplex branches physically together. Instead of working with linearly polarized light, if we switch to circularly polarized light, we can benefit from the principles of Pancharatnam-Berry Phase, also called Geometric Phase. As illustrated in Fig. 5.19 (a), if we start with two circularly polarized beams with the opposite handedness, they have orthogonal polarizations and cannot interfere. However, if they pass through a linear polarizer, they do interfere, and have an added phase that directly depends on the rotation angle θ of the polarizer [80]. The interference can be expressed as:

$$I = \frac{E_s^2}{2} + \frac{E_r^2}{2} + E_s E_r \cos(\phi + 2\theta) \tag{5.22}$$

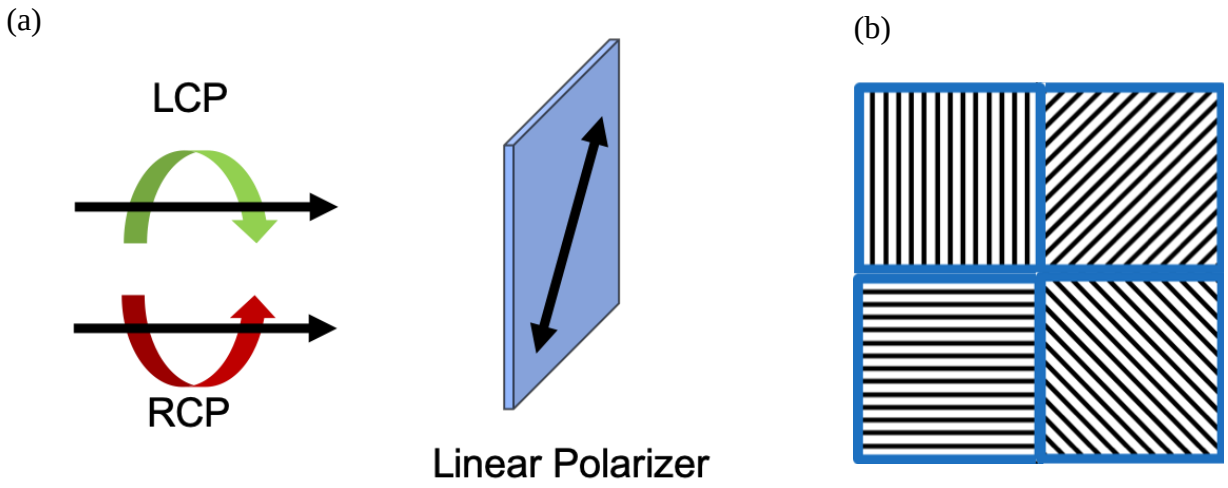

Figure 5.19: (a) An illustration of two circularly polarized beams, with the opposite handedness, incident on a rotated linear polarizer. (b): Schematic of the unit cell with four linear polarizers rotated at 0°, 45°, 90° and 135°to get the four phase shifts.

The polarizer can be rotated by 0°, 45°, 90° and 135° to get four phases shifts equal to 0°, 90°, 180° and 270°. But instead of rotating the polarizer, four different linear polarizers can be used. To make the setup compact, researchers have developed micropolarizer arrays. Each cell of the array consists of 2x2 linear polarizers rotated in the orientation described above. Each polarizer in the 2x2 array is to match the pixel size of the camera, and the array is carefully placed on the camera sensor [48]. A schematic of the phase m ask is shown in Fig. 5.19 (b). However, in order to use this technique, we will need to convert the linear polarized beams, coming from the polarizing beam splitter, to circularly polarized. To do so, we replace HWP2 in Fig. 5.14 with another QWP, and align it such that it makes a 45° angle with both the s and p polarizations. We can then replace the $4f$ imaging systems, and the additional BS, PBS and QWP with just a single camera, as shown in Fig. 5.20.

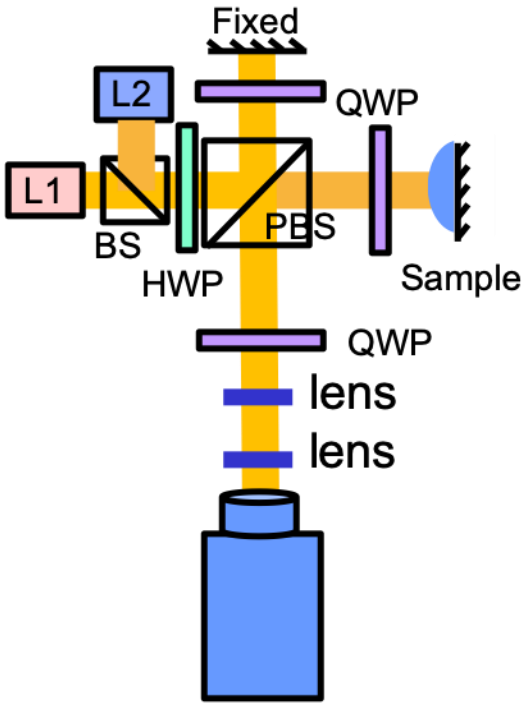

Figure 5.20: A compact imaging setup based on geometric phase.

However, for us to use the setup in Fig. 5.2 with a reliable demultiplexed multiwavelength interferometry configuration, we will have to perform simultaneous phase shifting and demultiplexing. Fig. 5.21 illustrates the steps required to do that. We start with a depiction of the camera pixels, in Fig 5.21 (a). For the simultaneous phase shifting interferometry, the unit cell, illustrated in Fig. 5.19 (b), have to be integrated on top of the camera sensors. Thus, every 2x2 section of the camera pixels is merged into one pixel and can directly measure the phase. To demultiplex the wavelengths, we will have to integrate narrow bandpass wavelength filters on top. The two colors, red and green, represent filters for two wavelengths. Such a system will allow us to perform imaging in a compact demultiplexed multiwavelength interferometry setup. The range will be equal to the lcm of the wavelengths, the depth accuracy will depend on the uncertainty in phase measurements, and the lateral resolution will be limited by eight times the size of the camera pixel.

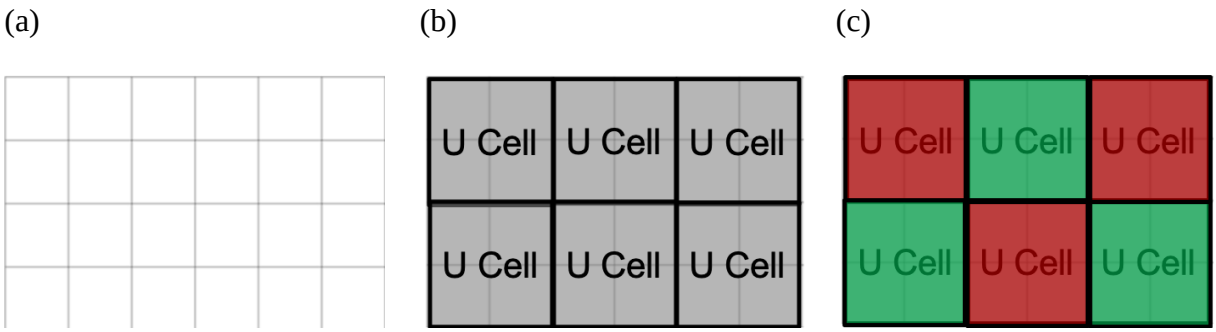

Figure 5.21: Filter and pixelated phase mask requirements for the compact imaging setup.

Chapter 6: Summary

In the first part of this thesis, we show a new technique that utilizes High Contrast Gratings to materialize efficient and colorful solar cells. We show optimized results for thin-film Silicon, InP and Perovskite solar cells, but the technique can be used with any material stack. Our optimization show that it is possible to make the cells colorful with a very small (<5%) penalty on the efficiencies. Furthermore, our experimental results with Perovskite solar cells indicate the viability of our idea. Lastly, we discuss techniques that can be utilized to make the designs polarization and angle insensitive.

In the second part of this thesis, we have demonstrated a new arithmetic algorithm to unwrap the distance from a multiwavelength interferometer. Our analytical formulation has a range of the lcm and can achieve the maximum noise tolerance, as determined by fundamental statistics. Our technique is accurate without any error correction when the deviation of measured phase is within the tolerance bounds. To achieve a low noise in phase measurements, we use a calibrated near simultaneous phase shifting interferometry setup. Furthermore, we describe a technique to measure samples without deteriorating the noise in measured phase. Our setup can be made compact through the use of pixelated cameras with wavelength filters. Our work demonstrates a viable alternative to hierarchical beat-wavelength approaches that necessitate the generation and separation of closely spaced wavelengths to achieve a long range. The simplicity of the algorithm and hardware could enable reliable, instantaneous, low-cost, high-precision and long-range 3D imaging devices. Beyond this, our simple algebraic algorithm offers a way to more conveniently implant the concept of unambiguous range extending in other domains, for example, the multifrequency phase unwrapping in Time of Flight cameras.

Bibliography

[1] M. Grätzel, “Dye-sensitized solar cells,” *J. Photochem. Photobiol. C Photochem. Rev.*, vol. 4, no. 2, pp. 145–153, Oct. 2003.

[2] M. Grätzel, “Conversion of sunlight to electric power by nanocrystalline dye-sensitized solar cells,” *J. Photochem. Photobiol. Chem.*, vol. 164, no. 1, pp. 3–14, Jun. 2004.

[3] H. Otaka *et al.*, “Multi-colored dye-sensitized solar cells,” *J. Photochem. Photobiol. Chem.*, vol. 164, no. 1–3, pp. 67–73, 2004.

[4] J.-H. Yum *et al.*, “Blue-Coloured Highly Efficient Dye-Sensitized Solar Cells by Implementing the Diketopyrrolopyrrole Chromophore,” *Sci. Rep.*, vol. 3, no. 1, p. 2446, Dec. 2013.

[5] R. Komiya, A. Fukui, N. Murofushi, N. Koide, R. Yamanaka, and H. Katayama, “Improvement of the conversion efficiency of a monolithic type dye-sensitized solar cell module,” in *Technical Digest, 21st International Photovoltaic Science and Engineering Conference*, 2011, pp. 2C–5O.

[6] K. Yoshikawa *et al.*, “Silicon heterojunction solar cell with interdigitated back contacts for a photoconversion efficiency over 26%,” *Nat. Energy*, vol. 2, no. 5, p. 17032, May 2017.

[7] B. M. Kayes *et al.*, “27.6% Conversion efficiency, a new record for single-junction solar cells under 1 sun illumination,” in *2011 37th IEEE Photovoltaic Specialists Conference*, 2011, pp. 000004–000008.

[8] E. H. Jung *et al.*, “Efficient, stable and scalable perovskite solar cells using poly(3-hexylthiophene),” *Nature*, vol. 567, no. 7749, pp. 511–515, Mar. 2019.

[9] Y. Deng, Q. Wang, Y. Yuan, and J. Huang, “Vividly colorful hybrid perovskite solar cells by doctor-blade coating with perovskite photonic nanostructures,” *Mater. Horiz.*, vol. 2, no. 6, pp. 578–583, 2015.

[10] J. H. Noh, S. H. Im, J. H. Heo, T. N. Mandal, and S. I. Seok, “Chemical Management for Colorful, Efficient, and Stable Inorganic–Organic Hybrid Nanostructured Solar Cells,” *Nano Lett.*, vol. 13, no. 4, pp. 1764–1769, Apr. 2013.

[11] J. Salvi, J. Pages, and J. Batlle, “Pattern codification strategies in structured light systems,” *Pattern Recognit.*, vol. 37, no. 4, pp. 827–849, 2004.

[12] U. Wijenayake and S.-Y. Park, “An M-array technique for generating random binary pattern based on a connectivity constraint,” in *Workshop on Image Processing and Image Understanding*, 2012.

[13] M. J. Landau, B. Y. Choo, and P. A. Beling, “Simulating Kinect infrared and depth images,” *IEEE Trans. Cybern.*, vol. 46, no. 12, pp. 3018–3031, 2015.

[14] F. Aflatouni, B. Abiri, A. Rekhi, and A. Hajimiri, "Nanophotonic coherent imager," *Opt. Express*, vol. 23, no. 4, pp. 5117–5125, 2015.

[15] G. M. H. and, "Advanced LIGO: the next generation of gravitational wave detectors," *Class. Quantum Gravity*, vol. 27, no. 8, p. 084006, Apr. 2010.

[16] Z. Zhu, G. Xu, K. Ni, Q. Zhou, and G. Wu, "Synthetic-wavelength-based dual-comb interferometry for fast and precise absolute distance measurement," *Opt. Express*, vol. 26, no. 5, pp. 5747–5757, 2018.

[17] V. Durán and P. A. Andrekson, "Electro-optic dual-comb interferometry over 40 nm bandwidth," *Opt. Lett.*, vol. 41, no. 18, pp. 4190–4193, 2016.

[18] C. J. Chang-Hasnain and W. Yang, "High-contrast gratings for integrated optoelectronics," *Adv. Opt. Photonics*, vol. 4, no. 3, pp. 379–440, Sep. 2012.

[19] P. Qiao, W. Yang, and C. J. Chang-Hasnain, "Recent advances in high-contrast metastructures, metasurfaces, and photonic crystals," *Adv. Opt. Photonics*, vol. 10, no. 1, p. 180, Mar. 2018.

[20] J. D. Joannopoulos, S. G. Johnson, J. N. Winn, and R. D. Meade, "Photonic Crystals: Molding the Flow of Light," 1995.

[21] C. Weisbuch, M. Nishioka, A. Ishikawa, and Y. Arakawa, "Observation of the coupled exciton-photon mode splitting in a semiconductor quantum microcavity," *Phys. Rev. Lett.*, vol. 69, no. 23, p. 3314, 1992.

[22] J. P. Reithmaier *et al.*, "Strong coupling in a single quantum dot–semiconductor microcavity system," *Nature*, vol. 432, no. 7014, p. 197, 2004.

[23] Ye Zhou, M. Moewe, J. Kern, M. C. Y. Huang, and C. J. Chang-Hasnain, "A novel high-Q resonator using high contrast subwavelength grating," in *2008 Conference on Lasers and Electro-Optics*, San Jose, CA, USA, 2008, pp. 1–2.

[24] T. Sun, S. Kan, G. Marriott, and C. Chang-Hasnain, "High-contrast grating resonators for label-free detection of disease biomarkers," *Sci. Rep.*, vol. 6, no. 1, p. 27482, Jul. 2016.

[25] M. C. Y. Huang, Y. Zhou, and C. J. Chang-Hasnain, "A surface-emitting laser incorporating a high-index-contrast subwavelength grating," *Nat. Photonics*, vol. 1, no. 2, pp. 119–122, Feb. 2007.

[26] M. C. Y. Huang, Y. Zhou, and C. J. Chang-Hasnain, "A nanoelectromechanical tunable laser," *Nat. Photonics*, vol. 2, no. 3, pp. 180–184, Mar. 2008.

[27] Y. Rao *et al.*, "Long-Wavelength VCSEL Using High-Contrast Grating," *IEEE J. Sel. Top. Quantum Electron.*, vol. 19, no. 4, pp. 1701311–1701311, Jul. 2013.

[28] L. Zhu, W. Yang, and C. Chang-Hasnain, “Very high efficiency optical coupler for silicon nanophotonic waveguide and single mode optical fiber,” *Opt. Express*, vol. 25, no. 15, pp. 18462–18473, Jul. 2017.

[29] A. Wang *et al.*, “Indium-cadmium-oxide films having exceptional electrical conductivity and optical transparency: Clues for optimizing transparent conductors,” *Proc. Natl. Acad. Sci.*, vol. 98, no. 13, pp. 7113–7116, Jun. 2001.

[30] P. Qiao, L. Zhu, W. C. Chew, and C. J. Chang-Hasnain, “Theory and design of two-dimensional high-contrast-grating phased arrays,” *Opt. Express*, vol. 23, no. 19, pp. 24508–24524, 2015.

[31] D. P. Edward and I. Palik, *Handbook of optical constants of solids*. Academic, Orlando, Florida, 1985.

[32] T. Smith and J. Guild, “The CIE colorimetric standards and their use,” *Trans. Opt. Soc.*, vol. 33, no. 3, p. 73, 1931.

[33] L. Zhu, J. Kapraun, J. Ferrara, and C. J. Chang-Hasnain, “Flexible photonic metastructures for tunable coloration,” *Optica*, vol. 2, no. 3, pp. 255–258, 2015.

[34] W. Zhang *et al.*, “Highly Efficient Perovskite Solar Cells with Tunable Structural Color,” *Nano Lett.*, vol. 15, no. 3, pp. 1698–1702, Mar. 2015.

[35] S. A. Kulkarni, T. Baikie, P. P. Boix, N. Yantara, N. Mathews, and S. Mhaisalkar, “Band-gap tuning of lead halide perovskites using a sequential deposition process,” *J. Mater. Chem. A*, vol. 2, no. 24, pp. 9221–9225, 2014.

[36] N. Yantara *et al.*, “Unravelling the effects of Cl addition in single step CH3NH3PbI3 perovskite solar cells,” *Chem. Mater.*, vol. 27, no. 7, pp. 2309–2314, 2015.

[37] K. Fu *et al.*, “Modulating CH 3 NH 3 PbI 3 perovskite crystallization behavior through precursor concentration,” *Nano*, vol. 9, no. 05, p. 1440003, 2014.

[38] C.-W. Chen, S.-Y. Hsiao, C.-Y. Chen, H.-W. Kang, Z.-Y. Huang, and H.-W. Lin, “Optical properties of organometal halide perovskite thin films and general device structure design rules for perovskite single and tandem solar cells,” *J. Mater. Chem. A*, vol. 3, no. 17, pp. 9152–9159, 2015.

[39] V. Karagodsky, C. Chase, and C. J. Chang-Hasnain, “Novel inverse-tone High Contrast Grating reflector,” in *CLEO/QELS: 2010 Laser Science to Photonic Applications*, 2010, pp. 1–2.

[40] C. Chang-Hasnain, L. Zhu, W. Yang, C. Chase, Y. Rao, and M. C.-Y. Huang, “Polarization independent dual usage hcg vcsel-detector with high contrast grating and two dimensional period structure,” 04-Dec-2014.

[41] N. M. Estakhri, V. Neder, M. W. Knight, A. Polman, and A. Alù, "Visible light, wide-angle graded metasurface for back reflection," *Acs Photonics*, vol. 4, no. 2, pp. 228–235, 2017.

[42] X. Yan *et al.*, "Broadband, wide-angle, low-scattering terahertz wave by a flexible 2-bit coding metasurface," *Opt. Express*, vol. 23, no. 22, pp. 29128–29137, 2015.

[43] A. Yariv, "Quantum Electronics John Wiley & Sons," *N. Y. Sec*, vol. 14, 1975.

[44] A. Vasilyev, "The optoelectronic swept-frequency laser and its applications in ranging, three-dimensional imaging, and coherent beam combining of chirped-seed amplifiers," PhD Thesis, California Institute of Technology, 2013.

[45] L. Cohen, "The generalization of the wiener-khinchin theorem," in *Proceedings of the 1998 IEEE International Conference on Acoustics, Speech and Signal Processing, ICASSP'98 (Cat. No. 98CH36181)*, 1998, vol. 3, pp. 1577–1580.

[46] C. Henry, "Theory of the linewidth of semiconductor lasers," *IEEE J. Quantum Electron.*, vol. 18, no. 2, pp. 259–264, 1982.

[47] Y.-Y. Cheng and J. C. Wyant, "Two-wavelength phase shifting interferometry," *Appl. Opt.*, vol. 23, no. 24, pp. 4539–4543, 1984.

[48] J. Millerd, N. Brock, J. Hayes, M. North-Morris, B. Kimbrough, and J. Wyant, "Pixelated phase-mask dynamic interferometers," in *Fringe 2005*, Springer, 2006, pp. 640–647.

[49] N. Brock *et al.*, "Dynamic interferometry," in *Novel Optical Systems Design and Optimization VIII*, 2005, vol. 5875, p. 58750F.

[50] J. C. Wyant, C. L. Koliopoulos, B. Bhushan, and O. E. George, "An Optical Profilometer for Surface Characterization of Magnetic Media," *E Trans.*, vol. 27, no. 2, pp. 101–113, Jan. 1984.

[51] Y.-Y. Cheng and J. C. Wyant, "Phase shifter calibration in phase-shifting interferometry," *Appl. Opt.*, vol. 24, no. 18, pp. 3049–3052, Sep. 1985.

[52] J. C. Wyant, "Testing aspherics using two-wavelength holography," *Appl. Opt.*, vol. 10, no. 9, pp. 2113–2118, 1971.

[53] R. Benoît, "Application des phénomènes d'interférence à des déterminations métrologiques," *J. Phys. Théorique Appliquée*, vol. 7, no. 1, pp. 57–68, 1898.

[54] K. Falaggis, D. P. Towers, and C. E. Towers, "Method of excess fractions with application to absolute distance metrology: analytical solution," *Appl. Opt.*, vol. 52, no. 23, pp. 5758–5765, 2013.

[55] K. Falaggis, D. P. Towers, and C. E. Towers, "Method of excess fractions with application to absolute distance metrology: theoretical analysis," *Appl. Opt.*, vol. 50, no. 28, pp. 5484–5498, 2011.

[56] K. Falaggis, D. P. Towers, and C. E. Towers, "Method of excess fractions with application to absolute distance metrology: wavelength selection and the effects of common error sources," *Appl. Opt.*, vol. 51, no. 27, pp. 6471–6479, 2012.

[57] Y. Ding, J. Xi, Y. Yu, and F. Deng, "Absolute phase recovery of three fringe patterns with selected spatial frequencies," *Opt. Lasers Eng.*, vol. 70, pp. 18–25, 2015.

[58] J. Zhong and Y. Zhang, "Absolute phase-measurement technique based on number theory in multifrequency grating projection profilometry," *Appl. Opt.*, vol. 40, no. 4, pp. 492–500, 2001.

[59] J. Zhong and M. Wang, "Phase unwrapping by lookup table method: application to phase map with singular points," *Opt. Eng.*, vol. 38, 1999.

[60] V. I. Gushov and Y. N. Solodkin, "Automatic processing of fringe patterns in integer interferometers," *Opt. Lasers Eng.*, vol. 14, no. 4–5, pp. 311–324, 1991.

[61] M. Takeda, Q. Gu, M. Kinoshita, H. Takai, and Y. Takahashi, "Frequency-multiplex Fourier-transform profilometry: a single-shot three-dimensional shape measurement of objects with large height discontinuities and/or surface isolations," *Appl. Opt.*, vol. 36, no. 22, pp. 5347–5354, 1997.

[62] W. Wang and X.-G. Xia, "A closed-form robust Chinese remainder theorem and its performance analysis," *IEEE Trans. Signal Process.*, vol. 58, no. 11, pp. 5655–5666, 2010.

[63] X.-G. Xia and G. Wang, "Phase unwrapping and a robust Chinese remainder theorem," *IEEE Signal Process. Lett.*, vol. 14, no. 4, pp. 247–250, 2007.

[64] C. E. Towers, D. P. Towers, and J. D. Jones, "Time efficient Chinese remainder theorem algorithm for full-field fringe phase analysis in multi-wavelength interferometry," *Opt. Express*, vol. 12, no. 6, pp. 1136–1143, 2004.

[65] P. J. De Groot, "Extending the unambiguous range of two-color interferometers," *Appl. Opt.*, vol. 33, no. 25, pp. 5948–5953, 1994.

[66] K. Falaggis, D. P. Towers, and C. E. Towers, "Algebraic solution for phase unwrapping problems in multiwavelength interferometry," *Appl. Opt.*, vol. 53, no. 17, pp. 3737–3747, 2014.

[67] K. Falaggis, A. H. Ramirez-Andrade, D. Towers, C. Towers, and R. Porras-Aguilar, "Multi-wavelength phase unwrapping: a versatile tool for extending the measurement range, breaking the Nyquist limit, and encrypting optical communications," in *Interferometry XIX*, 2018, vol. 10749, p. 1074913.

[68] J. Burke, T. Bothe, W. Osten, and C. F. Hess, "Reverse engineering by fringe projection," in *Interferometry XI: Applications*, 2002, vol. 4778, pp. 312–324.

[69] M. Gupta and S. K. Nayar, “Micro phase shifting,” in *2012 IEEE Conference on Computer Vision and Pattern Recognition*, 2012, pp. 813–820.

[70] Y. Ikeda, S. Yoneyama, M. Fujigaki, and Y. Morimoto, “Absolute phase analysis method for three-dimensional surface profilometry using frequency-modulated grating,” *Opt. Eng.*, vol. 42, no. 5, pp. 1249–1257, 2003.

[71] H. Takahashi, S. Suzuki, K. Kato, and I. Nishi, “Arrayed-waveguide grating for wavelength division multi/demultiplexer with nanometre resolution,” *Electron. Lett.*, vol. 26, no. 2, pp. 87–88, 1990.

[72] G. B. Hocker, “Fiber-optic sensing of pressure and temperature,” *Appl. Opt.*, vol. 18, no. 9, pp. 1445–1448, 1979.

[73] M. Silva-López *et al.*, “Strain and temperature sensitivity of a single-mode polymer optical fiber,” *Opt. Lett.*, vol. 30, no. 23, pp. 3129–3131, 2005.

[74] D. A. Kliner, J. P. Koplow, L. Goldberg, A. L. Carter, and J. A. Digweed, “Polarization-maintaining amplifier employing double-clad bow-tie fiber,” *Opt. Lett.*, vol. 26, no. 4, pp. 184–186, 2001.

[75] F. Zhang and J. W. Lit, “Temperature and strain sensitivity measurements of high-birefringent polarization-maintaining fibers,” *Appl. Opt.*, vol. 32, no. 13, pp. 2213–2218, 1993.

[76] C. L. Koliopoulos, “Simultaneous phase-shift interferometer,” in *Advanced Optical Manufacturing and Testing II*, 1992, vol. 1531, pp. 119–127.

[77] I. Moreno, J. J. Araiza, and M. Avendano-Alejo, “Thin-film spatial filters,” *Opt. Lett.*, vol. 30, no. 8, pp. 914–916, Apr. 2005.

[78] J. Jahns and S. J. Walker, “Imaging with planar optical systems,” *Opt. Commun.*, vol. 76, no. 5, pp. 313–317, May 1990.

[79] S. Sinzinger and J. Jahns, “Integrated micro-optical imaging system with a high interconnection capacity fabricated in planar optics,” *Appl. Opt.*, vol. 36, no. 20, pp. 4729–4735, Jul. 1997.

[80] P. Hariharan and P. E. Ciddor, “An achromatic phase-shifter operating on the geometric phase,” *Opt. Commun.*, vol. 110, no. 1–2, pp. 13–17, 1994.